CFD prediction of hull manoeuvering forces

Chad Oldfield
Roham Larmaei
STX Marine

Prepared By:
STX Marine
Suite 1502, 85 Albert Street
Ottawa, ON K1P 6A4

Contractor's Document Number: 181-050-04, Rev 2
Contract Project Manager: Andrew Kendrick, 613-238-7979
PWGSC Contract Number: W7707-145687/001/HAL
CSA: Kevin McTaggart, Defence Scientist, 902-426-3100 x253

Contract Report
DRDC-RDDC-2014-C236
April 2014

STX Canada Marine

CFD PREDICTION OF HULL MANOEUVERING FORCES

Prepared for:

Department of National Defence
DRDC – Atlantic Research Centre
9 Grove Street
Dartmouth, NS B3A 3C5

Prepared by:

Chad Oldfield
Roham Larmaei

STX Marine
Suite 1502
85 Albert Street
Ottawa, ON K1P 6A4

Project No: 181
Report No: 181-050-04, Rev 2
Date: 2014-04-17

SUMMARY OF REVISIONS

Report No.: 181-050-04, Rev 2

Title: CFD prediction of hull manoeuvering forces.

Rev	Date	Description	Prepared by	Checked by:
0	2014-02-04	Progress report	RML	CO
1	2014-03-21	Draft final report	RML, CO	AK
2	2014-03-17	Addressed client comments	RML, CO	AK

EXECUTIVE SUMMARY

STX Canada Marine have completed CFD simulations to numerically replicate Planar Motion Mechanism (PMM) model tests of the DDG51 frigate, previously completed by FORCE Technology [1, 2] in the context of the SIMMAN workshops. The aim of the present study was to validate both the accuracy and practicality of CFD for the prediction of ship manoeuvring data that can be derived from PMM tests. The scope of the validation is limited to the relatively direct results of the PMM tests or simulations: it does not include the development of manoeuvring derivatives and using them in a mathematical manoeuvring simulation to predict IMO or other ship manoeuvres.

The vessel has a relatively typical fine hullform for a fast displacement naval monohull, and includes both a sonar bulb (below baseline) and bilge keels. No rudder, propellers, shafts, or other appendages were included in either the model tests or the CFD simulations.

Most of the model tests completed at a Froude number of 0.28 were repeated with CFD. The simulations include cases of steady drift, unsteady pure sway, unsteady pure yaw, and the combination of unsteady pure yaw with a superimposed steady drift angle. To establish the spatial discretization error as described for the Journal of Fluids Engineering [3], mesh refinement studies including three mesh sizes were completed for one steady case and one unsteady case. The sensitivity of the results to the bilge keels was investigated by repeating four of the simulations with the bilge keels removed. All simulations have been completed with the intent of carefully replicating the model tests. Details such as the vessel geometry, model scale, physical constants, and equations describing the PMM motion were kept consistent with the model tests [1]. The results analysis focused on the non-dimensional forces and moment of most interest to ship manoeuvring: the longitudinal force, X', the lateral force, Y', and the yaw moment about amidships, N'.

A literature review was completed prior to initiating the simulation work. The relatively few studies found showed a variety of techniques, and some presented relatively good correlation with experimental results for steady simulations. Good validation of unsteady manoeuvring simulations was not found. The review provided some insight into the effectiveness of different CFD modelling techniques and details, in the context of vessel manoeuvring simulations.

While the model test report [1] included a detailed error analysis, some of the final plots showed a drastic difference from the separately presented raw results from the same tests [2]. It was determined that the error was likely in the report [1]; due to this error it could not be assumed that the uncertainty results (shown on the same plots) were correct. This unfortunately limited the consideration for experimental uncertainty to examining the range of results obtained for the few test conditions in which twelve repeat runs were completed.

At higher drift angles, the steady drift solutions exhibited a breaking bow wave on the upstream side, a breaking wave near amidships on the downstream side, and as flow aeration downstream which was drawn under the hull. These flow patterns are unsteady and have too small of a length and timescale to be fully resolved by the simulations. It was also found that the fluctuations in the integrated hull forces and moment were small, and so it was inferred that resolving these flow phenomena accurately is not important to the accuracy of the time-averaged forces and moment. A large vortex shed from the sonar bulb was prominent in the solution. At some drift angles this vortex extended underneath the downstream bilge keel and modified the flow so that the transverse component of the flow velocity across the bilge keel tip was in the opposite direction to the overall drift velocity. This type of flow interaction would not have been captured by classical simple manoeuvring techniques which treat the hull and bilge keel manoeuvring forces separately.

While the above fluctuations in the steady drift results were small, so was the difference between the results achieved with the coarse, medium, and fine meshes. Therefore the calculation of the spatial discretization error was somewhat obscured. The fine-mesh spatial discretization error was determined to be between 0.0004% and 0.14% for X', between 0.26% and 3.0% for Y', and between 0.70% and 1.6% for N'.

For drift angles of 2° or greater, the comparison of the steady drift simulations with model test results showed at most 7.3% error for X', 4.4% error for Y', and 5.4% for N'. With the fine mesh at 10° drift, there were also 12 repeated model tests, and the errors were reduced to 0.9% for X', 2.9% for Y', and 2.6% for N'.

The removal of bilge keels in the 10° drift case resulted in an 11% reduction in X', an 8% reduction in Y', and 1.4% reduction in N'. With bilge keels, the well-established bilge keel vortex merged with the weaker skeg vortex; without bilge keels the skeg vortex remained distinct from other flow features.

The unsteady simulations exhibited similar types of flow phenomena to those found in the steady simulations. In addition, the animations show additional transverse waves having small amplitudes and short wavelengths, which are overtaken by the vessel. These could be either a real physical phenomena or a numerical artifact. Refinement in both time and space would be required to either better resolve either the phenomena or remove the artifact. In either case, it was determined that effects of the small flow pattern on the overall manoeuvring forces and moment are not important.

The post-processing of the unsteady simulations included harmonic analysis of the time-series results to yield the coefficients of a third-order Fourier series for X', Y', and N'. These coefficients are viewed as an intermediary which captures the aspects of the raw time series that would capture the essential manoeuvring characteristics of the vessel, without deriving a mathematical manoeuvring model derived from the CFD results and thereby obtaining final results such as a tactical diameter or zig-zag overshoot. Percentage differences or errors reported for the unsteady results are generally on the basis of Fourier coefficient, normalized by the maximum amplitude of the mean model test time-history so that relatively unimportant Fourier coefficients are not over-emphasized.

Late in the project, when the post-processing of all simulations was effectively complete, it was found that the draft and trim were incorrectly specified in the setup of all unsteady simulations. These have been interpreted as errors in the projected underwater lateral area of 7% to 11%, and errors in the longitudinal centroid of this area of less than 0.53% of the length between perpendiculars. The case used for the mesh refinement study was repeated with corrected drafts and the medium mesh to assess the impact of the erroneous inputs. It was found that the predictions were generally improved by this, although the accuracy (as compared to model tests) was decreased for about a quarter of the results. The difference between the results of the corrected simulation and the mean of the 12 repeat model tests, as determined from the Fourier coefficients, was found to be at most 2.67% for X', 4.54% for Y', and 2.95% for N'.

Despite the above draft and trim error, the unsteady mesh refinement study is still considered to be generally applicable, because the same draft and trim were used on all three meshes. It showed a fine-mesh spatial discretization error of at most 4.80% for X', 0.75% for Y', and 4.75%

for N'. For Y', the mesh convergence appeared to be divergent for some Fourier coefficients; this is expected to be a misinterpretation of oscillatory convergence, and would be clarified by repeating the simulation with a yet finer mesh.

Although the unsteady simulations are subject to draft and trim input errors, the difference from the model test results is at most 33.5%. The most different Fourier coefficient for an individual test is typically between 5% and 20% different from the model test result.

While the simulations with bilge keels removed did not use the intended drafts, the unsteady pure sway case and the unsteady yaw and drift case both used the same drafts with and without bilge keels. The observed bilge keel effect for those is therefore reasonably representative of what would have been observed with the correct drafts. For the unsteady pure sway case, bilge keel removal resulted in a 12% reduction in X', a 21% reduction in Y', and a 12% reduction in N'.

For the unsteady yaw and drift case, bilge keel removal resulted in an 8% reduction in X', a 9.5% change in Y' which visually appeared as a phase change, and a 0.8% change in N'.

Overall, this study has shown validation results which support the accuracy and feasibility of CFD as an early analysis tool for determining the manoeuvring characteristics of a vessel. The accuracy of the steady simulations, as judged by comparisons to model tests, is almost as good as the repeatability of the model tests themselves. This represents a substantial improvement over other studies identified in the literature review, which reported errors in the order of 10% for steady drift cases, and unacceptably large errors for unsteady cases.

As CFD manoeuvring simulation is a new and developing field, there are many opportunities for future work. Recommendations include aspects such as repeating simulations with a corrected draft and trim, better characterizing the model test error, including a rudder and propeller, using CFD to compute the draft and trim, establishing the uncertainty in terms of the salient results of predicted vessel manoeuvres, including roll motions, exploring other ship types, and full-scale validation.

TABLE OF CONTENTS

LIST OF FIGURES

LIST OF TABLES

LIST OF APPENDICES

ACRONYMS AND NOMENCLATURE

AP	Aft Perpendicular
CAD	Computer Aided Design
CFD	Computational Fluid Dynamics
CFL	Courant–Friedrichs–Lewy
DES	Detached Eddy Simulation
DNS	Direct Numerical Simulation
FP	Forward Perpendicular
F.T.	FORCE Technology
HRIC	High Resolution Interface Capturing
LES	Large Eddy Simulation
PMM	Planar Motion Mechanism
SIMPLE	Semi-Implicit Method for Pressure-Linked Equations
SST	Shear Stress Transport
URANS	Unsteady Reynolds Averaged Navier-Stokes
VOF	Volume Of Fluid
6DOF	6 Degree Of Freedom
A_0	lateral underwater area of the ship (approximated by $T_m L_{bp}$)
A_L	lateral underwater area of the ship
B_{wl}	width of waterline
C	denotes a computed data
D	denotes a measured data
F_r	Froude number
g	gravitation acceleration, 9.806 m/s²
H_n	normalized helicity density
I	intensity of turbulence
k	turbulence kinematic energy
k	integer index used in weighted averaging
L	Length scale of turbulence
L_{bp}	length between perpendiculars
L_{wl}	length of waterline
n	number of points used in weighted averaging
N	component of fluid moment acting on the vessel about the z_s direction
N_{PMM}	number of cyclic motion per minute in PMM equipment
p	Pressure
P_0	environmental pressure
Q	second invariant of the rate of deformation tensor, Q-Criterion

r_{PMM}	yaw rate
$\vec{\mathbf{S}}$	rate of strain tensor
$\dot{r}_{PMM}$	yaw acceleration
S_{mm}	a distance related to the measurement equipment
T_m	mean draft
t	Time
t_{std}	steady simulation run time
T	period of oscillatory motions
T_0	environmental temperature
$\vec{u}_g$	velocity vector in global coordinate
u_{PMM}	longitudinal velocity in PMM coordinate
$\dot{u}_{PMM}$	longitudinal acceleration in PMM coordinate
$\vec{u}_{s_g}$	ship velocity vector in global coordinate
$\vec{u}_{s_s}$	ship velocity vector in ship fixed local coordinate
U	Velocity
U_c	carriage speed
v_{PMM}	transvers velocity in PMM coordinate
$\dot{v}_{PMM}$	transvers acceleration in PMM coordinate
w_k	k^{th} weight for the weighted average used in determining steady convergence
X	Component of fluid force acting on the vessel in the x_s direction
$\bar{X}$	Converged value of X, by weighted averaging
x_{AL}	longitudinal component of the centroid of A_L
x_g	global x coordinate
x_m	moving mesh local x coordinate
x_s	ship fixed local x coordinate
Y	component of fluid force acting on the vessel in the y_s direction
y_g	global y coordinate
y_m	moving mesh local y coordinate
y_s	ship fixed local y coordinate
Y_{mm}	a distance related to the measurement equipment
Y_p	the normal distance between the wall and the center of the near-wall cell
y^+	universal dimensionless wall normal distance
z_g	global z coordinate
z_m	moving mesh z local coordinate
z_s	ship fixed local z coordinate
β	drift angle
Δ	vessel mass displacement

ε	turbulence dissipation rate
η_{PMM}	transvers PMM motion in an unsteady test
λ	wave length
θ	The angle between the diverging wave and x_s
ξ_{PMM}	longitudinal translation in PMM coordinate
ρ_w	density of water
τ	time for unsteady run
ω	specific rate of turbulence dissipation
$\vec{\omega}_g$	vorticity vector in global coordinate
ω_{mo}	angular velocity of the oscillatory PMM motions
$\vec{\mathbf{\Omega}}$	vorticity tensor
ψ	Heading
ψ_1	dynamic part of heading
σ	weighted standard deviation of steady solution history
$\bar{\sigma}$	weighted standard deviation of weighted mean of steady solution history
∇	vessel volumetric displacement
$\lvert\vec{a}\rvert$	absolute value of the arbitrary vector $\vec{a}$
a'	non-dimensionalization of arbitrary value a

1 INTRODUCTION

Under contract W7707-145687/001/HAL, issued by Public Works and Government Services Canada (PWGSC) on behalf of the Technical Authority, DRDC Atlantic, STX Canada Marine (STXM) have completed Computational Fluid Dynamics (CFD) modelling of Planar Motion Mechanism (PMM) manoeuvring tests for the purpose of validation against experimental results.

1.1 OBJECTIVE

In light of the present status of manoeuvring predictive and CFD capabilities, the objective of the proposed work is to determine whether CFD can be used to provide practical and reliable predictions of the manoeuvring forces and moments traditionally measured through PMM model tests. The PMM tests of the DDG51 frigate completed by FORCE Technology [1, 2] provide the basis for this validation study.

1.2 BACKGROUND

While a basic level of manoeuvring performance is essential for the safe navigation of all vessels, the manoeuvring performance of a warship is an integral aspect of the vessel capability. High manoeuvring performance can be leveraged to effect a tactical advantage in combat situations, can improve the safety of ship-to-ship and fleet operations, and can improve performance in peacetime roles requiring launch and recovery operations or performance in high winds or seas.

The ability to accurately describe the manoeuvring performance of an existing warship can help the performance limitations to be better understood by the ship’s captain, so that the vessel’s capability can be exploited more effectively. This quality of information is typically obtained through manoeuvring trials, including standard tests such as turning circles, zig-zag manoeuvres, crash stop manoeuvres, spiral manoeuvres, and more specialized manoeuvres.

An accurate prediction of manoeuvring performance is also important at the design stage, when it remains possible to make design adjustments which can remedy deficiencies in the manoeuvring performance or further enhance the performance. However, trials data is not available for the first-of-class vessel at the design stage, and it necessary to use other means to predict the manoeuvring performance. Manoeuvring performance predictions can be made using physical model tests to directly simulate the trials manoeuvres, with a free-running model. Alternately, either rotating arm tests or planar motion mechanism (PMM) tests can be conducted at model scale with the aim of developing mathematical models of the manoeuvring performance. Although other methods have been used, the most common is based on Taylor series expansion of the dependence of manoeuvring forces on the vessel dynamics (speed, drift rate, rate of turn, rudder angle, etc.), and the tests determine the value of the coefficients, called manoeuvring derivatives, for each term in the expansion. The mathematical models use the series expansions to predict the manoeuvring forces on the vessel, compute propulsion and control surface forces, solve the coupled equations of motion, and numerically integrate in time to provide time-histories of the vessel trajectory.

Manoeuvring model tests are expensive due to the large testing program and the specialized equipment required (such as a free-running model in a large test basin, a rotating arm facility in a suitably large basin, or a planar motion mechanism in a sufficiently wide towing tank). Manoeuvring model tests are therefore typically warranted only late in the design cycle, and possibly not at all for some types of naval vessels.

In the absence of model test data, the necessary data to populate a mathematical manoeuvring model can be approximated using techniques such as regression analysis of data obtained from other (similar) vessels, strip-wise integration of estimated coefficients, and semi-empirical methods to separately account for the effects of appendages. The reliability of these methods is not high, because they often do not provide sufficient account of the specific geometry of the vessel, and the influence it has on the flow patterns and developed forces.

Even manoeuvring model tests results are subject to greater uncertainty than classic resistance and propulsion model tests. In many manoeuvring model tests, the measured loads include the load required to accelerate the vessel, and this must be removed from the measured loads to obtain the pure hydrodynamic loads. Such indirect measurements incur additional error. Also, manoeuvring forces include strong viscous components, so there are difficulties in scaling these results to full scale, when the model velocity is based on Froude scaling.

The prominence of viscous forces has also made it challenging to use numerical techniques to estimate the manoeuvring performance of a vessel; this is in contrast to other aspects of hydrodynamic performance, many of which can be predicted reasonably well under the assumption of inviscid potential flow. This combination of challenges has helped manoeuvring prediction to earn a reputation as a “black art”, with final results have an intricate dependency on coefficients that are difficult to estimate.

Meanwhile, Computational Fluid Dynamics (CFD) has developed from a research tool for use in specialized problems to a routine design tool. Integral aspects of this shift have been the dramatic increase in computational resources, technical developments, and their incorporation into commercially available CFD software. Important developments have spanned the whole range of the CFD workflow, including the direct import of 3D CAD geometry, automated meshing tools including local mesh refinement and specialized meshing models to resolve the turbulent boundary layer, the introduction of the volume of fluid (VOF) approach to modelling free surface flows, the collection of a wide range of physics models within a single program, and integrated post-processing.

Developments in CFD have resulted in excellent accuracy. In 2013, STXM completed an internal validation study of CFD resistance calculations for several different vessels. This showed remarkably good agreement with model test results, with the difference in resistance typically less than 1.3% of the full-speed model resistance.

Considering the challenges in developing manoeuvring predictions in the design stage and the increased maturity of CFD for predicting viscous flows in marine applications, the time has arrived for pursuing manoeuvring prediction with CFD.

The natural progression is that the use of CFD in manoeuvring work be analogous to its use for vessel resistance prediction: CFD can be used to develop the information that would normally be developed using model test procedures. This would allow numerical manoeuvring models to be constructed based on the CFD results in cases where either the level of design maturity or the cost make model testing an unattractive option. It also is the necessary first step, as the replication of model test results with CFD predictions is required to validate the technique. Looking forward, it may be that the future use of CFD for engineering predictions of manoeuvring will not directly follow present model test procedures, as these are constrained by the physical limitations of the testing equipment, and impose some challenges to the CFD analysis.

1.3 SCOPE

This work included reviewing public-domain literature on CFD analysis of vessel manoeuvring for the purpose of guiding the approach taken in the remaining tasks, preparing the hullform and bilge keel geometry, using STAR-CCM+ by CD-ADAPCO to complete CFD simulations of a subset of the steady and unsteady PMM tests in [1], post-processing the results, comparing of the results against previously completed model tests, calculating the spatial discretization errors as described for the Journal of Fluids Engineering [3], and investigating the effect of bilge keels.

2 LITERATURE REVIEW

While CFD is a well-established technique for analyzing some problems, the application of CFD to vessel manoeuvring is a new and developing field. There are relatively few publications in this area, and while different studies show varying degrees of success, some recent papers [4, 5, 6, 7] present promising results for the use of CFD in predicting the ship maneuvering forces.

The following sections review the CFD approaches taken by other researchers, with the aim of providing insight to guide the CFD modelling tasks to be undertaken by STXM in other phases of this project. These include:

- geometry preparation;
- meshing the domain;
- numerical techniques appropriate for capturing all necessary physical phenomena within the fluid domain;
- rigid body motion of the vessel and mesh;
- algorithm for the solution of the fluid flow; and
- solution convergence.

2.1 GEOMETRIC MODELLING

Fabricating a completely symmetric scale model for the tow/manoeuver tank is extremely difficult. The measured forces and moments therefore should be corrected in order to take account of the model asymmetry [4]. Development of a symmetric CAD model, on the contrary, is easy to achieve.

There are many tools in the market for building a marine related geometry from scratch. Among them Rhinoceros3D [8] is the software of choice in STX Marine, while many others are also available [9, 10, 11].

Since building a CAD model is considered a trivial task, the literature does not refer to the software and methodology used but, slight modifications to the originally developed CAD model are normally done within the CAD tool of the CFD software package. For instance, the surface mesh of the CAD model can be improved in STAR-CCM+ software through automated mesh operation. This surface mesh can better represent the original surface of the CAD model and, it further can be used in other automated mesh operations.

2.2 MESHING

CFD requires that a mesh be generated which subdivides the fluid domain into many cells. Two basic approaches for this are structured grids and unstructured grids. A classic structured grid can be envisioned as a large rectangular block that has been sliced several times in each of three directions to subdivide it into an array of cubic cells, then deformed so that one face of the domain matches the shape of the ship’s hull. This approach makes it very simple (and fast) to index individual cells in the domain and their neighbours. For complex geometries, the overall domain may be divided into multiple blocks prior to meshing each block using the above structured approach. Since computations are faster within a structured grid compared to an unstructured grid, the structured body-fitted grid seems to be the grid of choice for CFD simulation of flow around ship models [6, 12, 13]. In a structured gird cells have identifiers in the directions of the coordinate system while in an unstructured grid cells are numbered as they are generated in a consecutive manner. An example of a grid including two overlapping structured blocks is presented in Figure 2.1-a.

For an appended hull body-fitted grids are mostly chimera multi-block [13] which eases the grid generation at the cost of reduced accuracy within the overlapping regions or, mesh morphing [7] which may cause inaccuracy and convergence difficulty at highly skewed cells. A chimera multi-block grid is simply a grid made of more than one block of mesh where the boundaries of the blocks overlap rather than sharing a single surface. An example of chimera grid is presented in Figure 2.1-b; the different colours show several different structured blocks, and the topology allows both rudder rotation and 6 DOF motions of the vessel. In a PMM manoeuvre test an unstructured trimmed mesh can be used either with chimera or with moving mesh [14] where compared with a simple resistance test [14] the near hull mesh is further refined [4].

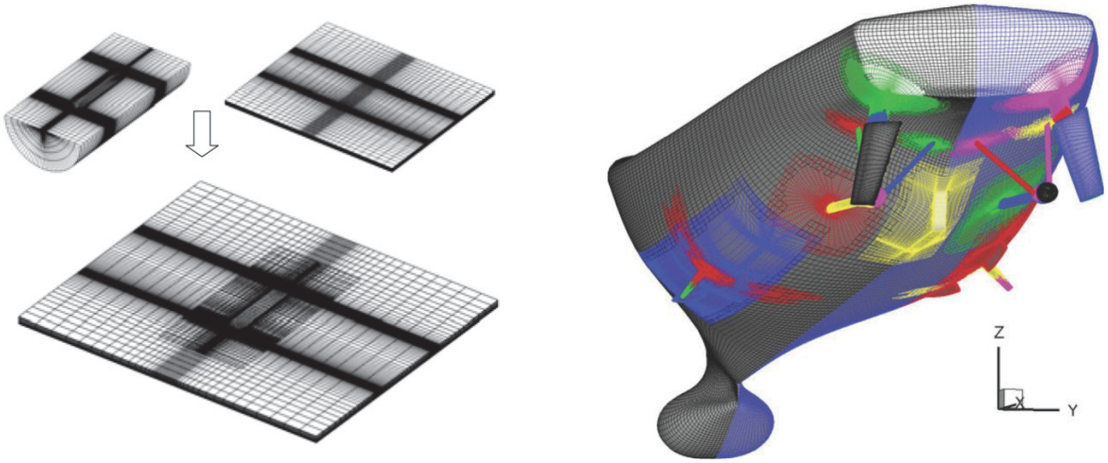

(a) Structured [12] (b) Chimera [13]

Figure 2.1: Grids in Computational Maneuver Tests

Unstructured grids place fewer or no general guidelines on the arrangement of each cell and its neighbours. This frees the meshing process from the confines of a structured grid, which may be difficult to bend to fit complicated geometries while providing sufficient refinement in the desired areas. The use of an unstructured grid seems to be limited to the trimmed mesh [4, 14], which is essentially a structured mesh which is not deformed to match the shape of the hull; instead the cells that intersect with the hull are trimmed by the hull boundary. Trimmed meshes are also typically subdivided in regions where refinement is required. The use of the trimmed meshing approach in ship manoeuvring is due to its capability to capture the sharp interface between the water and air through an effective local refinement while allowing cell size to grow rapidly away from the ship and water surface. This technique, as observed in ITTC guidelines [15], efficiently avoids reflection of the waves on the boundaries. An example of a trimmed mesh is presented in Figure 2.2.

The maximum mesh size reported for the CFD modelling of a PMM test in calm water is 19 million cells [16]. However 1.5 million cells has been recommended as the minimum acceptable number of the cells [4, 17] and, a grid of 4 million cells is suggested as an optimum grid [4]. This is demonstrated, for instance, in [16, 17] where linear derivatives are calculated with enough accuracy using 4 million cells [4, 17]. Even 19 million cells does not appear to give sufficient resolution for accurate calculation of non-linear and acceleration dependent derivatives [16]. These findings suggest the use of the 4 million cells for the available technology, when URANS method is used.

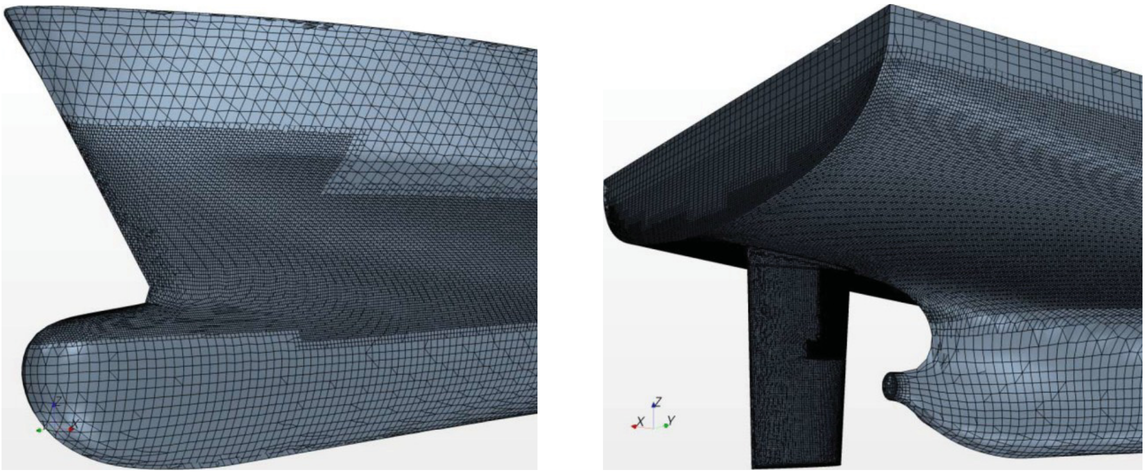

(a) Bow (b) Stern

Figure 2.2: Trimmed Mesh in Computational Maneuver Tests [4]

Most simulations have aimed to replicate PMM tests but some simulations of free-running models have also been undertaken. For the CFD modelling of a free model manoeuvre the optimum number is about 7 million cells and simulation period is of about 50 times longer [13]. This indicates that a PMM test is computationally less expensive compared with a free model.

Since CFD simulation of a manoeuvring test is not yet mature, a mesh refinement study is necessary for identifying the accuracy of the computations [4, 12]. A refinement ratio of $\sqrt{2}$ (this will yield a mesh size ratio of about $2^{3/2}$) is both most practiced [4, 17] and sufficient [3]. The refinement ratio is the ratio of the typical cell size in a given mesh to the typical cell size in the next finer mesh; With base mesh size of 4.2 million cells as a medium mesh, a ratio this yields the coarse and fine meshes of about 1.6 and 9.9 million cells, respectively, which can be used for a grid independency study.

2.3 PHYSICS MODELLING

Physics of a problem forces the required techniques for resolving the flow field in a CFD model. For the CFD simulation of a manoeuvre test, the most important among these techniques are methods for turbulence modelling, interface capturing, near-wall treatment, boundary condition, and initial condition.

2.3.1 Turbulence

Turbulent flows involve flow structures that are inherently three-dimensional, unsteady, and have an extremely wide range of length scales. These are governed by the Navier Stokes equations, and it is possible to simulate the entire flow field (including all scales) using an extremely fine mesh. This technique, Direct Numerical Simulation (DNS) of a flow field, demands an exceptionally high computational resource, and has only been completed for flows very much smaller than the flow around a ship.

With existing computational resources, it is necessary instead to use an approximation to account for turbulence. Large Eddy Simulation (LES) uses a mesh that resolves only the larger eddies, while using a simplified approach for the smaller length scales, and is still considered a demanding technique for a large-scale engineering project. Detached Eddy Simulation (DES) and Unsteady Reynolds Averaged Navier-Stokes (URANS), on the contrary, require less computational resources and reveal adequate accuracy for most of engineering applications. DES resolves only the larger eddies which are outside the boundary layer, while URANS uses a eddy viscosity model to account for all turbulent flow structures.

Neither using 4 million cells in [17] nor using 19 million cells in [16] could result in a significant improvement in the accuracy of the computed forces and moments when DES was used over URANS. An inadequate mesh size was suggested as one of the reasons behind insufficient accuracy of computations [16]. Although this may be the case for DES method due to its higher demand for mesh density compared with URANS method, the use of URANS method in CFD calculations does not show significant improvement in computation accuracy when mesh size is changed from 2.5 million cells to 19 million cells; see [16] on page 10. Another reason behind inaccuracy of computations is believed to be the use of the isotropic turbulence models [16], an idea that could not be concluded in [17] after comparing several techniques.

Since the use of DES method has not been shown to significantly improve the accuracy of computations, URANS methods seem to be of more interest for engineering applications due to their significant lower demand for computational resources [4, 12, 13].

A strong dependency has been observed for both the resistance and the velocity field on the turbulence model [15], making an appropriate choice of the URANS model essential. Compared to the other URANS methods, the SST $k-\omega$ turbulence model [18] effectively blends the accurate formulation of the $k-\omega$ model in the near-wall region with the free-stream independence of the $k-\varepsilon$ model in the far field, thus is more appropriate for the external flows with severe separation. This model has been the model of the choice in the recent CFD simulations for the manoeuver test when URANS method was used [4, 13].

2.3.2 Interface Capturing

When modelling a manoeuver in CFD, ignoring the interface between the water and air will cause a significant computational inaccuracy at high Froude numbers. A technique then is required for capturing the interface when a significant displacement in water surface is expected.

There are several interface capturing methods, which can be classified as single phase or multi-phase. Single phase methods are computationally less demanding since flow field can be resolved only within the liquid phase. The drawback of this method is the inaccuracy near the interface since variables (pressure for instance) have to be extrapolated to the interface. An example of the application is the use of the single phase Level-Set method in CFD simulation of a manoeuver test [6, 13]. A two-phase interface capturing method such as the two-phase Volume Of Fluid (VOF) method, on the contrary, provides a higher computational accuracy near the interface at the expense of a higher computational demand. Two-phase VOF is the method of the choice in many commercial solvers [19, 20] and is used, for instance, for the CFD modelling of flow around ship model in [4, 5].

2.3.3 Near-Wall Treatment

Since Navier-Stokes equations are parabolic, information propagates from the boundaries into the interior of a domain both in time and space. The main source of the turbulence production is near the wall boundaries and, in turn, any failure in accurately simulating the near wall flow can influence the entire solution.

Solving the flow field with a universal dimensionless wall normal distance, y^+, of less than 1 requires a very fine near-wall mesh, and is computationally expensive. Although the use of a wall function approach, the standard wall function approach in [21] for instance, will efficiently mitigate this problem and is considered an acceptable technique in ITTC guidelines [15], the near-wall cell y^+ must be always above 11.62. This will limit the choice of the near wall mesh size which is not always practical. An automatic wall treatment, on the contrary, uses a blending function for a smooth transition from the laminar boundary/sub-layer, $y^+ < 1$, to the turbulent region, $y^+ > 11.62$. Even though this will solve the problem when mesh size is uniform, difficulty may arise when two neighboring cells do not have the same size. In such condition, the calculated wall shear stress in neighboring cells will not be the same while physically it can be (for instance, on a flat plate it has to be). Thus, the choice of the near-wall mesh size remains important. It should be noted that $y^+ = 11.62$ is the intersection point between the log-law layer and the laminar sub-layer and a commercial CFD solver may use a different y^+ value. The use of automatic wall treatment is the practical way of dealing with the near-wall flow in CFD simulation of a manoeuver test [4, 13, 17].

2.3.4 Boundary Conditions

At a boundary, flow variables can be produced, transferred into the domain, or carried out of the domain. Regardless of these characteristics, all boundary conditions reveal an important attribute in a two-phase flow; i.e. they either reflect or do not reflect surface waves. Among all boundary conditions only the outlet boundary condition can allow surface waves to exit without reflection. Wave reflection from the boundaries can influence the accuracy of the solution. Thus, provisions are required for preventing wave reflection.

Using a coarse mesh with a cell size equal to or greater than the wave length is the simplest way of damping a wave. While numerical wave absorbers exists [22], increasing the mesh size away from the body is the practical approach in CFD simulation of flow around a ship model [4, 12, 13].

2.4 MOTION SIMULATION

The ship model in a planar motion has a minimum of three degrees of freedom. The two additional motions of heave and pitch are sometimes accounted for within the CFD simulation of a PMM manoeuver test [17] while the roll motion is usually ignored [4, 17].

The trajectory of a ship model is calculated in the ship-fixed coordinate system by solving the equations of motion for the degrees of freedom which are not prescribed [17]. For a given body of specific mass and moment of inertia these equations relate the forces and moments acting on the ship model to its motions. In this project however, the heave and pitch will be fixed, so further review of formulations for the equations of motion is unnecessary.

2.5 SOLUTION ALGORITHM

For the flow field around a moving body the solution algorithm includes procedures for solving flow variables, integrating forces and moments on the moving body, moving the body, moving the mesh when it is relevant, and transferring the flow information between the meshes when applicable.

2.5.1 Flow Solver

Riemann solvers, even though applied to flow fields with parabolic equations, were originally developed for invicid and shallow flows where diffusive terms are ignorable and flow equations are hyperbolic. Treating the diffusive terms of the transport equations as source terms converts the parabolic flow equations to hyperbolic equations (even though not physically but, mathematically) and makes the use of Riemann solvers possible for the flow around ship model, at least when free surface is ignorable [12].

Finite volume method of SIMPLE family (Semi-Implicit Method for Pressure-Linked Equations), on the contrary, is the solver of choice for incompressible viscous flows where flow equations are parabolic. This solver is successfully applied to the simulation of flow around ship models [4, 5, 13, 17].

2.6 CONVERGENCE

Since convergence of a CFD solution is project specific and subject dependent [14], residual reduction by three orders of magnitude as reported in [17] (independent of how the residual is defined) may neither be possible nor required. For instance, if the objective of the CFD simulation of flow field around a ship model is prediction of the steady hull resistance, the solution can be considered as converged when forces converge to a steady value and do not change by reducing the time step. For the CFD prediction of a manoeuvring test as in [6, 13] when chimera grid is used, residual reduction may not be possible since due to the transfer of information between different grids the solution may not be conservative. Selection of a smaller time step as well as placing the boundaries of a chimera grid far enough from the moving body will mitigate this problem [14].

3 METHODOLOGY

The methodology for this project has been guided primarily by the objective of producing an accurate CFD representation of the PMM model tests completed by FORCE Technology. While this implies that many of the aspects of the simulations are prescribed to match the model tests, the accuracy and efficiency of CFD simulations is dependent on the expert selection of a large number of numerical modelling parameters. This section describes the methodology used to achieve this, as well as the details of post-processing intended to yield a meaningful comparison against the model test results.

CFD modelling of the PMM manoeuver tests started with modifying the CAD model [23] in Rhinoceros software. The modified model was exported to Parasolid *.x_t file format which then was imported in STAR-CCM+. The computational domain and mesh were developed in STAR-CCM+ and, physics, motions, and pre-run post-processing have been set up. The raw CFD results were further processed using Octave and Microsoft Excel.

3.1 EXPERIMENTAL DATA SOURCE

Reference [1] by FORCE Technology was cited in the contract as the experimental data source against which CFD is to be validated. The report provides the model test results as well as a detailed experimental error analysis. The simulation matrix in Section 3.2 and overall CFD setup including aspects such as the prescribed motions is in accordance with [1].

In addition to this, the SIMMAN 2014 workshop was discussed in the kickoff meeting as a data source. After arranging access to the SIMMAN 2014 FTP site, raw data files from the same model tests were downloaded from it [2, 23]. A significant inconsistency is found between the data reported in the report [1] and the raw data available in data files in the FTP site [23]. An example of this inconsistency is presented in Figure 3.1 for the lateral force, Y, measured in the dynamic yaw and 10° drift test. The results were also compared with the measurements from a separate set of PMM tests of the same vessel completed by INSEAN [24], when possible, in order to check the accuracy of the computed data. Although in many cases the computed data are closer to the INSEAN measurements [24], inaccurate measurements could as well be observed in the INSEAN data which made the comparison very difficult.

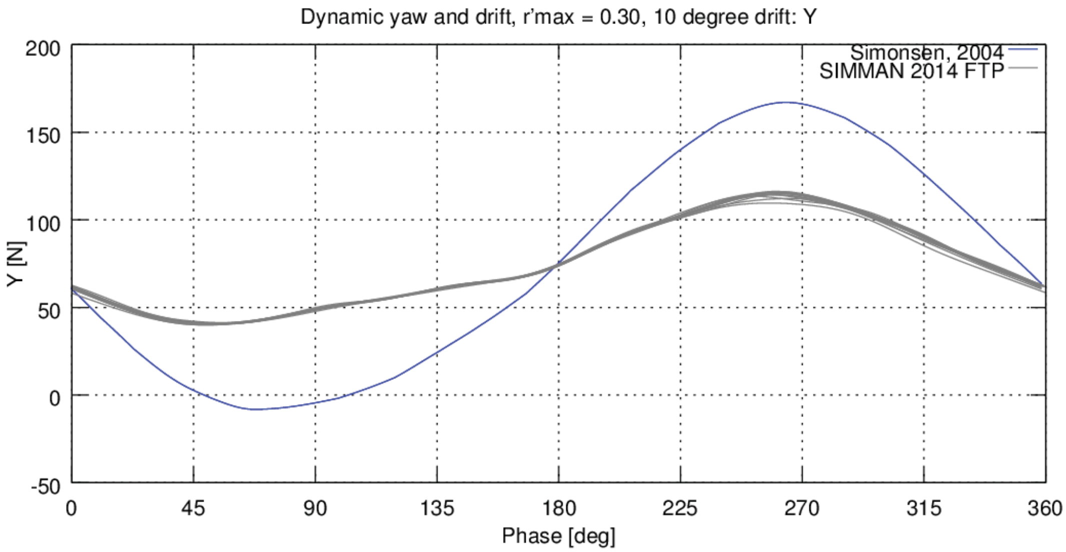

Figure 3.1: Inconsistency of Model Test Results

3.2 SIMULATION MATRIX

The simulation matrix for the present CFD analyses is a subset of the model tests, comprising cases with a Froude number of 0.28, and without including negative drift angles. The tests completed include:

- Steady drift with drift angles of 0, 2, 6, 9, 10, 11, 12, 16, and 20 degrees;
- Unsteady pure sway with non-dimensional sway velocities of 0.03, 0.07, and 0.17;
- Unsteady pure yaw with non-dimensional yaw velocities of 0.05, 0.15, 0.30, 0.45, 0.60, and 0.75; and
- Unsteady yaw and drift with a non-dimensional yaw velocity of 0.30 and drift angles of 9, 10, and 11 degrees.

The details of these tests are presented in Table 3.1 through Table 3.4. Tests marked with * were simulated with three different levels of mesh refinement to allow the calculation of the spatial discretization errors. Tests marked with ^{BK} were completed both with and without bilge keels.

The parameters shown for the unsteady tests are specific settings used in configuring the PMM for the model tests. These achieve the shown non-dimensional sway and yaw velocities only to the number of significant digits shown. To preserve consistency with the model tests, the PMM settings have been directly used in the CFD analysis; details of this are provided in Section 3.10.

Table 3.1: Static Drift Simulation Matrix

F_r [-]	U_c [m/s]	β [deg.]
0.280	1.7536	0, 2, 6, 9, 10*^{BK}, 11, 12, 16, 20

Table 3.2: Unsteady Yaw and Drift Simulation Matrix

F_r [-]	U_c [m/s]	β [deg.]	$N - PMM$ [rpm]	S_{mm} [m]	Y_{mm} [m]	Run [#]
0.280	1.7536	9	7.0	0.2148	0.0897	10
0.280	1.7536	11	7.0	0.2148	0.0897	11
0.280	1.7536	10	7.0	0.2148	0.0897	12*^{BK}

Table 3.3: Unsteady Pure Yaw Simulation Matrix

F_r [-]	U_c [m/s]	β [deg.]	$N - PMM$ [rpm]	S_{mm} [m]	Y_{mm} [m]	r'_{max} [-]	Run [#]
0.280	1.7536	0	7.0	0.0358	0.0150	0.05	4^{BK}
0.280	1.7536	0	7.0	0.1074	0.0449	0.15	5
0.280	1.7536	0	7.0	0.2148	0.0897	0.30	6
0.280	1.7536	0	7.0	0.3222	0.1346	0.45	7
0.280	1.7536	0	9.0	0.2599	0.1396	0.60	8
0.280	1.7536	0	9.0	0.3249	0.1745	0.75	9

Table 3.4: Dynamic Pure Sway Simulation Matrix

F_r [-]	U_c [m/s]	β [deg.]	$N - PMM$ [rpm]	S_{mm} [m]	Y_{mm} [m]	v'_{max} [-]	Run [#]
0.280	1.7536	0	7.0	0.0418	0.0	0.03	1^{BK}
0.280	1.7536	0	7.0	0.0835	0.0	0.07	2
0.280	1.7536	0	7.0	0.2079	0.0	0.17	3

3.3 COORDINATE SYSTEMS

Several different coordinate systems have been used in this analysis. The alignment of the different coordinate systems follows the decomposition of the vessel heading into two parts, as described in the model test report [1]. This provides the vessel heading, ψ, as the sum of the dynamic yaw angle, ψ_1, and the steady drift angle, β, such that $\psi = \psi_1 + \beta$. This is illustrated in Figure 3.2. For all simulations, the initial condition was $\phi_1 = 0$. Further details of the vessel and coordinate system motion for the unsteady simulations are discussed in Section 3.10.

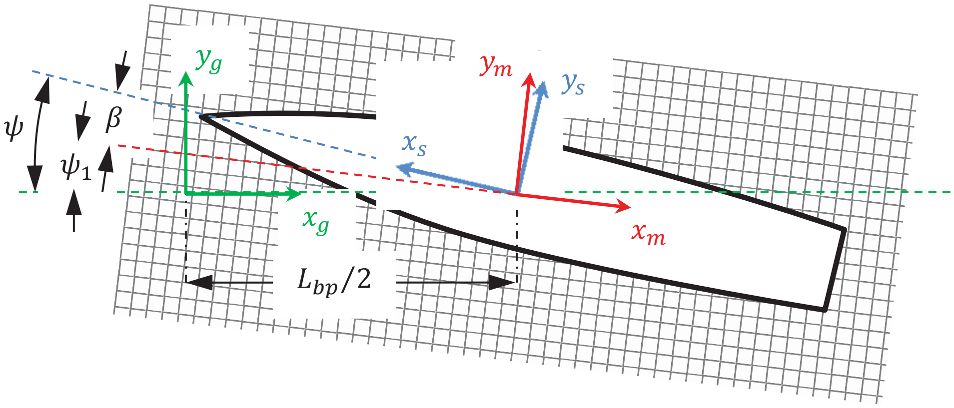

Figure 3.2: Coordinate Systems in STAR-CCM+ Models

The coordinate systems include:

- Ship coordinate system
    - Used for measuring forces and moments acting on the vessel, as it matches the model coordinate system in the model test report [1]
    - Moves with the vessel
    - Remains aligned with the vessel, such that it is rotated an angle $\psi = \psi_1 + \beta$ clockwise[1] of the global coordinate system
    - Origin remains amidships, on the calm waterline, and on centreline
    - Right-handed
    - x_s is positive forward
    - y_s is positive to starboard
    - z_s is positive down
    - Forces X and Y aligned with x_s and y_s, respectively
    - Moment N positive clockwise[1]
- Moving mesh coordinate system
    - Moves with the vessel (and mesh)
    - Remains aligned with the mesh, such that it is rotated an angle ψ_1 clockwise[1] of the global coordinate system
    - Origin remains amidships, on the calm waterline, and on centreline
    - Right-handed
    - x_m is positive in a direction β counterclockwise[1] of astern
    - y_m is positive in a direction β counterclockwise[1] of starboard

---

[1] As viewed from above, looking straight down at the vessel.

- ○ z_m is positive up
- Tank (or global) coordinate system
    - Remains fixed in space
    - Remains aligned with the (hypothetical) towing tank
    - Origin is on the calm waterline, and initially set such that amidships (and the origins of the mesh and ship coordinate systems) lies at an x_g-coordinate of $L_{bp}/2$ at the beginning of the steady simulations.
    - Right-handed
    - x_g is positive in the direction opposite to the carriage motion
    - y_g is positive on the starboard side
    - z_g is positive up
- Vessel geometry (IGES file)
    - Matches the coordinates of the IGES file in which the model geometry was provided
    - Origin located at the FP, baseline, on centreline
    - Right-handed
    - x is positive aft
    - y is positive to starboard
    - z is positive up

The angle β between the mesh coordinates and the ship coordinates required that the orientation of the ship coordinates, denoted "Report CS" in STAR-CCM+, be manually updated for each drift angle, β.

3.4 MODEL GEOMETRY

The particulars of the model of the DDG51 frigate used in the model tests [1] are presented in Table 3.5.

Table 3.5: Model Geometry

Model	FORCE Tec.
Scale	1:35.48
L_{bp} $[m]$	4.0023
L_{wl} [m]	4.0083
B_{wl} $[m]$	0.5382
T_m $[m]$	0.1736
∇ $[m^3]$	0.1897

The basis for the CFD geometry is the IGES file for the bare hull, as downloaded from the SIMMAN 2014 FTP site [23] (folder: "5414 Hull (Bare)"; file: "5415.igs"). The IGES file includes one surface for the main hull, shown in blue in Figure 3.3, and a second surface for the bow, shown in red. In order to successfully build a CFD mesh for the hull, these surfaces needed to be joined to each other and to a new deck surface to fully enclose the hull volume. It is essential that the resulting hull description be watertight: i.e. that the edges of the surfaces forming it touch exactly, with no gaps, no overlaps, and no unconnected edges.

However in the IGES geometry, the forward edge of the blue main hull surface extends forward past the aft edge of the red bow surface, forming an overlap. Additionally, the two surfaces do not exactly intersect. The actual intersection between the two surfaces is shown in cyan in Figure 3.3. The figure also highlights the faintly visible gap at deck level between the forward end of the blue main hull surface and the red bow surface. As the two surfaces are closer to touching at the aft edge of the red bow surface, the aft edge of the main bow surface was used as the nominal intersection between the two surfaces. Rhinoceros3D software [8] was used to trim the main hull surface to this intersection curve, and to ensure the join between the two surfaces is watertight.

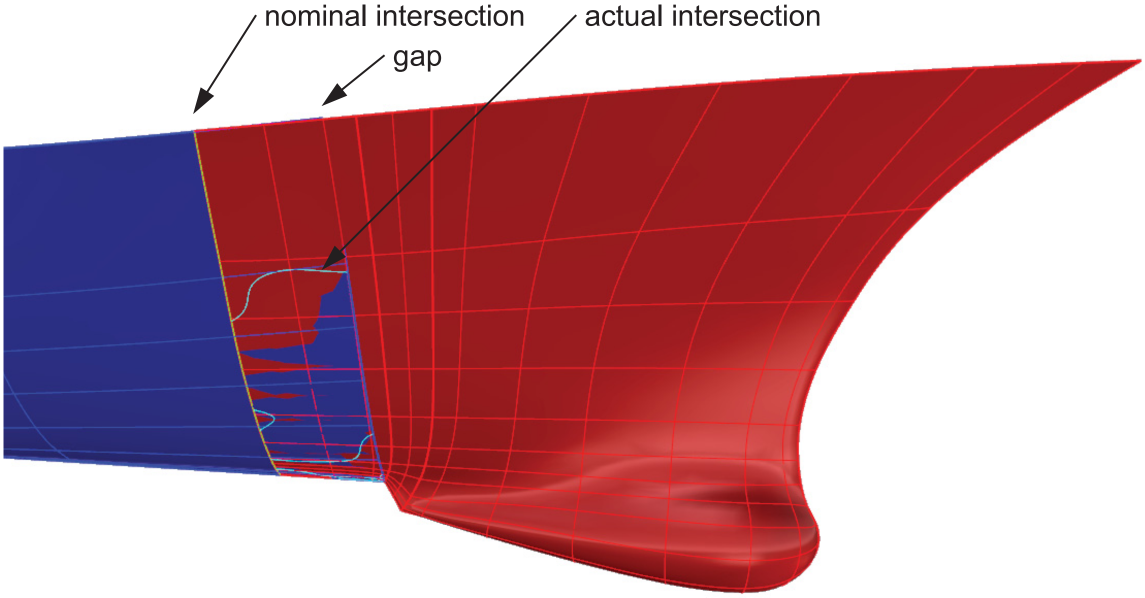

Figure 3.3: IGES Geometry

Rhinoceros3D was also used to develop a 3D model of the bilge keels based on the 2D CAD drawings; these were downloaded from the SIMMAN 2014 FTP site [23] (folder: "5414 Bilge keels B (Bare hull)"; file: "5415 Bilge Keel.dwg"). In modeling the bilge keels, a minor modification was made: the inner plate was extended to meet the end of the outboard plate, rather than leaving a 0.111" long tab tangent to the end of the outer plate. This modification is because the thin tab is smaller than the expected mesh size in the area, and is of the sort of modification typically made for CFD analysis; the change is shown in red in Figure 3.4.

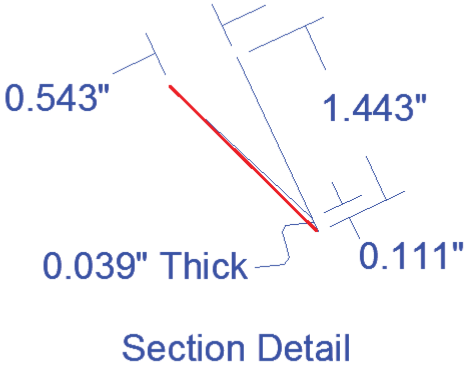

Figure 3.4: Bilge keel geometry, with modification showing in red

The completed hull geometry including bilge keels is shown in Figure 3.5.

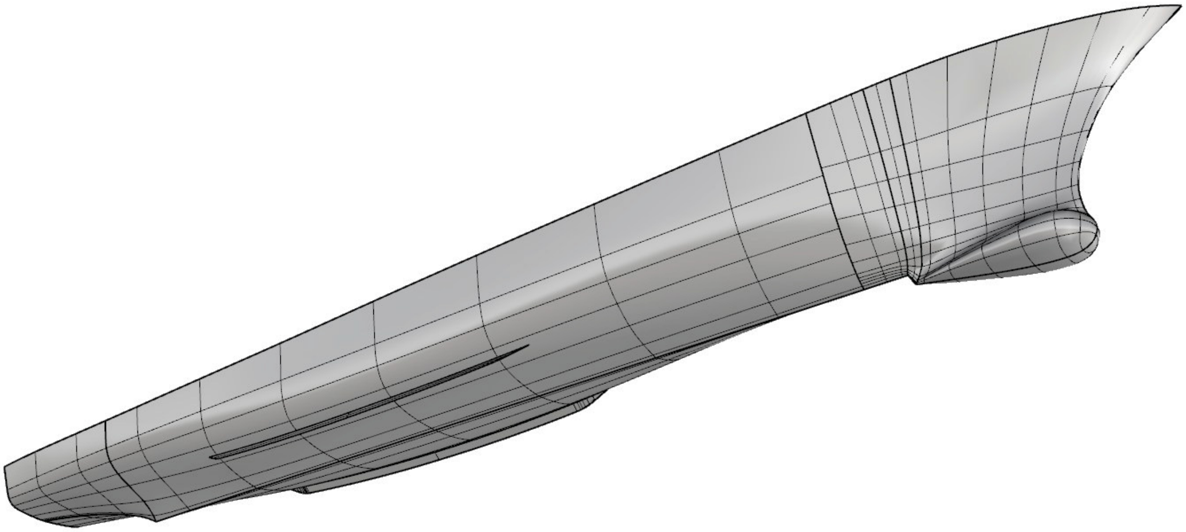

Figure 3.5: Hull Geometry

The geometry was scaled in Rhinoceros3D to account for the difference between the IGES geometry scale of 1:24.83 and the scale factor of 1:35.48 used in the FORCE Technology model tests [1] and in these simulations.

3.5 SINKAGE AND TRIM

At the time this project was initiated, STAR-CCM+ did not have the capability of modeling motions with some degrees of freedom prescribed (by the PMM) and other degrees of freedom free. As a result, it was not possible to conduct PMM simulations with free pitch and heave. Improvements made to STAR-CCM+ during the course of the project have removed this restriction, so free sinkage and trim is a potential avenue for future work. The simulations were completed with fixed sinkage and trim, using values reported in the model tests. For the unsteady simulations, the mean sinkage and trim was determined from the model test data.

To achieve the required draft and trim, the model was first shifted vertically to its draft at the AP. Then the model was rotated about the AP to achieve its draft at the FP. The details of this transformation are presented in Table 3.6 to Table 3.9, where the data is presented with the same order as the data in Section 3.1.

Table 3.6: Draft and Trim in Steady Drift Tests

β [deg]	AP Draft [m]	Trim by bow [deg]
0	0.17963	-0.01686
2	0.17936	0.04291
6	0.18057	0.05632
9	0.18134	0.03084
10	0.17974	0.11984
11	0.18097	0.09521
12	0.18129	0.13103
16	0.18107	0.23562
20	0.18269	0.37890

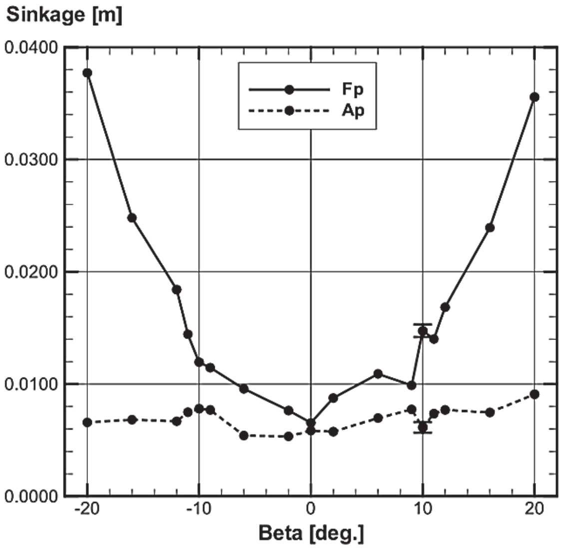

Positive sinkage corresponds to an increase in draft.

Figure 3.6: Sinkage in Steady Drift Tests [1]

Table 3.7: Draft and Trim in Unsteady Yaw and Drift Tests

Run [#]	AP Draft [m]	Trim by bow [deg]
10	0.189631	0.182694
11	0.193192	0.227307
12	0.190569	0.185924

Table 3.8: Draft and Trim in Unsteady Pure Yaw Tests

Run [#]	AP Draft [m]	Trim by bow [deg]
4	0.179442	-0.028922
5	0.185517	0.075555
6	0.181671	0.078397
7	0.187004	0.107000
8	0.187553	0.154961
9	0.189927	0.187421

The calculated draft and trim at the AP for the drift angle of 0 degree in Table 3.6, however, do not match the sinkages extracted from the reported data in Figure 3.6. When the trend of the sinkages at other drift angles is followed, the draft and trim calculated from the data in Figure 3.6 (0.17941 m and 0.00960°, respectively) are more realistic compared with the ones presented in Table 3.6. Simulations were then performed for both conditions in order to identify their influence on the computed forces and moments.

Table 3.9: Draft and Trim in Unsteady Pure Sway Tests

Run [#]	AP Draft [m]	Trim by bow [deg]
1	0.181216	0.042999
2	0.180186	0.036464
3	0.185061	0.095996

An error in the initial setup of the unsteady simulations was found late in the project. This resulted in incorrect draft and trim, and is discussed in detail in Section 5.1.

3.6 DOMAIN GEOMETRY

The Rhinoceros3D hull geometry model, described in Section 3.4, has been imported into the CAD environment of the STAR-CCM+ software, scaled to the appropriate scale, sunk and rotated at A_p as per Section 3.5, and rotated to the drift angle β.

With the exception of CAD import, all operations were performed parametrically so that an automatic operation is possible from outside of the STAR-CCM+ CAD environment. This facilitated the changes from one CFD run to the other.

All volumes required for volumetric mesh refinement control, with the exception of the one for the wave refinement purpose, were also developed in STAR-CCM+ CAD environment and rotated, parametrically, to the drift angle β. For the steady drift case, the volumetric control for the wave refinement was developed within the Part environment of STAR-CCM+ such that it is suitable for any drift angle up to 20 degree. For the unsteady tests, this volumetric control was developed within the STAR-CCM+ CAD environment and parametrically translated to an appropriate position (when applicable) so that it covers the viscous refinement zone and can be adapted in order to take account of the model static drift angle.

The developed CAD geometries were then transferred to the Part within STAR-CCM+. Further automatic mesh operation was performed on parts in order to develop the domain as well as appropriate volumetric controls.

3.7 MESHING

Two automated meshing methods have been developed; a surface mesh for the model and a volumetric mesh for the domain. As soon as each model geometry (including slight changes due to sinkage, drift angle, or bilge keels) was passed from the CAD to the Part within STAR-CCM+, its surface was re-meshed in order to guaranty a high quality surface definition for the subsequent automated mesh operations.

The Trimmer mesh generator was chosen for the volume mesh generation. The Trimmer mesh makes it possible to lay very thin meshes near the interface between the water and air, specifically at distances far away from the model, thus reduces the number of the required volume cells while preserving the numerical accuracy. The HRIC VOF model in STAR-CCM+, which is recommended in CD-adapco's training course [14] for steady solutions, is also more appropriate for a mesh generated by Trimmer.

For the steady drift tests, the longest wave generated by model has a wave length of 1.97 m and an effective wave height of 0.4 m. The wave length was calculated with Equation 3.1 while the wave height was initially assumed not to be more than half of the freeboard.

$$\lambda = \frac{\vec{u}_{s_g}^2}{2\pi \mathrm{g}} \cos^2 \theta \tag{3.1}$$

The assumed wave height was later examined after running the solver for the cases with the drift angle of 0 and 10 degrees. When the actual wave height was observed, the height of the refinement zone was chosen to be slightly larger than the observed wave height. The exception was the wave height near the bow and stern where some local refinement blocks were added in order to achieve sufficient refinement near the water surface. The same strategy was followed in unsteady tests where an initial coarser mesh was used to identify the local spots where further refinement near the water surface is required.

The extension of the required wave refinement zone was identified using an estimate of the wave generated during each test. This is discussed further in detail in Section 3.7.2.

The meshes used for the mesh refinement study in steady drift and unsteady tests are presented in Table 3.10 and Table 3.11, respectively. Since automated mesh generation has been implemented for building the Trimmed mesh, the different meshes in Table 3.10 and Table 3.11 were generated by changing the base size with the refinement ratio of $\sqrt{2}$.

The volume growth rate shown in the right-hand column of each table indicates the number of layers neighbouring cells of the same size in regions where the mesh is growing. The changing growth rates preserve approximately the same mesh refinement ratio through the growth region. An example of the mesh generated near the bow of the vessel is presented in Figure 3.7.

Table 3.10: Steady Drift Test's Mesh Characteristics in Refinement Study

Mesh	Base Size	Cells on Wave		Surface Target Size	Mesh Size	Volume Growth Rate
		Height	Length			
	[m]	[-]	[-]	[m]	[× 10^6]	[-]
Coarse	0.0105	19	47	0.021	1.6	2
Medium	0.0074	27	66	0.015	4.2	3
Fine	0.0053	38	94	0.011	9.9	4

Table 3.11: Unsteady Test's Mesh Characteristics in Refinement Study

Mesh	Base Size	Cells on Wave		Surface Target Size	Mesh Size	Volume Growth Rate
		Height	Length			
	[m]	[-]	[-]	[m]	[× 10^6]	[-]
Coarse	0.0148	13	33	0.030	0.95	2
Medium	0.0105	19	47	0.021	2.24	3
Fine	0.0074	27	66	0.015	5.67	4

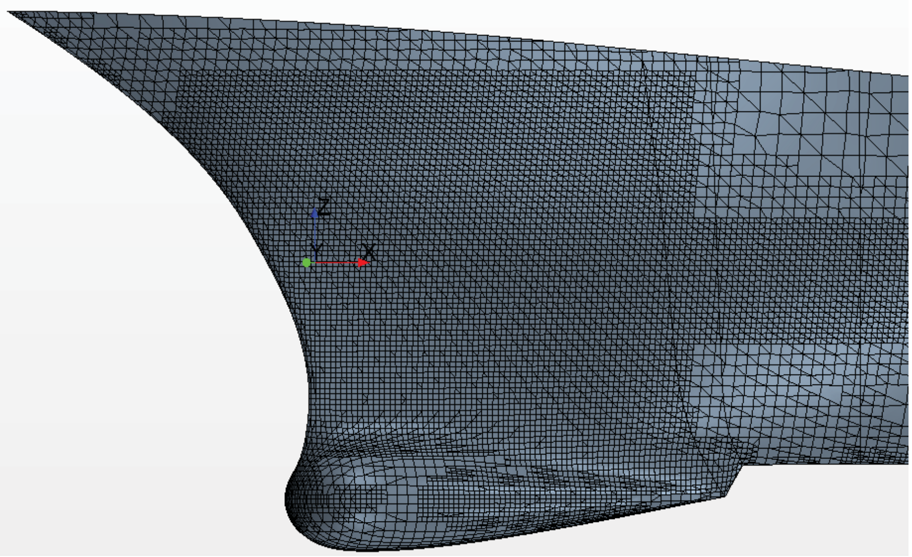

Figure 3.7: Bow Mesh in Unsteady Tests

3.7.1 Prism Layer

An appropriate near wall cell size was chosen with regard to the requirements of the wall-function approach and a prism mesh of three layers, with a growth rate of 1.3 (ratio of neighbouring cell sizes), was used for the near wall treatment on the model hull. Since the wind force on model deck is significantly smaller than the force acting on model hull by water, no prism layer mesh was generated for the model deck. The details of the prism layer mesh are presented in Table 3.12; the details of calculations for the near-wall cell size are presented in Section 3.8.

The thickness of the cells touching the hull boundary was maintained constant in the mesh refinement study. This was chosen to because changes in y^+ due to different near-wall cell thicknesses would affect not only the spatial discretization errors, but also the modelling errors associated with the selection of different turbulence boundary conditions for different values of y^+. It was decided that the modelling errors should not be altered in the mesh refinement study.

Table 3.12: Prism Layer Mesh

Layer No.	Cell Size [m]
1	0.0017
2	0.00221
3	0.002873
Layer thickness	
Sum	0.006784

3.7.2 Wake Estimate

Prior to generating a mesh, a first-principles estimate of the unsteady free surface wake was completed for each test. For the steady simulations, this is simply the Kelvin wake pattern initiating at the forward perpendicular, and contained within triangular envelope (a roughly 19° angle) expanded aft and transversely.

For the unsteady simulations, the estimation of the wake is more complicated. The Kelvin wake envelope was adjusted to account for the unsteady motion of the forward perpendicular. This involved using the instantaneous velocity of the FP to determine how the wake generated at a given time propagates and is observed at later times, including establishing the relative direction of propagation of the wake energy that lies on the envelope of the wake pattern. This is illustrated for the case used in the mesh refinement study, yaw + 10° drift, in Figure 3.8. The figure shows several curves, with each representing the wake envelope for a different instant in time. Processing has not been implemented to remove the visible overlapping areas.

The results were then transformed into a coordinate system that is aligned with the CFD mesh. This is fixed to the ship, but has a fixed rotation with respect to the ship set by the drift angle. This shows which parts of the CFD mesh would be influenced by the free surface wake. An example of this, again with the yaw + 10° drift case, is shown in Figure 3.9. The red and green vectors shown in the figure indicate the possible range of relative flow directions that would be experienced (maximum and minimum flow angle) at various locations in the ship-fixed reference frame.

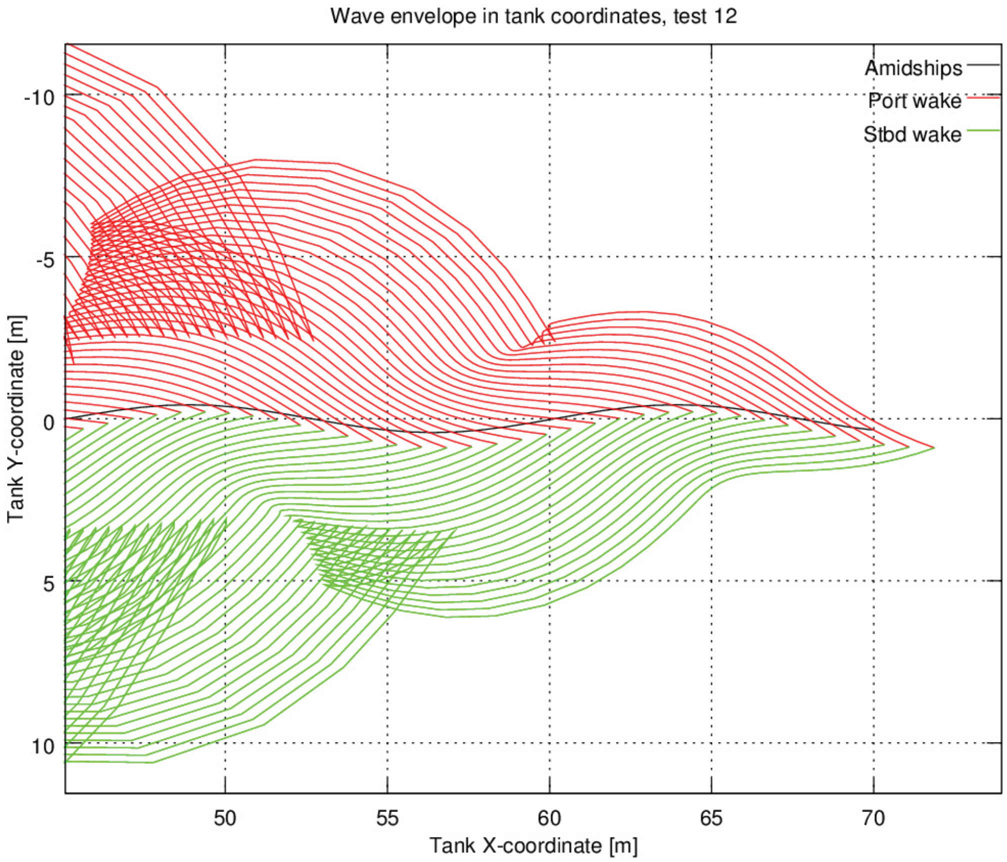

Figure 3.8: Estimated Wake in Tank Coordinates; Yaw + 10° Drift

As might be expected, it was found that dynamic yaw has a strong influence on the wake as plotted in mesh-aligned coordinates, while dynamic sway has a smaller influence. The estimated wakes have been used in selecting the size and shape of the volume specifying the free surface mesh refinement, to help ensure the free surface wake is retained within the refinement volume, while avoiding the refinement of areas not influenced by the free surface wake. The refinement zone was extended slightly further than the estimated wake, because in some cases it could be seen that the wake prediction based on the motion of the forward perpendicular fell within the shoulders of the vessel. Also it can be expected that the estimated envelope might loosely align with a wave crest, so the actual free surface disturbance could be on the order of one quarter wavelength further ahead.

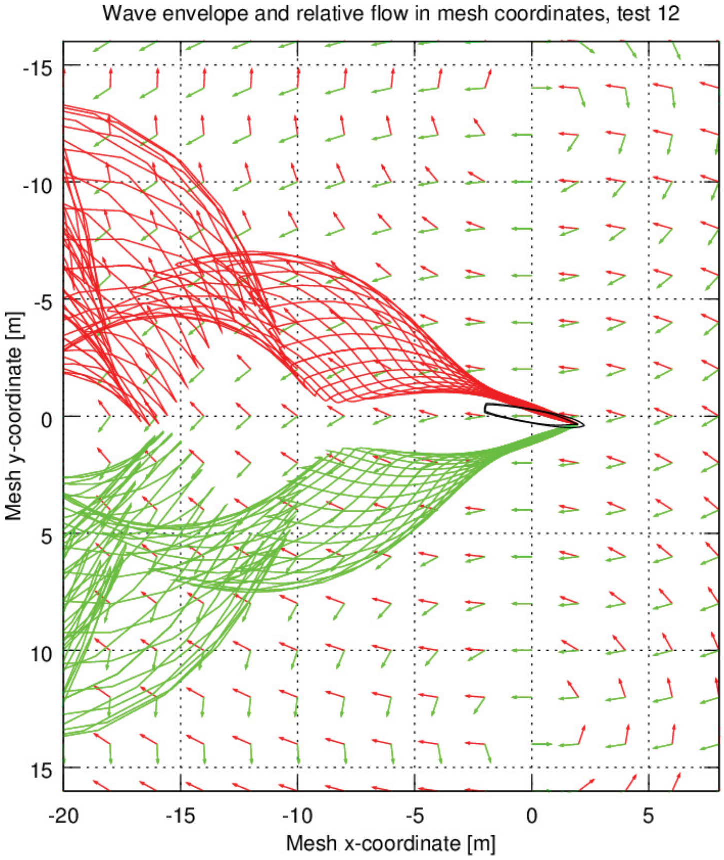

Figure 3.9: Estimated Wake in Mesh-Aligned Coordinates; Yaw + 10° Drift

It was initially thought that the overall domain size and shape would need to be selected carefully to avoid the free surface wake propagating out boundaries other than the outlet downstream, and to avoid as much as possible the incidence of reverse flow through the boundaries (flow into an outlet, or out of an inlet). However the steady simulations showed that the gradual coarsening of the mesh towards the outer boundaries was very effective in eliminating the wake near the boundary. It was therefore not as important to ensure the above criteria were met. Nonetheless, the domain geometry was selected to such that the predicted free surface wake would flow out the outlet.

3.8 PHYSICS

The SST $k-\omega$ model was used for simulating turbulence with the $All-Y^{+}$ model for the near wall treatment. For the steady drift tests, the interface between the water and air is captured through HRIC VOF method where the mesh near the interface is sufficiently refined in order to minimize smearing effect of the VOF method on the free surface. In the unsteady tests, a mix of HRIC and second order upwind scheme was used; this is consistent with the CD-adapco training course [14]. In the mixed method HRIC technique was used when $CFL \leq 0.5$, and second order upwind scheme was used when $CFL \geq 1.0$. For $0.5 \leq CFL \leq 1.0$ a mix of HRIC and second order upwind scheme was used.

The environmental conditions as well as the physical properties of the domain were chosen in accordance with the model tests [1]; see Table 3.13. An exception to this is gravitational acceleration. The local gravitational acceleration was not measured at the towing tank, but a value of 9.81 m/s² was used in the model test analysis in [1]. While discrepancies between these two are a source of error in the non-dimensional physical model test results, the significance is expected to be very small. A gravitational acceleration of 9.806 m/s² was selected for both the CFD analysis and post-processing.

Table 3.13: Domain Environment and its Physical Properties

Environment

T_0 [°C]	P_0 [Bar]	Gravity [m/s^2]
15.7	1	9.806

Physical Properties

Material	Density [Kg/m^3]	Dynamic Viscosity [Pa.s]
Water	998.9	0.0011180
Air	1.217	0.0000177

3.9 INITIAL AND BOUNDARY CONDITIONS

For both steady and unsteady tests the drift angle was statically introduced through suitable geometry alignment and meshing techniques. This technique minimizes the transient between the steady and unsteady parts of the simulation in an unsteady test. It also permits the steady part of the simulation in an unsteady test to be used in simulation of another unsteady test with a similar drift angle. This technique is depicted in Figure 3.10 for an unsteady test; where, t is the simulation time, and t_{std} indicates the end of the steady part in simulation of an unsteady test. The equation of transvers motion in the global coordinate system for an unsteady test is also modified as in Equation (3.2).

$$\eta_{PMM} = -2S_{mm}(-1 + \sin(\omega_{mo}\tau)) \tag{3.2}$$

where S_{mm} is a distance related to the measurement equipment, ω_{mo} is the angular velocity of the oscillatory PMM motion, and τ is the time for unsteady part of the simulation in an unsteady test. Although it is possible to dynamically introduce the drift angle in simulation of an unsteady test, it will require slight modification to the wave refinement zone, it causes poor flow condition near the pressure outlet boundary, and it prevents the steady part of the simulation in an unsteady test to be used in another unsteady test.

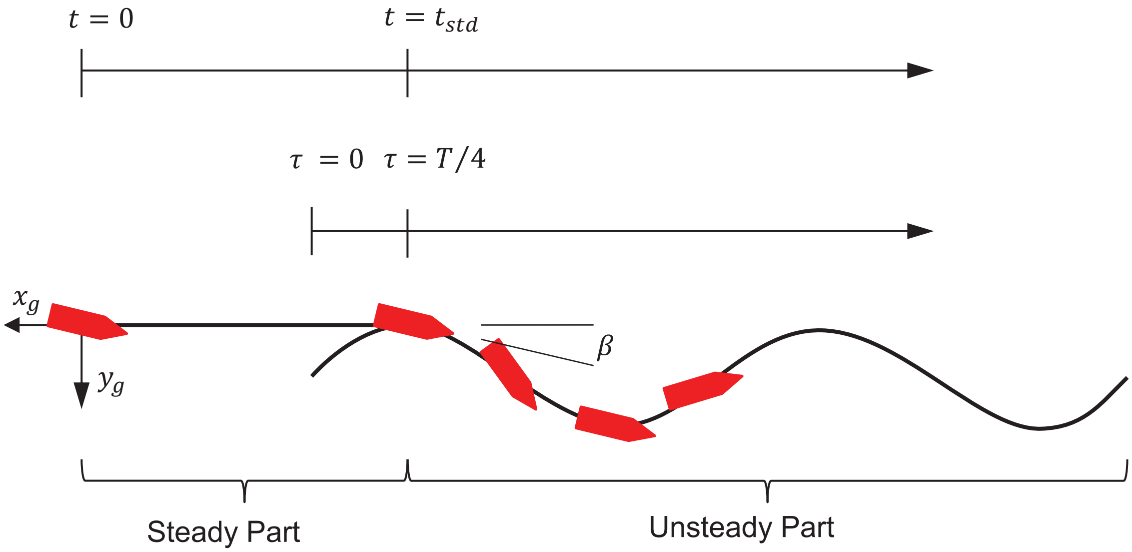

Figure 3.10: Initial Condition in an Unsteady Test

The initial and boundary values for the turbulence parameters as well as the targeted y^+ are presented in Table 3.14. In Table 3.14, the "Turbulence L" within the domain, which is the length scale of the turbulence, is a function of the projected ship width and, in turn, changes with the drift angle. This length scale is only an approximate and, in turn, it is not updated with changes in drift angle. This approximation is made in order to improve the convergence at the beginning of simulation. When solution proceeds in time, the actual turbulent structures formed by ship hull, will develop to be independent of the initial value. The inlet boundary turbulence parameters, however, will influence the solution and thus require a reasonable intial approximation. In this work, it is assumed that the inlet flow is calm with large but not intensive turbulent structures.

No-slip wall is assumed for the model hull where the free-slip condition is implemented on the deck. Domain boundaries form a hexahedron where, in steady drift tests, the lateral boundaries are assumed free-slip walls, velocity inlet boundary condition is chosen for the inlet to the domain, and the pressure outlet boundary condition is applied to the outlet boundary. For the unsteady tests, due to the application of moving mesh method through STAR-CCM+ DFBI model, all side boundaries of the domain are assumed to be velocity inlets.

Wave damping is activated together with an aggressive mesh coarsening toward the boundaries in order to effectively eliminate the waves before they reach the boundaries. Wave damping is applied to a distance of 13 m from pressure outlet boundary in steady tests. It is additionally applied to the same distance from the side boundaries in unsteady tests.

Table 3.14:Turbulence Parameters for the Domain and the Open Boundaries

Steady Drift Initial Condition	I =	0.05	[-]
	k =	0.01153186	$(m/s)^2$
	U =	1.7536	m/s
	U scale =	0.10738648	m/s
	y^+ =	50	[-]
	Y_P =	0.00085008	m
	Cell size =	0.00170016	m
	Drift Angle =	0	[°]
	Ship Length (L_{bp}) =	4	[m]
	Projected Ship Width =	0.5382	m
	Turbulence L =	0.0769	m
Steady Drift Inlet and outlet Turbulence	I =	0.01	[-]
	k =	0.00046127	$(m/s)^2$
	U =	1.7536	m/s
	U scale =	0.0214773	m/s
	Tank Width =	21.36	m
	Turbulence L =	3.0514	m

3.10 MOTION

In order to make the developed computational domain, plots, and scenes applicable to both static and dynamic tests, CPMC model within the STAR-CCM+ is activated for both steady and unsteady tests; i.e. contrary to the technique implemented in the CD-adapco training course [14], the water is assumed stationary and the model and mesh are made to travel with the moving mesh technique. Although this technique slightly increases the computation time for the static tests, it ensures appropriate settings for the time consuming dynamic tests and eliminates the time required for setting up scenes and plots for the dynamic tests. The CPMC equations of motions are defined though Field Functions and are identical to the PMM equations presented in the model test report [1].

Heading:

$$\psi = \psi_1 + \beta = -\tan^{-1}(a\cos(\omega_{mo}\tau)) + \beta \tag{3.2}$$

Yaw rate:

$$r_{PMM} = a\omega_{mo}\sin(\omega_{mo}\tau)\frac{1}{1 + (a\cos(\omega_{mo}\tau))^2} \tag{3.3}$$

Yaw Acceleration:

$$\dot{r}_{PMM} = a{\omega_{mo}}^2 \cos(\omega_{mo}\tau) \left[\frac{1 + a^2(1 + \sin^2(\omega_{mo}\tau))}{(1 + (a\cos(\omega_{mo}\tau))^2)^2} \right] \tag{3.4}$$

Transverse Translation:

$$\eta_{PMM} = -2S_{mm}(-1 + \sin(\omega_{mo}\tau)) \tag{3.5}$$

Transverse Velocity:

$$v_{PMM} = -2\omega_{mo}S_{mm}\cos(\omega_{mo}\tau) \tag{3.6}$$

Transverse Acceleration:

$$\dot{v}_{PMM} = 2\omega_{mo}^2 S_{mm}\sin(\omega_{mo}\tau) \tag{3.7}$$

Longitudinal translation:

$$\xi_{PMM} = U_c\tau \tag{3.8}$$

Longitudinal velocity:

$$u_{PMM} = U_c \tag{3.9}$$

Longitudinal Acceleration:

$$\dot{u}_{PMM} = 0 \tag{3.0}$$

As described in Section 3.1, longitudinal and rotational motion equations had been multiplied by -1 before they were used within the CPMC model of the STAR-CCM+. In the above equations $a = Y_{mm}/R$ and $\omega_{mo} = (2\pi N_{PMM})/60$, with $R = 0.5$ being a distance related to the measurement equipment.

3.11 SOLUTION

While the steady drift cases could theoretically be solved using the steady RANS equations, the VOF technique in STAR-CCM+ is far more robust when solving the unsteady equations for this type of problem. As a result, the steady drift tests have been solved through simulations in time, where the time step, iterative convergence, and overall simulation time have been selected to rapidly achieve a converged steady solution. A minimum simulation time, permitting the inlet flow travel a distance of 4.0 L_{bp}, is required for the inlet flow characteristics to populate within the domain to a distance of about 1.0 L_{bp} downstream of A_p (note that this distance is equal to 2.0 λ, with λ being the ship-generated wave length).

In addition to the considerations above, the steady simulation time was selected to be long enough to allow the results of interest to converge to an unchanging value. As in the model tests, the primary results are the forces and moment in the horizontal plane: the longitudinal force X aligned with the ship centreline, the transverse force Y perpendicular to it, and the yaw moment N about amidships and centreline. Considering the above, the selected simulation time is 30 s; equivalent to the time required for the inlet flow to travel 13.15 L_{bp}.

Since error and uncertainty estimates have been taken from the cases in which the mesh refinement study has been undertaken, these simulations were continued further in time in order to achieve a higher certainty that it is only the random oscillation which is left in variables of interest. A simulation time of 40 s was therefore used for the mesh refinement study; this allows inlet flow to travel a distance of 17.55 L_{bp}.

The unsteady tests were started with an initial steady run until the solution converged. After this steady period, the unsteady run starts and continues for 1.5 T, with T being the period of the oscillatory motion. Details of the run time for the unsteady tests are presented in Table 3.15.

Table 3.15: Unsteady Simulation Time

Steady Part		
Inlet Flow Entering the Domain	[% of L_{bp}]	1315%
Simulation Time	[s]	30.01

Unsteady Part

N-PMM	T	Simulation Time	
[rpm]	[s]	[s]	%T
7	8.57	14	163%
9	6.67	11	165%

Table 3.16: Time Step Size in Steady Drift Tests

Time Step Selection		
Coarse Mesh		
Minimum Surface Size	[% of base size]	50%
Minimum Surface Size	[m]	0.00525
CFL	[-]	17
Time Step	[s]	0.051
Medium Mesh		
Minimum Surface Size	[% of base size]	50%
Minimum Surface Size	[m]	0.003712
CFL	[-]	17
Time Step	[s]	0.036
Fine Mesh		
Minimum Surface Size	[% of base size]	50%
Minimum Surface Size	[m]	0.002625
CFL	[-]	17
Time Step	[s]	0.025

In steady drift tests, the simulation time, the number of iterations, and the temporal order of accuracy were manually given to the solver while in unsteady tests Field-Function and Java files were used in order to differentiate between the steady and unsteady part of the simulation. In steady solutions a first-order temporal discretization was used with five iterations per time step. In unsteady solutions a second-order temporal discretization was used with ten iterations per time step. The time step size used for steady drift tests is presented in Table 3.16. This achieves a Courant–Friedrichs–Lewy (CFL) number of 17, based on the carriage speed and the number assigned to the Minimum Surface Size in the Surface Remesher of the STAR-CCM+ software, which was considered sufficient to yield a converging solution. The same CFL number was maintained through the mesh refinement study. The time step sizes presented in Table 3.16 were used after the first 15 seconds of simulations. Slightly larger time step sizes were used at the beginning of the steady simulations in order to reduce the computational effort.

The same strategy as in Table 3.16 was followed in the steady part of the unsteady tests; this is described in Table 3.17. Following Samamoto's work [17], 384 time steps per motion period were used within the unsteady part of the simulation in unsteady tests. This selection is consistent with the objective of resolving flow phenomena having time scales that are relatively similar to the time scale of the PMM motions. In unsteady tests, the unsteady part of the run is started at $\tau = T/4$, with $\tau = t - t_{std} + T/4$; see Figure 3.10.

Table 3.17: Time Step Size in Steady Run Part of the Unsteady Tests

Time Step Selection		
Coarse		
Minimum Surface Size	[% of base size]	50%
Minimum Surface Size	[m]	0.007425
CFL	[-]	17
Time Step	[s]	0.072
Medium		
Minimum Surface Size	[% of base size]	50%
Minimum Surface Size	[m]	0.00525
CFL	[-]	17
Time Step	[s]	0.051
Fine		
Minimum Surface Size	[% of base size]	50%
Minimum Surface Size	[m]	0.003712
CFL	[-]	17
Time Step	[s]	0.036

3.11.1 Time Step Size Refinement

From the numerical view point, a solution can be deemed sufficiently accurate when it is grid and time step size independent. The number of the time steps used in the unsteady part of the unsteady yaw and drift test with the drift angle of 10° was changed from 384 time steps per motion period to 768 time steps. Figure 3.11 depicts the influence of this change in the time step size on the accuracy of the simulation. Some improvement can be observed in the computed data, at the cost of the simulation time increasing from 6 hours to 12 hours. Further refinement in time seems to be needed in order to achieve a solution which is completely independent of the time step size. This, however, leads to very demanding simulations which are out of the reach within a reasonable time by a 12-core machine.

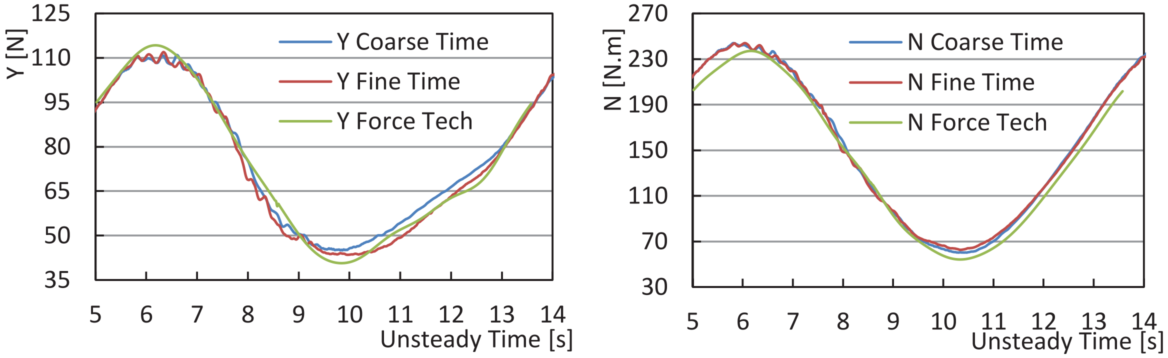

Figure 3.11: Time Step Size Effect on the Computed Y and N in Unsteady Yaw and Drift Test with the Drift Angle of 10°

3.11.2 Simulation Cyclic Repeatability

It is important for a CPMC manoeuver test to be repeatable, at least within an acceptable range of accuracy. In Figure 3.12 the computed Y and N in the last two motion cycle of the CPMC manoeuver for the unsteady yaw and drift test with the drift angle of 10° are compared. For the comparison purpose, in Figure 3.12, the second motion cycle is shifted in time in order to overlap the first motion cycle. With regard to the temporal and spatial accuracy of the solution, the simulation can be considered repeatable.

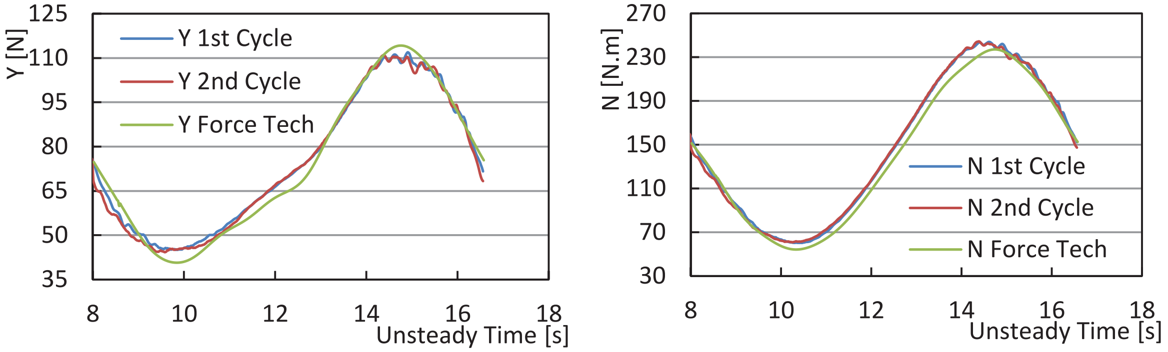

Figure 3.12: Cyclic Repeatability of the Computed Y and N in Unsteady Yaw and Drift Test with the Drift Angle of 10°

3.12 POST-PROCESSING

Post processing of data consists of three subcategories; pre-setup for STAR-CCM+, post processing of the raw data directly extracted from STAR-CCM+ in order to compare them with the raw measured data, and post processing of the computed forces and moments for calculating the dimensionless manoeuvring coefficients as well as the error and uncertainty estimate.

3.12.1 Pre-Setup for STAR-CCM+

Most pre-setups for STAR-CCM+ are built-in and only an appropriate selection is required regarding the expected results from the solution. There are, however, opportunities to include user-defined modifications to the default pre-setups to improve the way results are presented. For instance, helicity is a built-in function which can be reported within a Scene in STAR-CCM+. The quality of this Scene in terms of the information it can provide, however, can be highly improved if the built-in helicity function is first made dimensionless and then presented on the iso-surfaces of Q-Criterion. This provides a visualization of the vortex structures and their direction of rotation. The normalized helicity density is defined as:

$$H_n = \frac{\vec{u}_g \cdot \vec{\omega}_g}{|\vec{u}_g||\vec{\omega}_g|} \tag{3.11}$$

where, $\vec{u}_g$ and $\vec{\omega}_g$ are velocity and vorticity vectors in global coordinates, respectively. Following Sakomoto [17], the second invariant of the rate of deformation tensor, Q-Criterion, is used to identify the vortical structures and is defined as:

$$Q = \frac{1}{2}\left(\left|\vec{\mathbf{\Omega}}\right|^2 - \left|\vec{\mathbf{S}}\right|^2\right) \tag{3.12}$$

where, the rate of strain, $\vec{\mathbf{S}}$, and vorticity, $\vec{\mathbf{\Omega}}$, tensors are defined as:

$$\vec{\mathbf{S}} = \frac{1}{2}\left(\nabla\vec{u}_g + \left[\nabla\vec{u}_g\right]^T\right) \tag{3.13}$$

$$\vec{\mathbf{\Omega}} = \frac{1}{2}\left(\nabla\vec{u}_g - \left[\nabla\vec{u}_g\right]^T\right) \tag{3.14}$$

If Q is positive, the Euclidean norm of vorticity tensor dominates the rate of strain which dictates the rotation of flow. The H_n represents the directional cosine between the vorticity vector and velocity vector with $-1 \le H_n \le 1$. Based on the global coordinate system defined in Section 3.1, the positive sign of H_n corresponds to the vortices rotating counter-clockwise in the global coordinate system.

Visualizations were also prepared to show the pressure disturbance on the hull. This pressure disturbance is the difference between the pressure field of the vessel in motion and the pressure filed of the vessel in stationary condition in calm water. Preliminary simulations showed that the contribution of the hull viscous stresses to the manoeuvring forces and moments is much smaller than the effect of the asymmetry in pressure disturbance, thus the asymmetry in pressure disturbance gives a reasonable indication of how the manoeuvering forces and moments are developed. The pressure disturbance is defined as:

$$\delta p = p + \rho_w g z_g \tag{3.15}$$

where, p is the pressure predicted by simulation, ρ_w is the density of water, $g = 9.806\ \mathrm{m}/s$ is the gravitational acceleration, and z_g is the vertical position in the global coordinate system. The pressure p is such that in calm water, $p = 0$ and $z_g = 0$ at the free surface.

3.12.2 Post Processing of the Raw STAR-CCM+ Outputs

In order to compare the computed and measured data, the comparison error, $E[\%D]$, is defined as:

$$E[\%D] = \frac{(D - C)}{D} \times 100 \tag{3.16}$$

where C denotes computed data and D denotes measured data.

For the steady drift tests, the computed and measured forces and moments at every drift angle were compared with the measured data in Microsoft Excel and their $E[\%D]$ is calculated.

In order to be able to compare the computed data with those measured in the model tests [1, 23], dimensionless forces and moments are defined in the same manner as in the references:

$$X' = \frac{X}{0.5\rho\left|\vec{u}_{s_s}\right|^2 A_0}\ ,\quad Y' = \frac{Y}{0.5\rho\left|\vec{u}_{s_s}\right|^2 A_0}\ ,\quad Z' = \frac{Z}{0.5\rho\left|\vec{u}_{s_s}\right|^2 A_0 L_{bp}} \tag{3.17}$$

where, $A_0 = L_{bp} T_m$ is the lateral underwater area.

As the magnitude of the vessel velocity, $\left|\vec{u}_{s_s}\right|$, varies in time for the unsteady tests, dimensionless variables were developed prior to other post-processing.

3.12.3 Steady Convergence

It is generally infeasible to converge steady simulations to machine precision, and as a result it is necessary to use partially converged results. STXM experience with simple resistance simulations is that after initial transient behaviour, the resistance typically follows a pattern like that of a decaying sinusoid. However in the steady drift simulations, the convergence of the manoeuvring forces and moment was more erratic; it typically included apparently random higher-frequency oscillations (noise) superimposed on a low-frequency pattern. The low-frequency pattern sometimes resembled a decaying sinusoid, but other times tended more or less monotonically towards a converged value, and sometimes included step changes.

This type of behaviour could be indicative of a steady solution which is not fully converged, or a fundamentally unsteady flow pattern which may or may not be well-resolved by the time step used (such that the high-frequency oscillations truly are numerical noise). The simulations were run until it was clear that the continuing oscillations in the manoeuvring forces and moment were a small percentage of the mean value.

While very small compared to the mean value, the noise was found to be near the same order of magnitude as the difference in the results obtained on different mesh sizes in the mesh sensitivity study. As the spatial discretization error calculation is based on the differences between these results, the noise made the spatial discretization error calculation more difficult. A reasonable and objective means of selecting a converged steady solution, including an assessment of the convergence uncertainty, was therefore sought. The following technique using a weighted average was used (using X as an example):

$$\bar{X} = \frac{\sum_{k=1}^{n} w_k X_k}{\sum_{k=1}^{n} w_k} \tag{3.18}$$

$$w_k = \left(\frac{1 - \cos\left(\frac{\pi k}{n}\right)}{2} \right)^4 \tag{3.19}$$

where x is a generic result, and k is an integer from 1 to n. The case where $k = 1$ corresponds to the first time step for which both of the following are satisfied, before which known causes of transient behaviour are ongoing:

a) the flow which started at the inlet, which carries the inlet turbulence parameters, has convected downstream past the transom; and

b) the waves generated at the forward perpendicular (as approximated by the transverse waves in a steady Kelvin wake pattern) at the start of the simulation have been overtaken by the transom.

The successively larger integer values of k correspond to successive time steps until the final time step in the simulation, where $k = n$. This weighting function is arbitrary; however it is helpful because it places very similar large weights on the final few iterations, and essentially ignores the first several iterations. The details of the shape of the weighting function become irrelevant as the simulation approaches convergence.

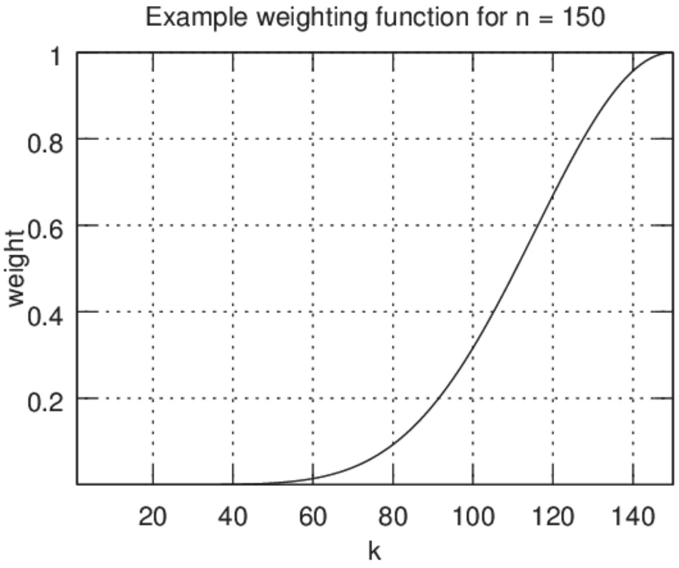

Figure 3.13: Weighting Function for Steady Convergence Calculations

Using the same weighting function, the weighted standard deviation of a result was computed as:

$$\sigma = \sqrt{\frac{\sum_{k=1}^{n} w_k (x_k - \bar{x})^2}{\sum_{k=1}^{n} w_k}} \tag{3.20}$$

Similarly, a weighted standard deviation associated with the estimate of the mean value was calculated using the following equation, which is adapted from the central limit theorem:

$$\bar{\sigma} = \frac{\sigma}{\sqrt{\sum_{k=1}^{n} w_k}} \tag{3.21}$$

Finally, the converged value, including convergence uncertainty, was calculated as $\bar{X} \pm 4\bar{\sigma}$. In all cases, this was checked against a visual estimate based on a plot of the result against time.

An example convergence plot is shown in Figure 3.14. It shows the evolution of the values above, as they would have been computed had the simulation been stopped at some earlier time, t. Indicators of reasonable convergence include the relatively constant values for the mean (black curve) and the uncertainty in the mean (green curves), as well as the small uncertainty in the mean at the end of the simulation (close spacing of the green curves).

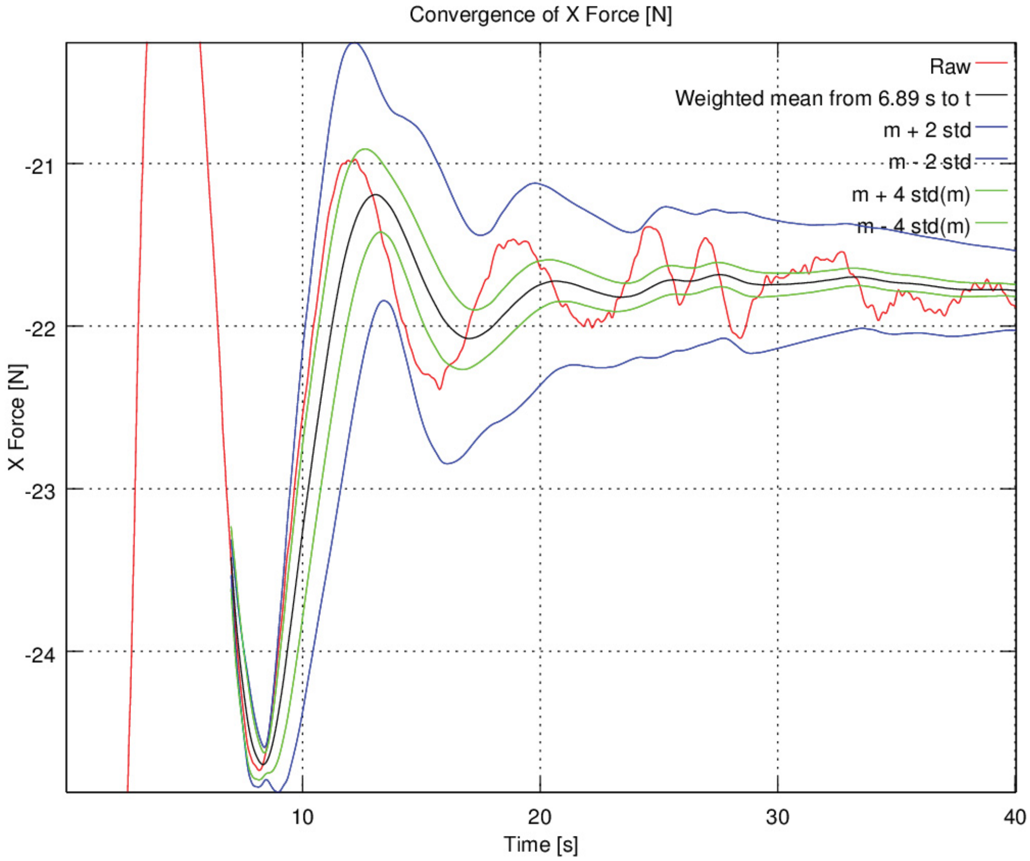

Figure 3.14: Example Determination of Steady Converged Value and Uncertainty

3.12.4 Harmonic Analysis

In a manoeuvring assessment of a ship, the results of unsteady PMM tests would normally be used to determine the manoeuvring derivatives. These are coefficients of Taylor series expansions of the manoeuvring forces and moments with respect to the velocities and accelerations of the vessel. The series expansions would then typically form the basis of a mathematical manoeuvring model, which integrates the manoeuvring equations to predict IMO or other manoeuvres for comparison against manoeuvring criteria.

In theory, it would therefore be most relevant to the designer if the basis for comparison of CFD to experimental PMM results were the salient results of the manoeuvres predicted by mathematical models derived from the CFD or experimental PMM results. However for this project, such an approach would be too specific to the actual manoeuvres simulated, and would require separate estimation of the influence of a rudder. In addition, such an approach would not help to determine whether a particular simulation in the ensemble is more or less accurate than the rest.

On the other hand, direct comparison of the PMM time-histories against the experimental time-histories is not ideal, because it would need to be robust with respect to both experimental and numerical noise, and because a substantial amount of the information contained in the time-series is essentially discarded through the process of determining manoeuvring derivatives.

As a compromise between the above two extremes, harmonic analysis of both the CFD and the experimental dynamic test results has been completed so that the harmonic amplitudes can be directly compared. This is considered to retain the relevant information from the time-histories, as some techniques for computing manoeuvring derivatives use harmonic analysis as a first step, and they can provide one-to-one correspondence to some manoeuvring derivatives. As mathematical manoeuvring models typically do not include terms of order higher than three (except derivatives of X' with respect to u), third-order harmonic analysis was used.

To complete the harmonic analysis, a least-squares fit of the following equation to the experimental or CFD time-history was performed for each result of each test or simulation; it determined the coefficients C_0, $C_{k,c}$, and $C_{k,s}$.

$$\mathcal{X}'(\tau) = C_0 + \sum_{k=1}^{3} \left(C_{k,c} \cos k\omega_{mo}\tau + C_{k,s} \sin k\omega_{mo}\tau \right) \tag{3.22}$$

where $\mathcal{X}'(\tau)$ is the Fourier series representation of the raw time series $X'(\tau)$, $\omega_{mo} = 2\pi/T$ is the PMM frequency [rad/s] and τ is time. Similar equations are used for Y' and N'.

4 RESULTS

The following sections present the CFD results for each type of PMM test: drift, unsteady yaw and drift, unsteady pure yaw, and unsteady pure sway. Each section includes comparison against the respective model test results. The sections also include the results of two mesh refinement studies and of four additional simulations without bilge keels.

Outputs from STAR-CCM+ which are not discussed within the text are referenced in Appendix A to Appendix D; Appendix A includes extensive data including animations, and is provided in electronic format.

An error in the initial setup of the unsteady simulations was found late in the project. This resulted in incorrect draft and trim, and is discussed in detail in Section 5.1.

4.1 GENERAL COMMENTS

Every set of CPMC tests was initially performed with a coarser mesh in order to remove probable problems in scenes setup and to check the mesh and solution in a qualitative manner. Figure 4.1 presents a scene for y^+, which is used to ensure an appropriate near-wall treatment. This figure, for instance, shows that the range of y^+ values on the wet portion of the hull are reasonable for the wall-function approach used, so provides verification of the boundary layer modelling for the steady drift test with the drift angle of 0°. The waterline on the ship hull is presented in Figure 4.2 for the steady drift test with the drift angle of 10°. This plot indicates the positions where the water surface refinement blocks should be placed near the hull.

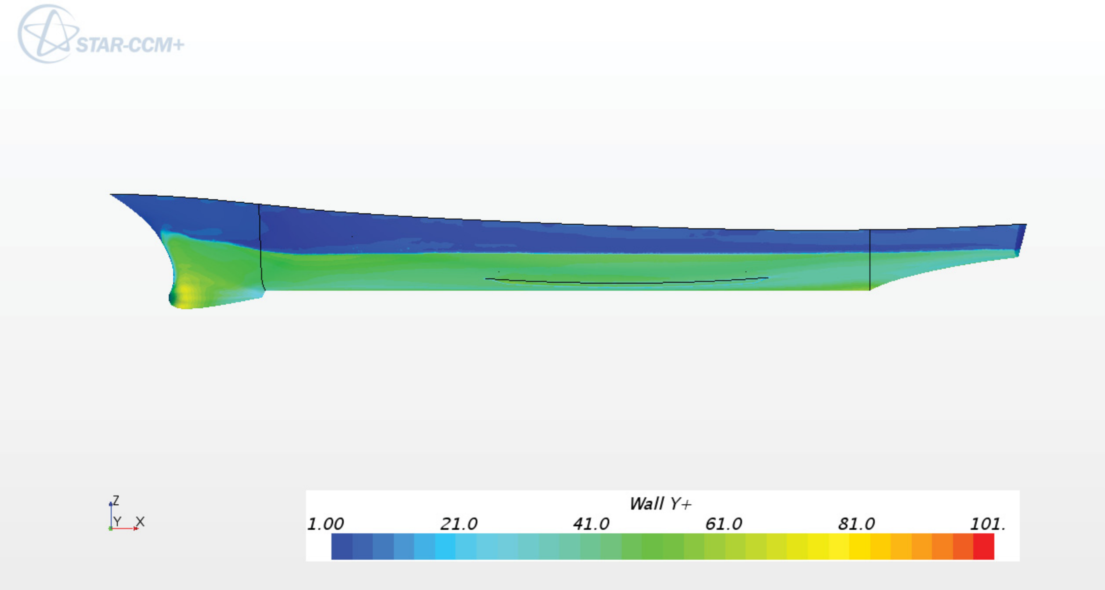

Figure 4.1: Ship Hull Colored with y^+ in Medium Mesh, with a Steady Drift Angle of 0°

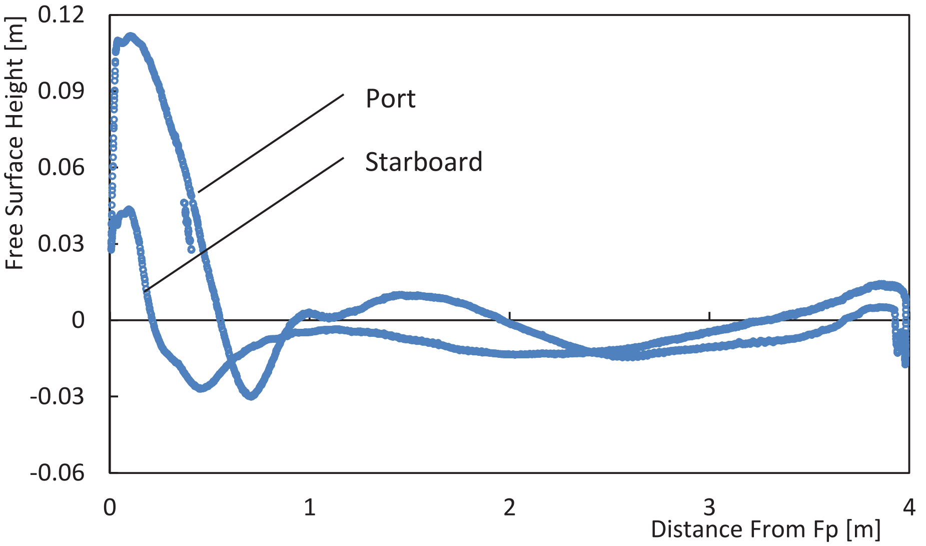

Figure 4.2: Water Surface on Ship Hull, 10° Drift, Medium Mesh

4.2 STEADY DRIFT

The first step in performing steady drift tests was a mesh refinement study at the drift angle of 10 degrees. This allowed the appropriate mesh to be identified prior to completing the remainder of the steady drift simulation matrix.

4.2.1 Discussion of Raw CFD Results and Mesh Refinement

Although in accordance with the literature [4, 6, 17] all static drift CPMC test have been assumed to be steady, the simulations indicate local unsteady flow structures such as a breaking bow wave; Figure 4.3-a. Figure 4.3-b shows local mesh refinement included to better capture the breaking bow wave. An even finer mesh and a shorter time step would be required to fully resolve this flow structure; such high accuracy for local flow structures is not considered to be important to the overall accuracy of the net forces and moments on the hull.

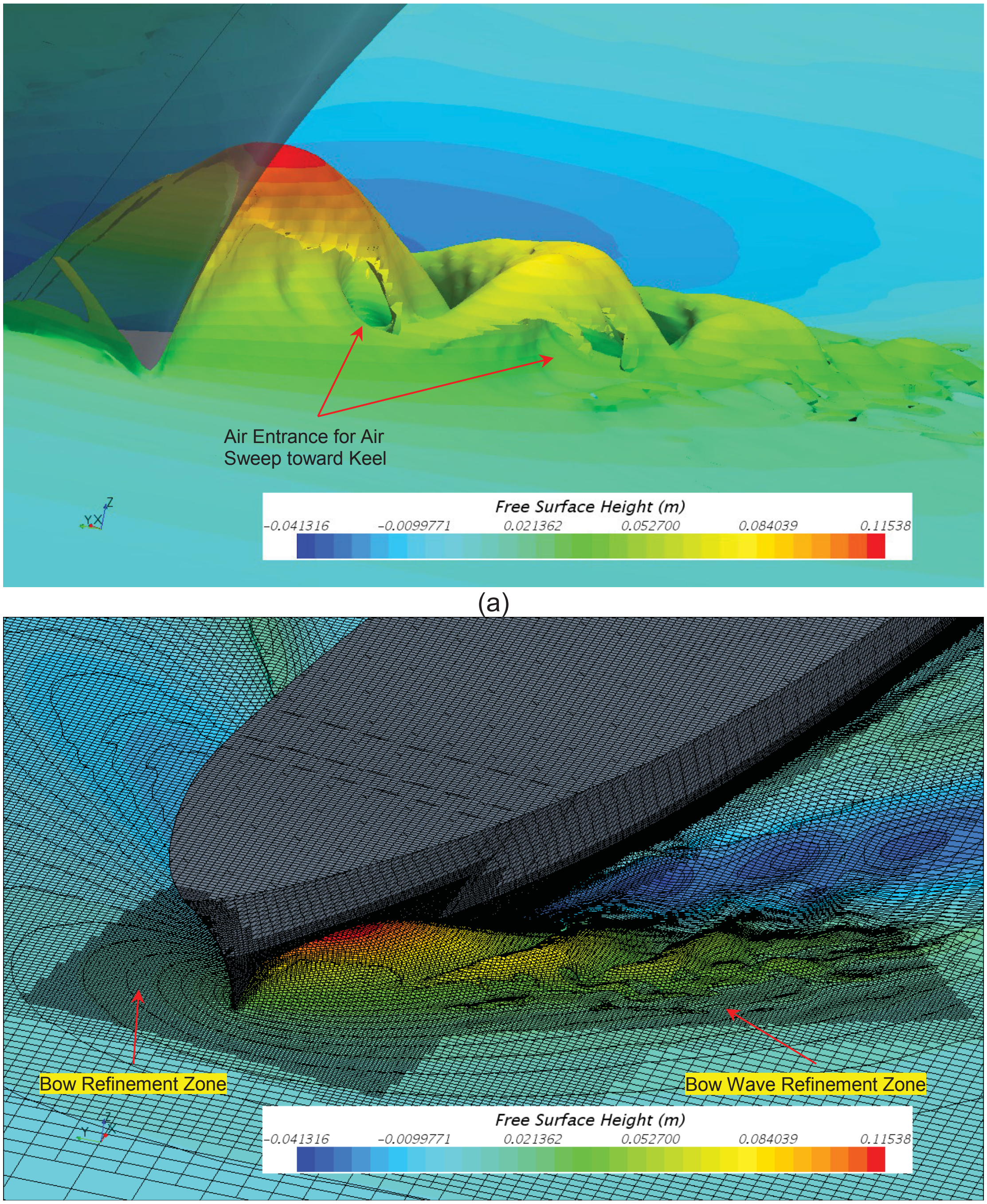

(a)

(b)

Figure 4.3: Bow Wave, 10° Drift, Fine Mesh

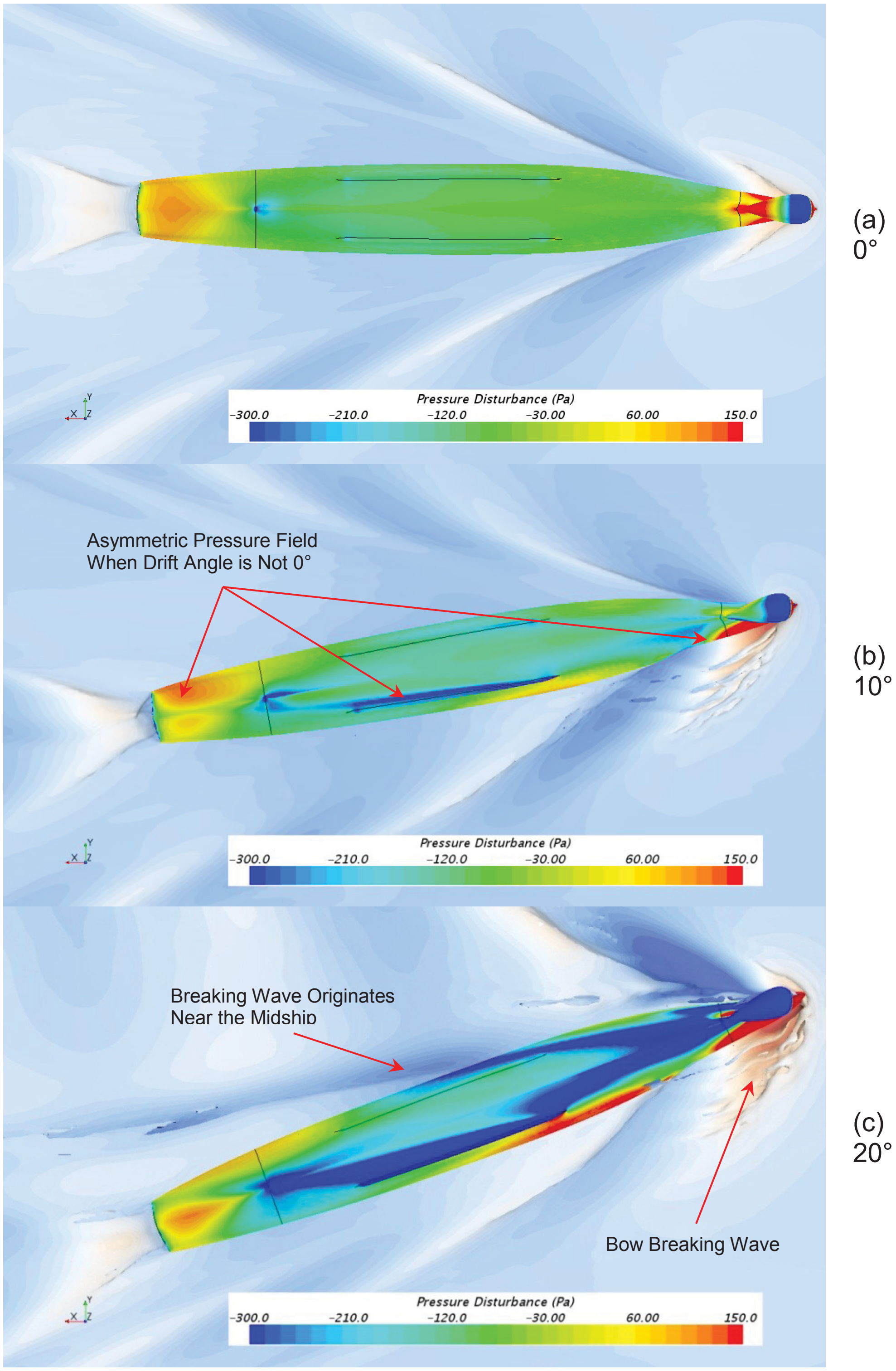

Asymmetric Pressure Field When Drift Angle is Not 0°

Breaking Wave Originates Near the Midship

Bow Breaking Wave

Figure 4.4: Pressure Disturbance and Surface Waves, Medium Mesh

Table 4.1: Force Along x_s in Steady Drift Test's Mesh Refinement Study

Drift Angle	X F.T.		X INSEAN		X CFD	
[deg]	[-]	[N]	[-]	[N]	[-]	[N]
10	-0.019465	-20.77	-0.019147	-20.43		
Coarse Mesh					-0.020412	-21.782
Medium Mesh					-0.019644	-20.963
Fine Mesh					-0.019596	-20.912

E[%D]

Coarse Mesh		Medium Mesh		Fine Mesh	
X F.T.	X INSEAN	X F.T.	X INSEAN	X F.T.	X INSEAN
-4.9%	-6.6%	-0.9%	-2.6%	-0.7%	-2.3%

Table 4.2: Force Along y_s in Steady Drift Test's Mesh Refinement Study

Drift Angle	Y F.T.		Y INSEAN		Y CFD	
[deg]	[-]	[N]	[-]	[N]	[-]	[N]
10	0.061699	65.84	0.064103	68.41		
Coarse Mesh					0.059619	63.622
Medium Mesh					0.059937	63.961
Fine Mesh					0.059182	63.155

E[%D]

Coarse Mesh		Medium Mesh		Fine Mesh	
Y F.T.	Y INSEAN	Y F.T.	Y INSEAN	Y F.T.	Y INSEAN
3.4%	7.0%	2.9%	6.5%	4.1%	7.7%

The unsteadiness as well as the nonlinearity in flow structures become stronger with increasing drift angle. This generates noise into the solution which will increase the uncertainty of the computed data. This increase in nonlinearity with an increase in drift angle can be observed, for instance, in Figure 4.4. In Figure 4.4-c an extra breaking wave is noticeable which originates on the starboard side near midships. For these small scale flow structures (small scale normal to their propagation direction), to be appropriately captured, further refinement in time and space is required. As the structures depend on drift angle, the refinement zone would need to be optimized in a case-specific manner. These procedures would increase the accuracy of the solution in capturing the nonlinear effects which are pronounced at high drift angles. In this work, however, such case-specific mesh was not developed since the procedure is very time consuming.

Three meshes, as indicated in Table 3.10, were chosen for the mesh refinement study. The results indicate a significant improvement in computational accuracy in the medium mesh compared with the coarse mesh, while the improvement in accuracy achieved with the fine mesh is not significant compared to the medium mesh; see Table 4.1 to Table 4.4.

Table 4.3: Force Along z_s in Steady Drift Test's Mesh Refinement Study

Drift Angle	Coarse Mesh		Medium Mesh		Fine Mesh	
[deg]	[-]	[N]	[-]	[N]	[-]	[N]
10	-1.7254	-1841.2	-1.7280	-1844	-1.7290	-1845.1

Vessel	$-\nabla$	$-\Delta$	
	[m^3]	[N]	[-]
	-0.1897	-1858	-1.7413

E[%D]

Coarse Mesh	Medium Mesh	Fine Mesh
Δ	Δ	Δ
0.9%	0.8%	0.7%

The iso-surfaces of Q-Criterion ($Q = 30$) colored with dimensionless helicity, as well as the contours of velocity component along x_g is presented in Figure 4.5. The coarse mesh in Figure 4.5-a is very diffusive and loses the trace of the Q=30 iso-surface on the starboard side. The medium and fine meshes are both capable of capturing the larger scale flow structures, while only the fine mesh is able to capture small scale eddies formed due to bow breaking waves on the port side. The insufficiency of the coarse grid resolution in capturing large scale flow structures likely causes the significant difference in $E[\%D]$ of the solutions in coarse and medium mesh in Table 4.1; the difference between the $E[\%D]$ of the medium and fine mesh is not significant.

Table 4.4: Moment Around z_s in Steady Drift Test's Mesh Refinement Study

Drift Angle	N F.T.		N INSEAN		N CFD	
[deg]	[-]	[N.m]	[-]	[N.m]	[-]	[N.m]
10	0.0306	130.63	0.0319	136.32		
Coarse Mesh					0.029370	125.44
Medium Mesh					0.029789	127.23
Fine Mesh					0.029735	127.00

E[%D]

Coarse Mesh		Medium Mesh		Fine Mesh	
N F.T.	N INSEAN	N F.T.	N INSEAN	N F.T.	N INSEAN
4.0%	8.0%	2.6%	6.7%	2.8%	6.8%

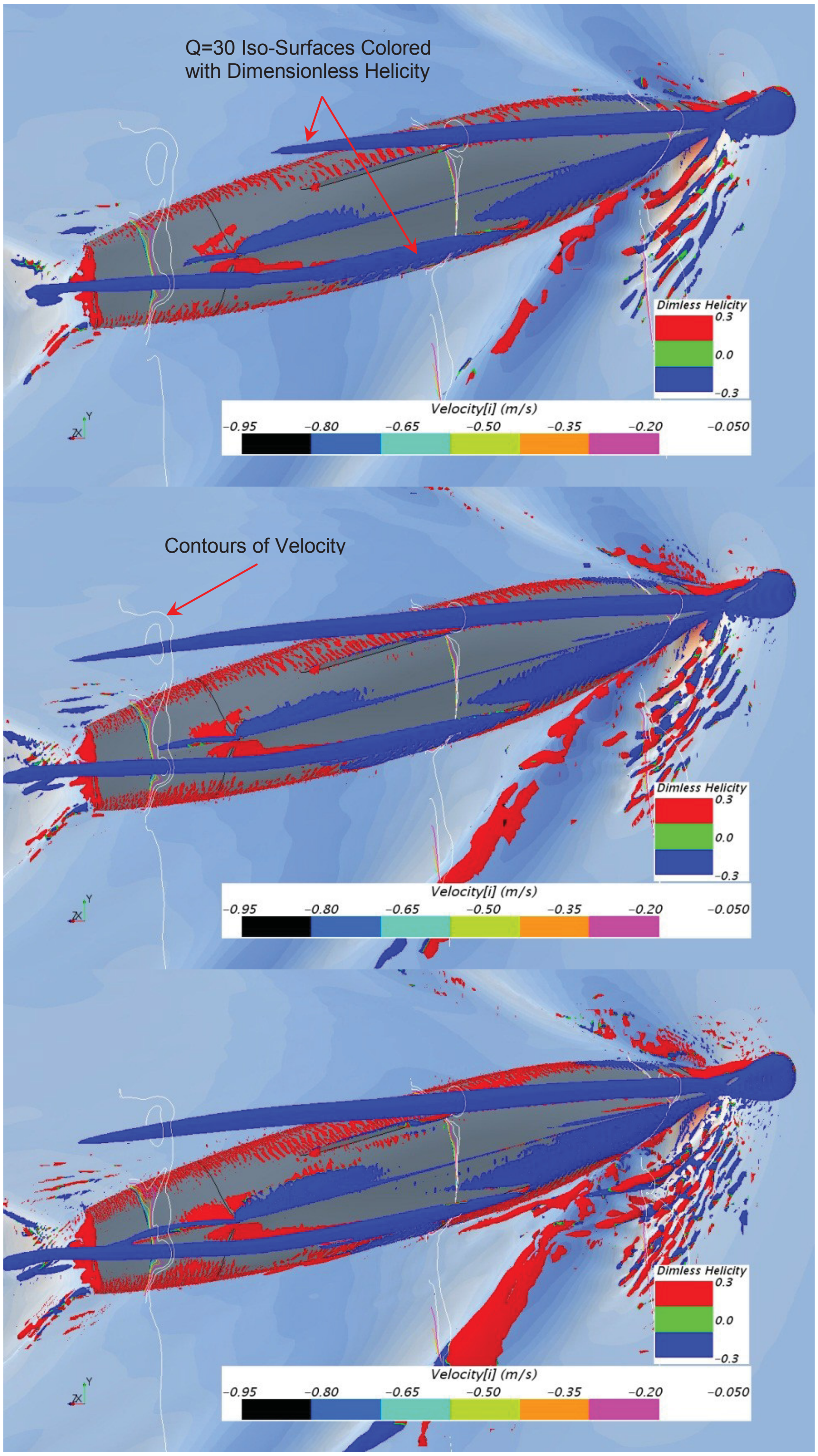

Q=30 Iso-Surfaces Colored with Dimensionless Helicity

Contours of Velocity

(a) Coarse

(b) Medium

(c) Fine

Vortices captured by Q=30 and coloured by helicity; velocity contours at three stations

Figure 4.5: Vortex Structure and Velocity Contours, 10° Drift

The same pattern, similar to what is noticeable in Figure 4.5, can be observed in Figure 4.6. The coarse mesh is very diffusive and loses the vortical structure near the starboard side's bilge keel, which was originated from the bow. This vortical structure builds a local vorticity in an interaction with the bilge keel on the starboard side. A plunging breaking wave can be observed on the top-right side of the images in Figure 4.6 which forms the Q=30 iso-surface near the water surface at the port side of the ship within the images in Figure 4.5 (at an angle of about 20° to the ship centerline). The fine mesh in Figure 4.6 indicates that the vortices generated by this plunging breaking wave can interact with other ship-generated vortical structures, and influence the forces and moments acting on the ship through increasing anisotropy and nonlinearity effects.

The vortex generated at the sonar bulb is prominent in both Figure 4.5 and Figure 4.6. In Figure 4.6, it can be seen that as this counter clockwise-turning bow vortex is swept under the leeward bilge keel. While the overall transverse flow component is to starboard, the transverse flow component on the upper part of this vortex is to port. The sonar bulb vortex thereby causes the transverse component of flow past the tip of the bilge keel to be to port, rather than to starboard. This causes the smaller bilge keel vortex to be shed on the port side of the bilge keel, and to turn in the clockwise direction; both these characteristics are opposite to what would normally be expected without the influence of the large vortex from the sonar bulb. This type of interaction would not be captured by less sophisticated manoeuvring calculation techniques that treat the hull and appendages independently.

The ship generated surface waves are presented in Figure 4.7. In this figure, the predicted maximum and minimum of the water surface elevation change with grid refinement. The minimum water surface elevation in Figure 4.7-c is a very small zone near the port side of the bow. Since the bow breaking wave is not fully resolved, it shows different patterns from the coarse to the fine mesh.

Figure 4.8 presents the waterline on ship hull. The coarse mesh results have a clean waterline while with the medium mesh there is some sign of aeration. Patterns of air pockets captured in water due to the plunging breaking bow wave can be observed in the fine mesh (Figure 4.3-a shows the entrance of air into the water). These air pockets are drawn downwards and aft. A trace of these air pockets can be observed in Figure 4.2 about 0.4 m aft of the FP between 0.03 m to 0.06 m above the calm water level. Some aeration seems to appear aft of midships, the trace of which can be observed in Figure 4.5-c as a red spot slightly ahead of the midship on the water surface, near the port side of the hull. A small scale plunging breaker, which is unsteady, seems to extend downstream before its energy dissipates.

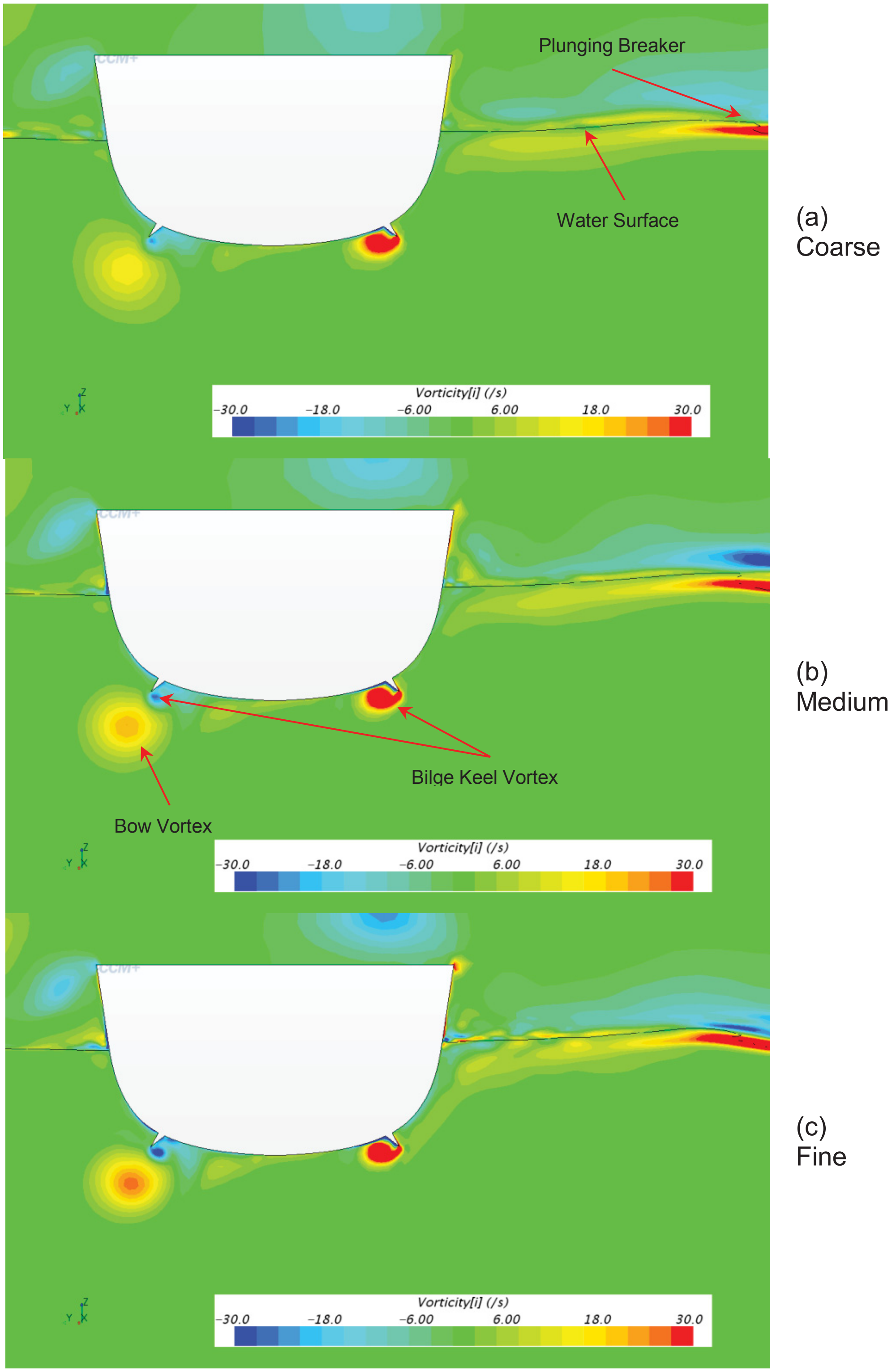

(a)
Coarse

(b)
Medium

(c)
Fine

Figure 4.6: Vorticity Component in x_g Direction Amidships, 10° Drift

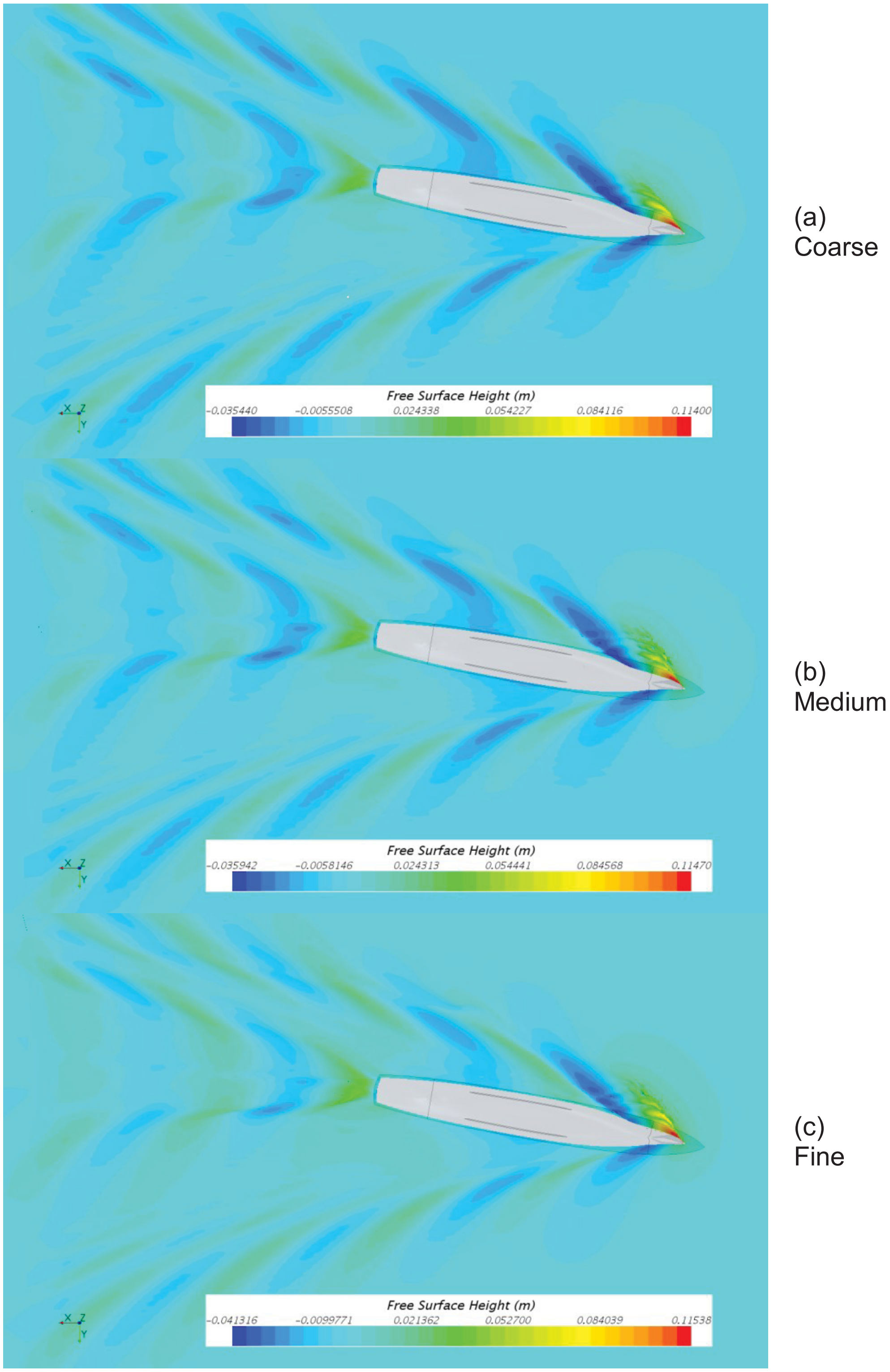

(a)
Coarse

(b)
Medium

(c)
Fine

Figure 4.7: Ship Generated Surface Waves, 10° Drift

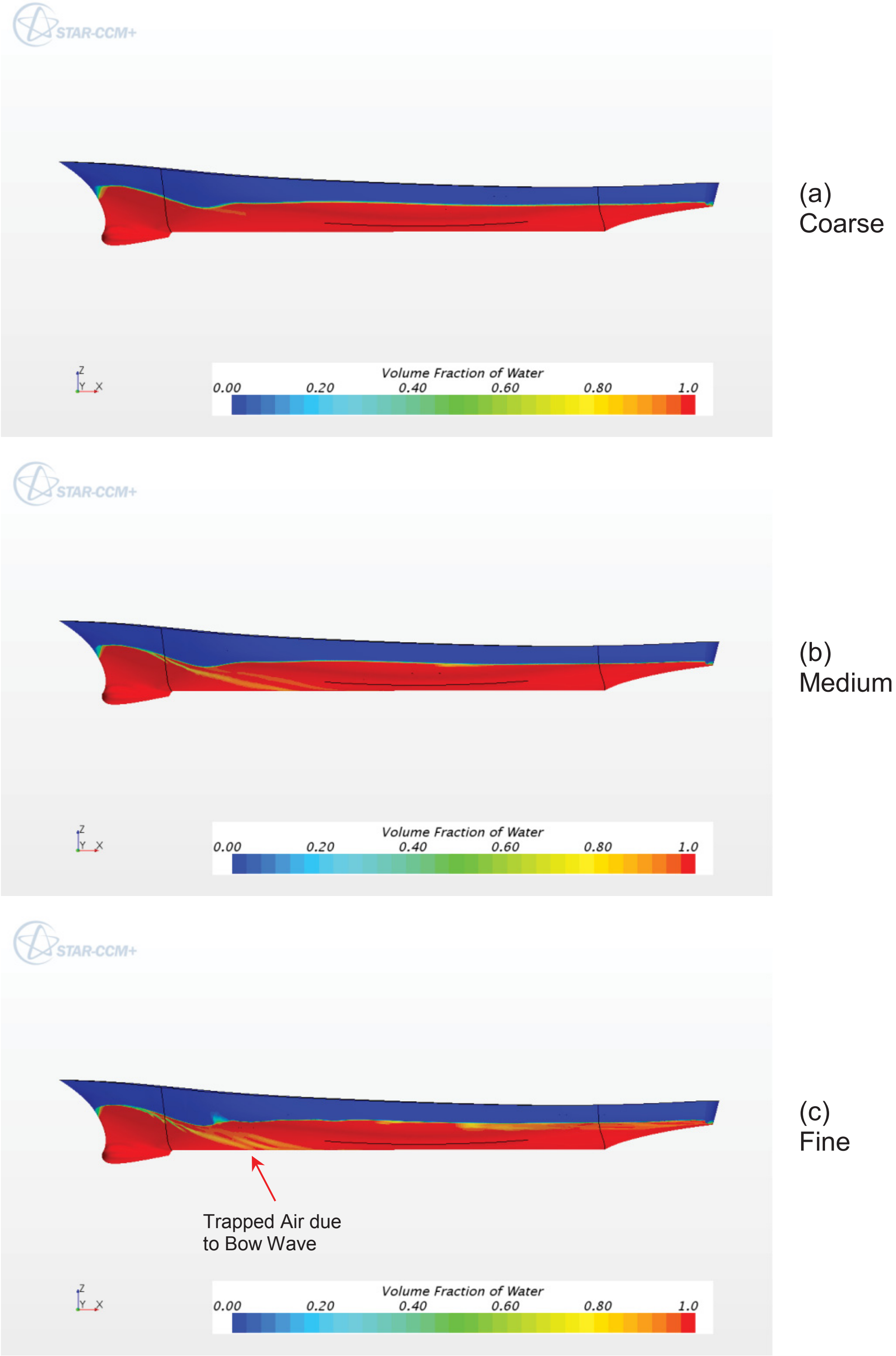

Figure 4.8: Waterline on Ship Hull, 10° Drift

Since the medium mesh is significantly smaller in size than the fine mesh and it is capable of resolving the variables of interest within the acceptable range of accuracy, it was selected to be used in the rest of the steady drift tests. The fine mesh significantly increases the required time for computations by reducing the time step size as well as incorporating more cells within the domain.

4.2.2 Spatial Discretization Error

The spatial discretization error has been computed using the mesh refinement study results and the methodology presented in the Journal of Fluids Engineering guidelines, by Celik *et al.* [3]. The error calculation is reasonably straightforward, and yields a relative error denoted GCI_{fine}^{21}.

However as alluded to in Section 3.12.3, it was not practical to run the steady simulations for long enough to achieve an iteration convergence error in the forces that was two or three orders of magnitude smaller than the spatial discretization error. The simulation results and the iteration uncertainty, calculated as described in Section 3.12.3, are shown in Table 4.5.

The iteration error has therefore been included in the spatial discretization error calculation by repeating the calculation presented by Celik *et al.* [3] using each combination of possible input values. That is, each combination of maximum or minimum result predicted for each of the three meshes, such that a total of eight sets of input values were used for each force or moment. From the ensemble of results, the maximum and minimum spatial discretization error was determined. Table 4.5 shows the minimum, expected (a simple calculation based on the central values of the forces), and maximum predicted spatial discretization error.

Table 4.5: Steady Drift Spatial Discretization Error Calculation

	X’	**Y’**	**N’**
Coarse mesh	-0.020411 ± 0.000034	0.059620 ± 0.00011	0.029370 ± 0.000026
Medium mesh	-0.019644 ± 0.000026	0.059937 ± 0.000083	0.029790 ± 0.000026
Fine mesh	-0.019596 ± 0.000028	0.059182 ± 0.000074	0.029736 ± 0.000029
Apparent order†	6.11, 8.83, 15.8	1.51, 3.29, 6.91	0.80, 2.67, 6.27
$\boldsymbol{GCI_{\text{fine}}^{21}}$ †	0.0004%, 0.027%, 0.14%	0.26%, 1.0%, 3.0%	0.70%, 1.1%, 1.6%

† *Minimum, expected, and maximum values are shown.*

The results show that due to the convergence error, it is difficult to accurately predict the spatial discretization error. However it can also be seen that the most unfavourable estimate of the spatial discretization error is still quite good: just 0.14% for X', 3.0% for Y', and 1.6% for N'.

For Y' and N', there is reasonable agreement between the middle value of the apparent order and the theoretical order of two for the method used. This indicates that the mesh may be sufficiently refined to be in the asymptotically converging region where this type of error estimation is most accurate. However the apparent order for X' is more substantially different from 2, so a more refined mesh may be required to accurately predict the (already very small) spatial discretization error for X'.

4.2.3 Comparison to Model Tests

The computed dimensionless forces and moment are compared with both FORCE Technology [1] and INSEAN [24] measurements in Figure 4.9 to Figure 4.11. In these figures, due to the symmetry of the model, the measured data at negative drift angles are mirrored in order to perform a better comparison with the computations. The R^2, in these figures, is the coefficient of determination which indicates how well data points fit a statistical model. In Figure 4.9, the computed forces are very close to the measurements by INSEAN [24] except at the drift angle of 16°. At this drift angle, there is a significant discrepancy not only between the computed and measured data, but also between the FORCE Technology [1] and INSEAN [24] measurements. A case specific mesh and solution strategy seems to be necessary at this drift angle in order to make sure of a grid and time independent solution. Developing a case specific strategy, however, is out of the scope of this work and can be addressed within the future investigations. FORCE Technology measurements [1] seem to over predict the X at small drift angles up to the drift angle of 6°.

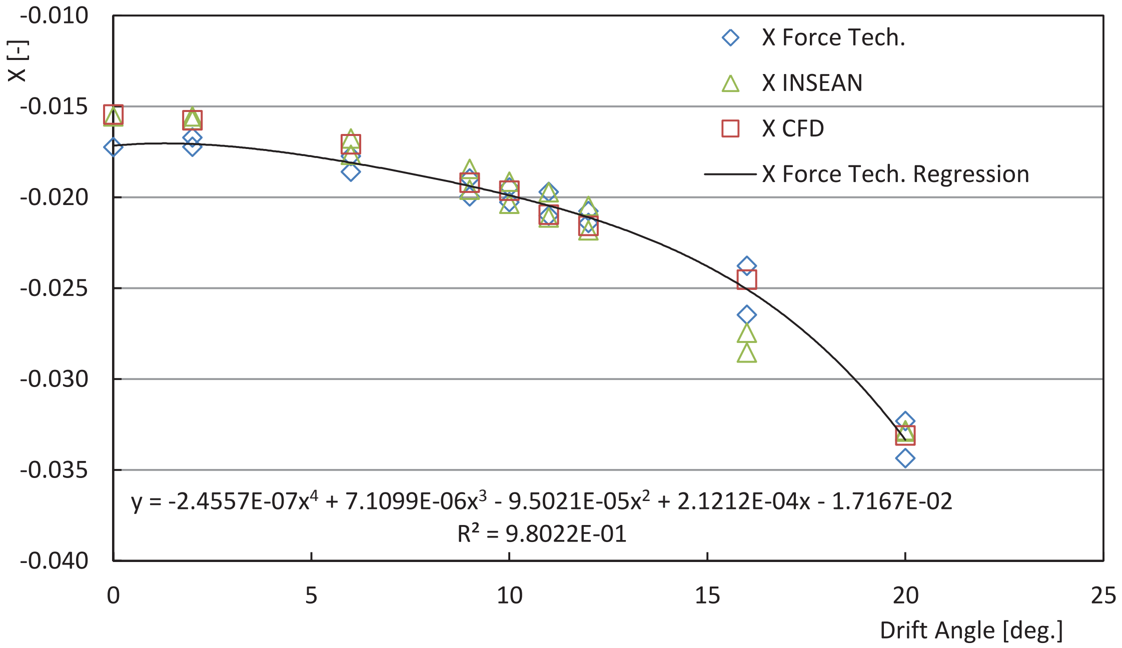

Figure 4.9: Steady Drift X', CFD and Model Tests

Table 4.6 presents the percentage error, $E[\%D]$, between the computed data and the measurements by FORCE Technology. The minimum percentage error between the measurements and computations is at the drift angle of 10°, where the measurements themselves show the minimum discrepancy.

Table 4.6: Steady Drift X' Comparison to Model Tests

Drift Angle	[deg]	0	2	6	9	10	11	12	16	20
E[%D]	[-]	10.4%	5.8%	3.7%	-1.2%	-0.9%	-6.4%	-3.9%	7.3%	-2.5%

The computed Y forces are compared with the measurements in Figure 4.10 and their percentage error is presented in Table 4.7. The high percentage error at the drift angle of 0°, in Table 4.7, is due to the fact that the actual Y at this drift angle is about zero which causes division by a small number in Equation (3.16). Figure 4.10 shows a very good agreement between the measurements and computations.

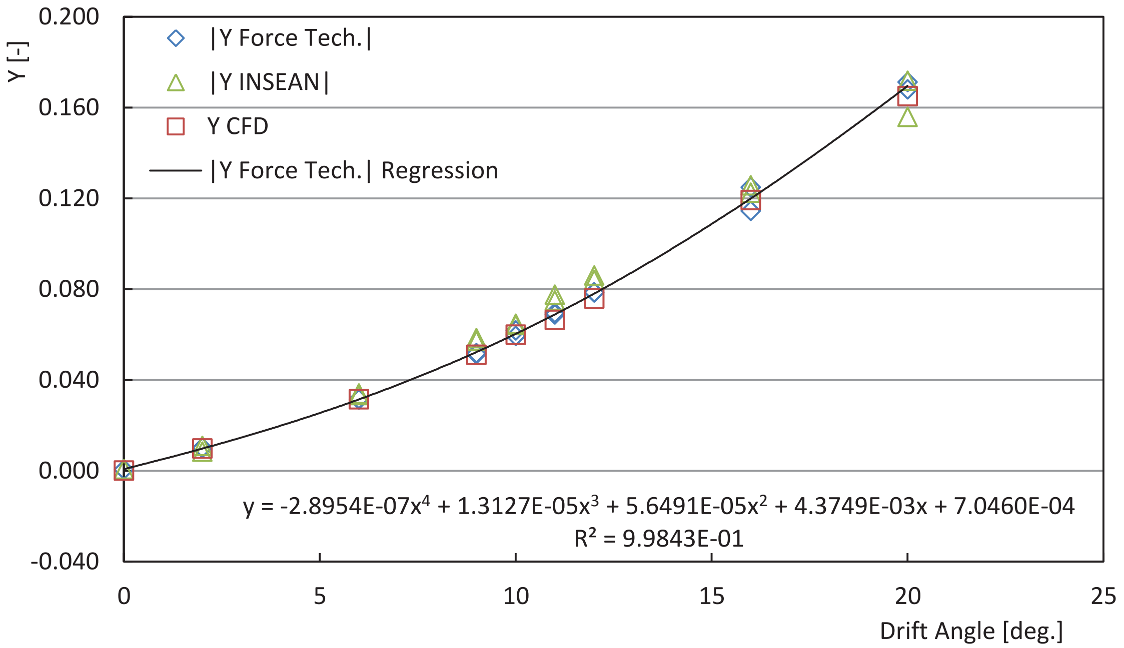

Figure 4.10: Steady Drift Y', CFD and Model Tests

Similar to the Y force, N moment shows a very good agreement with the measurements in Figure 4.11. The high percentage error at the drift angle of 0° in Table 4.8 can be explained in a similar way as explained for Y force in Table 4.7. FORCE Technology measurements, in Figure 4.11, show significant discrepancy at the drift angle of 9°.

Table 4.7: Steady Drift Y' Comparison to Model Tests

Drift Angle	[deg]	0	2	6	9	10	11	12	16	20
E[%D]	[-]	86.3%	3.2%	0.4%	1.2%	2.9%	4.4%	3.3%	-4.2%	3.7%

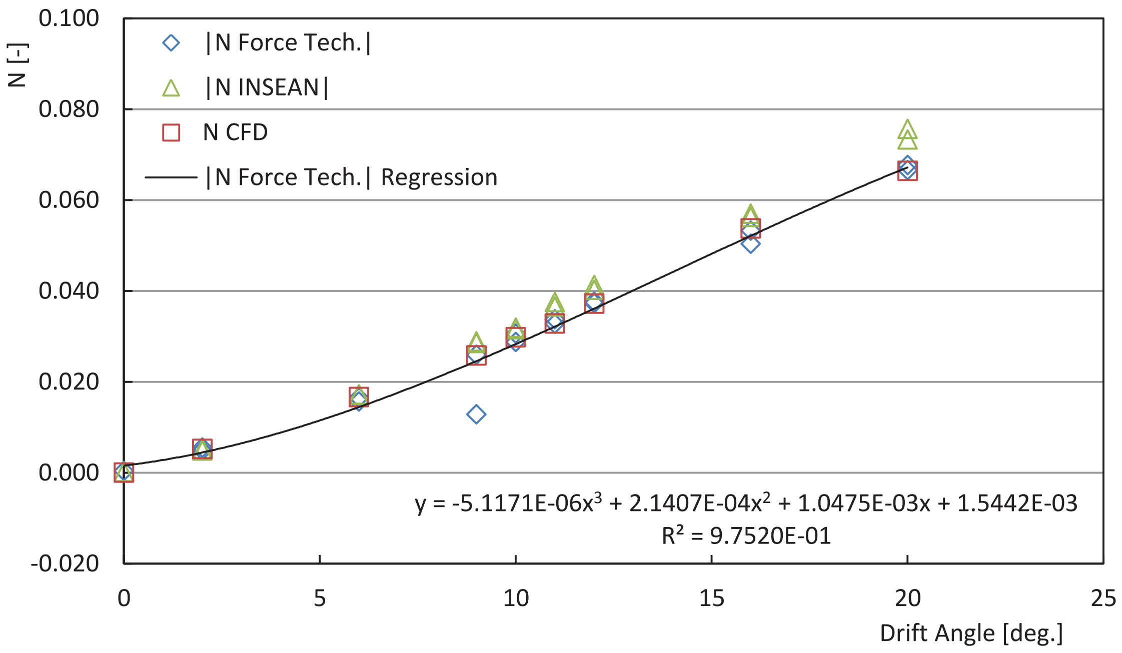

Figure 4.11: Steady Drift Y', CFD and Model Tests

Table 4.8: Steady Drift N', CFD and Model Tests

Drift Angle	[deg]	0	2	6	9	10	11	12	16	20
E[%D]	[-]	101.2%	5.4%	-1.1%	0.5%	2.6%	2.6%	1.0%	-0.07	1.8%

As discussed in Section 3.5, there is an inconsistency in the reported sinkage and trim by FORCE Technology at the drift angle of 0°. When using the sinkage and trim presented in Table 3.6, the percentage error of the computed X at the drift angle of the 0° was 10.6%. This is slightly more than the percentage error presented in Table 4.6. This supports the decision to override the sinkage and trim in Table 3.6 with that in Figure 3.6.

4.2.4 Effect of Bilge Keels

The bilge keels were removed from the model at the drift angle of 10 degrees in order to investigate their effect on flow structure as well as the computed forces and moments acting on the model hull. In Table 4.9 to Table 4.11, compared with the case with bilge keels, results indicate significant reduction in forces but the yaw moment is only slightly reduced.

In Figure 4.12, the vortical structures at midship of the model are compared for the cases with and without the bilge keel. Figure 4.12 indicates that bilge keels significantly contribute to the development of vortical structures. This can be observed in Figure 4.13 where the Q=30 surface generated by bilge keel in Figure 4.13-a completely disappears in Figure 4.13-b. The vortex generated by the model keel near the stern in Figure 4.13-b seems to be completely suppressed by bilge keel strong vortex in Figure 4.13-a. This suppression takes place since vortices have similar direction of rotation. Figure 4.5-c, which presents the same simulation as in Figure 4.13-a but in fine mesh, reveals that the two vortices actually merge when the grid resolution is high enough to eliminate non-physical dissipation of vortices energy.

Table 4.9: Bilge Keel Effect on the Computed X in Steady Drift Test, with the Drift Angle of 10°

Drift Angle	X F.T. BK		X CFD BK		X CFD NBK	
[deg]	[-]	[N]	[-]	[N]	[-]	[N]
10	-0.019465	-20.77	-0.019644	-20.96	-0.01748	-18.649

BK denotes the case with Bilge Keel.
NBK denotes the case without Bilge Keel.

Table 4.10: Bilge Keel Effect on the Computed Y in Steady Drift Test, with the Drift Angle of 10°

Drift Angle	Y F.T. BK		Y CFD BK		Y CFD NBK	
[deg]	[-]	[N]	[-]	[N]	[-]	[N]
10	0.061699	65.84	0.059937	63.96	0.054954	58.643

BK denotes the case with Bilge Keel.
NBK denotes the case without Bilge Keel.

Table 4.11: Bilge Keel Effect on the Computed N in Steady Drift Test, with the Drift Angle of 10°

Drift Angle	N F.T. BK		N CFD BK		N CFD NBK	
[deg]	[-]	[N.m]	[-]	[N.m]	[-]	[N.m]
10	0.030585	130.63	0.029789	127.23	0.029368	125.43

BK denotes the case with Bilge Keel.
NBK denotes the case without Bilge Keel.

A breaking wave can be observed as well in Figure 4.13 on the water surface in the right hand side of the hull. Although these breaking waves seem to be different at first glance, neither the temporal accuracy nor the spatial accuracy permit an appropriate comparison between the two cases. These breaking waves contribute to the nonlinearity of the forces and moments acting on the model as well as generation of noises in the steady state solution.

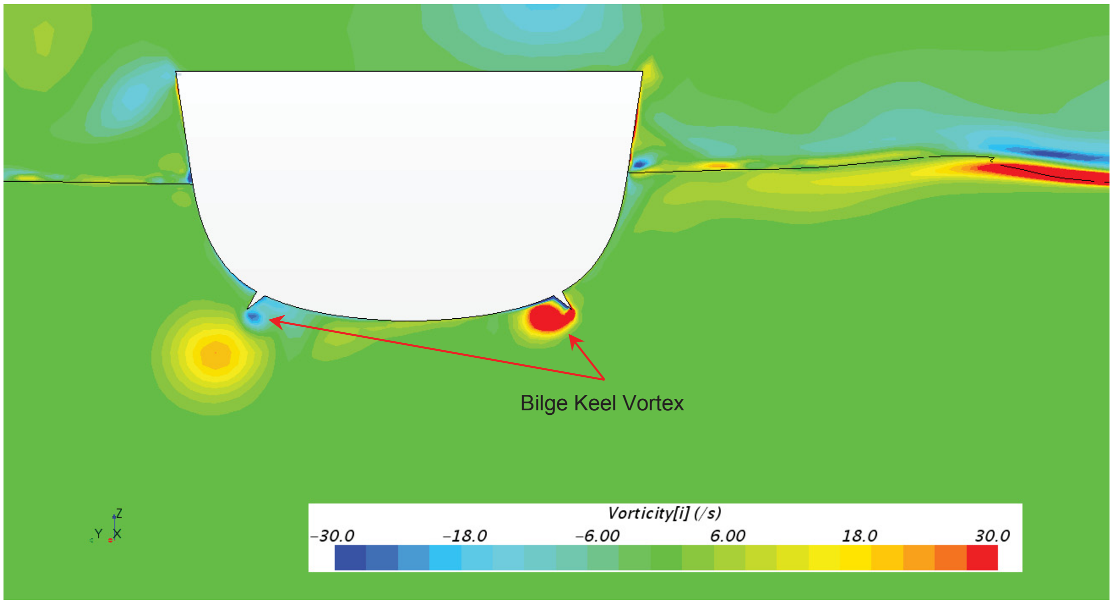

(a) With bilge keels

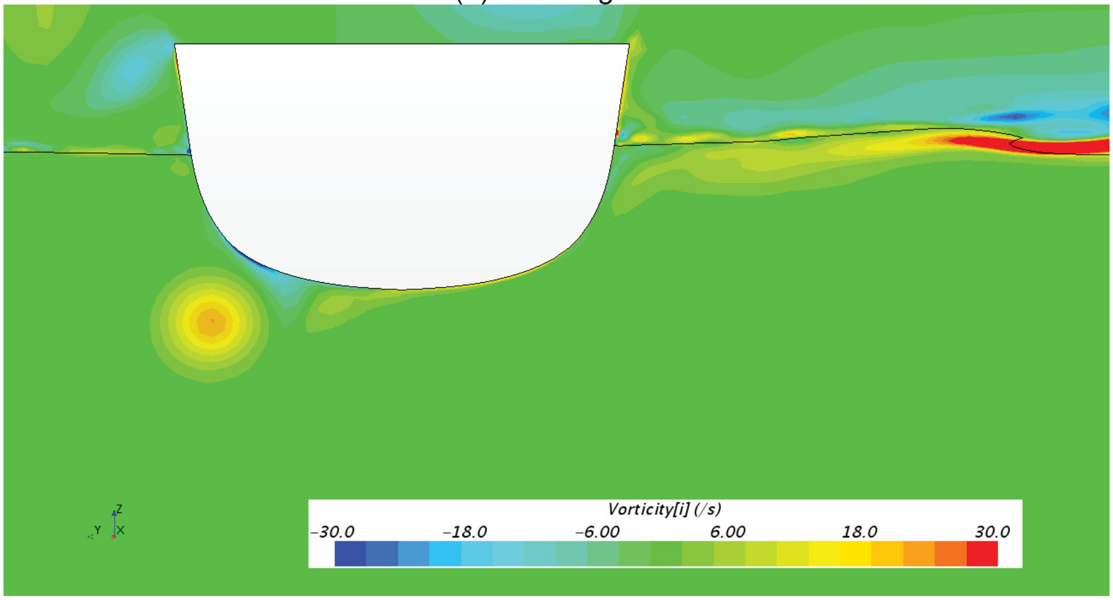

(b) Without bilge keels

Figure 4.12: Bilge Keel Effect on Vorticity, 10° Drift

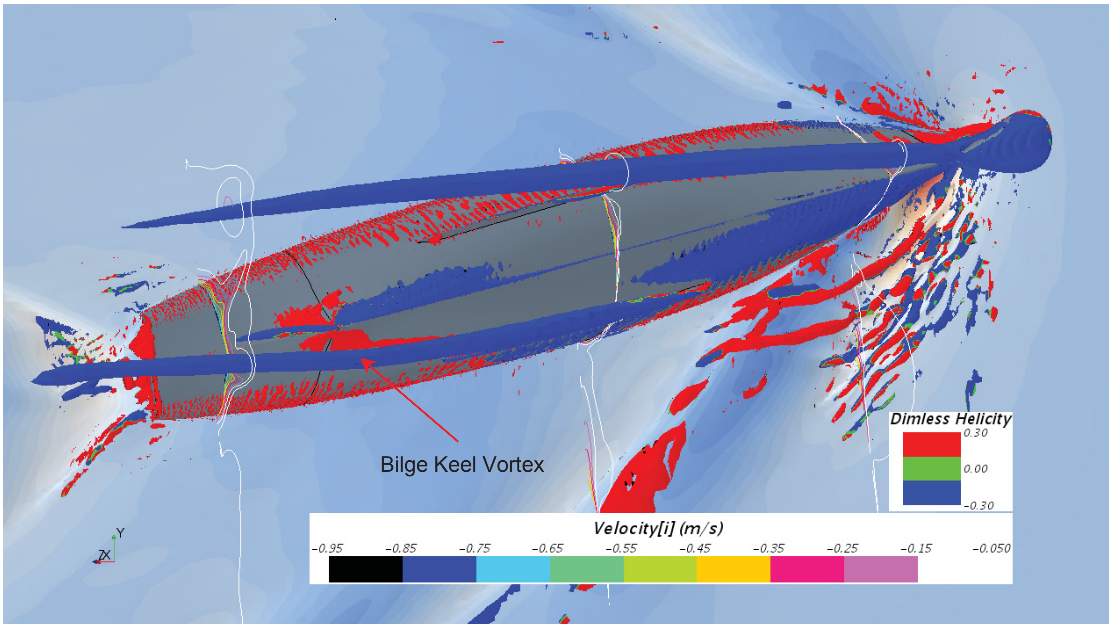

(a) With bilge keels

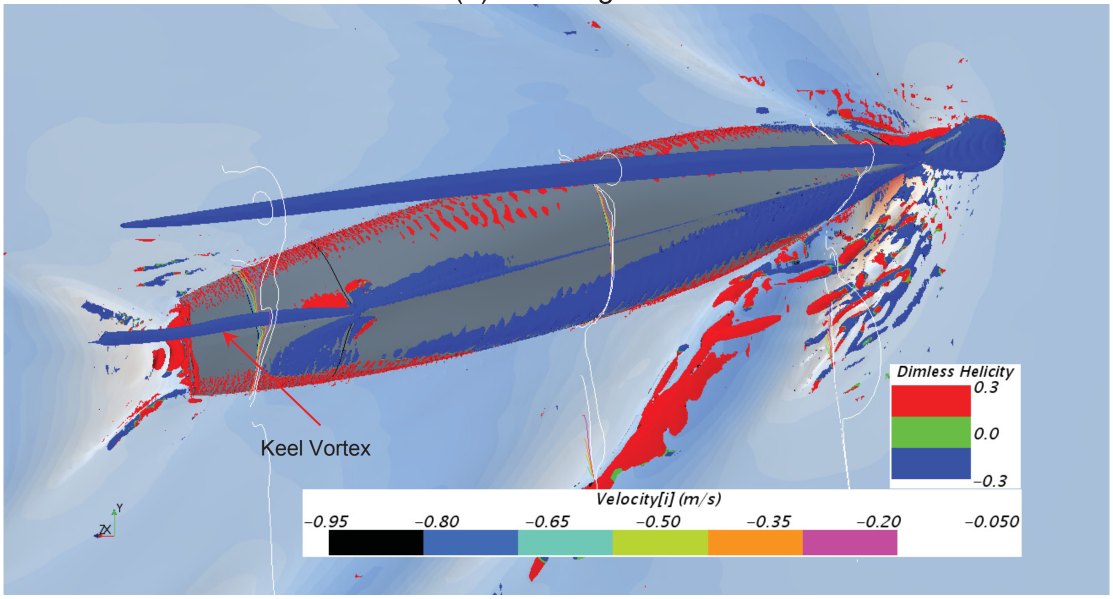

(b) Without bilge keels

Figure 4.13: Bilge Keel Effect on Vortex Structure and Velocity Contours, 10° Drift

4.3 UNSTEADY YAW AND DRIFT

For the unsteady tests to be performed within a reasonable time using a 12-core machine a mesh refinement study was performed for the Run 12 in Table 3.2, and an appropriate mesh was identified. Simulation was then continued by following the simulation matrix in Table 3.2, and forces and moments acting on the model were computed and compared with the measurements. The bilge keel was removed from the model in Run 12 of the

Table 3.2 in order to investigate the effect of the removal of the bilge keel on the computed forces and moments.

4.3.1 Mesh Refinement Study

A comparison of hull pressure disturbance (in HP video files) at the solution time of $t = 35.29s$ (phase angle = 312.258) indicates changes in the asymmetry of the pressure field in the fine mesh compared to the coarse mesh; see Appendix A for reference to the electronic data. Compared to the coarse mesh, the fine mesh can capture the flow structures with smaller length scale. This makes the fine mesh more appropriate for taking account of nonlinearities related to the vortical structures and breaking waves.

At the solution time of $t = 42.457s$ (this is equivalent to the video time of 17s, out of the 19s length of the video) a cloud foam can be observed in the coarse mesh at the port side of the vessel; see HWL_P_C video file. This large volume of foamy water uniformly initiates at the lee side of the bow wave, and almost covers the entire bilge keel. The fine mesh (HWL_P_F video file), however, captures a wavy pattern where the foamy water initiates. The HWLp_F video file (at video time of 17s) clearly depict the small scale plunging breakers at the port side within the first 1m from the FP. This is evident from the sharp change in surface elevation on the port side, at about of 1 m aft of the FP. The HWL_P_F file, however, only shows a green field at this region which identifies a zone with VOF=0.5. For a mesh to be considered of sufficient spatial resolution, a distinct blue zone of VOF=0.0 should be identifiable within this region, unless further refinement demonstrates that the flow mixing is a genuine physical phenomenon. The HWL_P and HWLp video files lead to the conclusion that none of the meshes used are fine enough to capture the breaking wave and resulting foamy flow; i.e. CFD solution is grid dependent at least in terms of VOF method.

The coarse mesh loses the bilge keel vortex at the solution time of $t = 43.2606s$, and it cannot capture the wavy form of the bow-generated vortex; see QC video files. The bow breaking wave is almost smeared out within the diffusive coarse mesh. This high diffusive effect can be observed in VXB video files at $t = 43.2606s$, where the coarse mesh does not resolve the breaking wave at the port side and the vortex near the keel is highly diffused.

A comparison between the computed and measured data in Figure B.1 to Figure B.3 indicates significant noise in the computed data. Further refinement in time and space would be required in order to eliminate these high frequency oscillations. It can be observed in Figure B.1 to Figure B.3 that grid refinement improves the accuracy of the computed forces and moment when compared to the measurements. The CFD predictions for X' include a distinct offset from the experimental data; mesh refinement almost eliminates this offset while bringing the shape of the time-history more in line with that obtained from model tests. The CFD predictions for Y' and N' are relatively close to the respective model test results, with relatively small differences in the overall mean, amplitude, and phase; much of the difference is noise and details of the shapes of the curves. Further temporal and spatial accuracy seems to be necessary for resolving those flow structures which dictate the local curvatures in the profile of the forces and moments.

4.3.2 Spatial Discretization Error

The spatial discretization error has been computed using [3], for each of the Fourier coefficients of the non-dimensional forces. This is presented in Table 4.12, Table 4.13, and Table 4.14. The apparent order and grid convergence index, GCI_{fine}^{21}, are as defined in [3]. The error shown is the product of the grid convergence index and the fine-mesh coefficient in the first row of the table. For consistency with the comparison with model tests, the relative error has been calculated by dividing the error by the maximum absolute value reported in the mean third-order Fourier fit to the experimental data (see Table 4.18). The relative error therefore shows where the inaccuracy in the coefficients is important to the overall fit between the CFD time-history and the experimental time-history.

The classification of some of the Y' Fourier coefficients as divergent reflects a greater difference between the fine-mesh and medium-mesh results when compared to the difference between the medium-mesh and the coarse-mesh results. While this can be an indication of divergence, it can also be an indication of oscillatory convergence or an indication that the mesh refinement is not yet in the asymptotic range. For example, the coarse mesh may be too coarse to capture all of the relevant flow features, so the results from it are not as useful in determining how accurately these features have been captured on the finer meshes. The relative error computed for the Y' coefficients is therefore of questionable accuracy.

The apparent order tends to deviate substantially from the expected value of two for the higher order Fourier coefficients; the grid convergence index also becomes very large for these coefficients. This suggests that the meshes are not sufficiently refined to accurately calculate the spatial discretization error of these coefficients. However as the higher order coefficients are typically quite small compared to the first order coefficients, their accuracy is not as important to the overall accuracy of the CFD prediction, or its potential use in predicting realistic ship manoeuvres.

Table 4.12: Unsteady Spatial Discretization for X' Fourier Coefficients

	C_0	$C_{1,C}$	$C_{1,S}$	$C_{2,C}$	$C_{2,S}$	$C_{3,C}$	$C_{3,S}$
Fine mesh result	-2.20e-2	1.14e-3	-1.41e-3	7.46e-4	-5.89e-4	-2.38e-4	2.68e-5
Medium mesh result	-2.28e-2	8.32e-4	-1.23e-3	4.16e-4	-5.59e-4	-3.06e-4	8.99e-5
Coarse mesh result	-2.40e-2	5.77e-5	-5.81e-4	1.70e-5	-7.42e-5	-2.89e-4	4.86e-4
Convergence type†	M	M	M	M	M	O	M
Apparent order, p	1.96	3.38	4.69	0.94	9.82	4.22	6.55
GCI_{fine}^{21}	5.13%	18.35%	4.84%	164.33%	0.32%	13.38%	44.49%
error	1.13e-3	2.10e-4	6.84e-5	1.23e-3	1.89e-6	3.18e-5	1.19e-5
Relative error	4.80%	0.89%	0.29%	5.21%	0.01%	0.14%	0.05%

† *M: monotonic, O: oscillatory, D: divergent*

Table 4.13: Unsteady Spatial Discretization for Y' Fourier Coefficients

	C_0	$C_{1,C}$	$C_{1,S}$	$C_{2,C}$	$C_{2,S}$	$C_{3,C}$	$C_{3,S}$
Fine mesh result	7.00e-2	-8.27e-3	-2.78e-2	-7.09e-3	-2.00e-3	6.29e-4	5.79e-4
Medium mesh result	6.74e-2	-1.09e-2	-2.78e-2	-8.02e-3	-1.25e-3	-5.48e-4	9.48e-4
Coarse mesh result	6.60e-2	-1.25e-2	-2.63e-2	-8.15e-3	8.34e-4	2.08e-4	1.48e-3
Convergence type†	D	D	M	D	M	O	M
Apparent order, p	1.52	1.16	23.82	5.75	3.73	1.36	1.50
GCI_{fine}^{21}	7.64%	91.0%	5e-6%	3.33%	21.7%	446%	135%
error	5.35e-3	7.53e-3	1.38e-9	2.36e-4	4.34e-4	2.80e-3	7.81e-4
Relative error	0.53%	0.75%	1e-7%	0.02%	0.04%	0.28%	0.08%

† M: monotonic, O: oscillatory, D: divergent

Table 4.14: Unsteady Spatial Discretization for N' Fourier Coefficients

	C_0	$C_{1,C}$	$C_{1,S}$	$C_{2,C}$	$C_{2,S}$	$C_{3,C}$	$C_{3,S}$
Fine mesh result	3.46e-2	-6.06e-3	-2.06e-2	-1.21e-3	-3.20e-5	3.38e-4	2.73e-4
Medium mesh result	3.38e-2	-6.65e-3	-1.99e-2	-1.87e-3	3.53e-4	-4.83e-5	3.43e-4
Coarse mesh result	3.29e-2	-7.43e-3	-1.91e-2	-1.84e-3	8.99e-4	2.21e-4	2.44e-4
Convergence type†	M	M	M	O	M	O	O
Apparent order, p	1.03	1.26	0.93	10.34	1.46	1.12	1.19
GCI_{fine}^{21}	7.10%	25.47%	12.74%	2.90%	2641.32%	346.02%	72.22%
error	2.45e-3	1.54e-3	2.63e-3	3.50e-5	8.45e-4	1.17e-3	1.97e-4
Relative error	4.44%	2.79%	4.75%	0.06%	1.53%	2.12%	0.36%

† M: monotonic, O: oscillatory, D: divergent

4.3.3 Comparison to Model Tests

The plots in Annex A provide a direct comparison of the time-histories as simulated by CFD to those from physical model testing, including both the raw results and the Fourier fit. As discussed in Section 3.12.4, the summarized comparison to model tests is presented here in terms of the Fourier coefficients. Table 4.15 through Table 4.17 provide the Fourier coefficients as computed from the model tests and from the CFD results. Where multiple repeat model tests were carried out, the tables include the minimum, mean, and maximum of the Fourier coefficients determined for the ensemble of tests, and the model test repeatability shown is based on half the range. All values shown as percentages have been normalized by dividing by the maximum absolute value reported in the mean third-order Fourier fit to the experimental data; these are provided in Table 4.18.

The data are presented graphically in Figure 4.14 through Figure 4.16; for reference, the graphs also include case 6, which uses the same non-dimensional yaw amplitude and zero drift.

For the repeated runs at 10° drift + yaw, it is of interest to compare the model test repeatability to the difference between CFD and model test results. Cases where the CFD result does not fall within the range of the model test results, or where the percent difference is greater than the percent repeatability, are shown in bold. This shows that roughly a third of the Fourier coefficients predicted by CFD are within the repeatability of the model tests. Even in the cases where the difference between CFD and the mean model test result is greater than the model test uncertainty, the percent difference is at most 3.29%.

The case with 10° drift + yaw is also the case where the mesh refinement study was carried out. In cases where the percent difference between CFD and model test results exceed the calculated spatial discretization error from Section 4.3.2, the percent difference is shown in italics in Table 4.15 through Table 4.17. This shows that for X' and Y', it is typically the case that if the difference between CFD and model test coefficients exceeds both the model test repeatability and the spatial discretization error. For N', however, the $C_{3,S}$ coefficient is the only one for which the difference between model tests and CFD cannot be accounted for by either model test repeatability or CFD spatial discretization errors.

For the other cases where there were no repeat model test runs or mesh refinement study, the difference between CFD and model test results is generally greater. This is to be expected, due to both the decreased confidence in the model test result and the use of the medium CFD mesh (the fine mesh was used for comparisons at 10° drift + yaw). The only percent difference exceeding 10% is that determined for the C_0 coefficient of X' in the yaw + 11° sway test, where it was 10.61%.

Due to the normalization used, the low percent difference for higher-order Fourier terms, are largely due to the small order of magnitude of the terms themselves and their correspondingly small effect on the overall error, rather than an extremely accurate prediction of the term. It was even found in some cases that the repeated model tests produced higher order Fourier coefficients having opposite signs.

The plots of X' coefficients in Figure 4.14 show non-smooth CFD results from test to test. This is largely due to the use of the fine mesh for the case with 10° drift +yaw and the medium mesh for the other two. The results from the medium mesh at 10° drift + yaw are closer to the linear trend set by the neighbouring results.

For the plots of all of the force results, a similar lack of a smooth trend can sometimes be seen in the experimental results. An extreme example of this is the $C_{1,C}$ coefficient for both Y' and N', as shown by the peak in the curve at 10° drift in Figure 4.15 and Figure 4.16. This appears to be outside the repeatability of the 10° drift + yaw test, and may be an indicator of either complicated non-linear effects or of poor quality model tests.

Table 4.15: Unsteady Yaw and Drift Fourier Coefficients of X', with Model Tests

β		C_0	$C_{1,C}$	$C_{1,S}$	$C_{2,C}$	$C_{2,S}$	$C_{3,C}$	$C_{3,S}$
9°	Model	-2.10e-2	9.39e-4	-2.06e-4	5.88e-4	4.15e-4	-1.23e-4	-8.54e-5
	CFD	-2.21e-2	8.75e-4	-1.02e-3	5.66e-4	-4.17e-4	-1.67e-4	4.66e-5
	Difference	-4.89%	-0.28%	-3.63%	-0.10%	-3.70%	-0.20%	0.59%
10°	Model min.	-2.19e-2	5.33e-4	-1.19e-3	5.81e-4	-2.00e-4	-2.99e-4	-1.80e-4
	Model mean	-2.16e-2	8.37e-4	-1.10e-3	6.83e-4	-3.96e-5	-1.79e-4	-5.43e-5
	Model max.	-2.08e-2	9.21e-4	-6.90e-4	8.07e-4	3.08e-4	1.54e-4	1.09e-4
	Repeatability	2.30%	0.82%	1.06%	0.48%	1.08%	0.96%	0.61%
	CFD	**-2.20e-2**	**1.14e-3**	**-1.41e-3**	7.46e-4	**-5.89e-4**	-2.38e-4	2.68e-5
	Difference	-1.94%	***1.30%***	***-1.33%***	0.27%	***-2.34%***	*-0.25%*	*0.35%*
11°	Model	-2.18e-2	1.32e-3	-5.11e-4	5.47e-4	1.78e-4	-3.25e-4	1.11e-4
	CFD	-2.43e-2	3.13e-4	-1.40e-3	-2.12e-4	-6.17e-4	-5.33e-4	3.69e-4
	Difference	**-10.61%**	-4.24%	-3.76%	-3.20%	-3.36%	-0.88%	1.09%

Table 4.16: Unsteady Yaw and Drift Fourier Coefficients of Y', with Model Tests

β		C_0	$C_{1,C}$	$C_{1,S}$	$C_{2,C}$	$C_{2,S}$	$C_{3,C}$	$C_{3,S}$
9°	Model	5.30e-2	-1.55e-2	-2.40e-2	-5.67e-3	8.43e-5	2.28e-3	7.55e-4
	CFD	6.04e-2	-8.37e-3	-2.43e-2	-5.76e-3	-1.21e-3	7.20e-4	9.46e-4
	Difference	8.43%	8.13%	-0.35%	-0.11%	-1.48%	-1.78%	0.22%
10°	Model min.	6.66e-2	-9.45e-3	-3.06e-2	-7.46e-3	-1.60e-3	1.62e-3	-1.63e-4
	Model mean	6.83e-2	-8.52e-3	-3.01e-2	-7.04e-3	-1.13e-3	1.89e-3	9.86e-5
	Model max.	6.89e-2	-8.16e-3	-2.87e-2	-6.65e-3	-6.71e-4	2.10e-3	2.80e-4
	Repeatability	1.08%	0.61%	0.88%	0.38%	0.43%	0.22%	0.21%
	CFD	**7.00e-2**	-8.27e-3	**-2.78e-2**	-7.09e-3	**-2.00e-3**	**6.29e-4**	**5.79e-4**
	Difference	***1.59%***	0.24%	***2.16%***	*-0.04%*	***-0.82%***	***-1.18%***	***0.45%***
11°	Model	6.99e-2	-1.81e-2	-2.94e-2	-8.06e-3	-4.45e-4	2.39e-3	1.88e-4
	CFD	7.71e-2	-1.24e-2	-3.04e-2	-8.59e-3	-1.11e-3	-3.28e-4	2.47e-4
	Difference	6.50%	5.06%	-0.91%	-0.47%	-0.59%	-2.43%	0.05%

Table 4.17: Unsteady Yaw and Drift Fourier Coefficients of N', with Model Tests

β		C_0	$C_{1,C}$	$C_{1,S}$	$C_{2,C}$	$C_{2,S}$	$C_{3,C}$	$C_{3,S}$
9°	Model	2.58e-2	-9.03e-3	-1.97e-2	-1.51e-3	3.23e-4	4.13e-4	3.14e-4
	CFD	3.02e-2	-5.62e-3	-1.91e-2	-1.09e-3	3.03e-4	3.28e-4	3.06e-4
	Difference	8.93%	6.91%	1.31%	0.86%	-0.04%	-0.17%	-0.02%
10°	Model min.	3.22e-2	-5.14e-3	-2.03e-2	-1.50e-3	-2.30e-5	2.40e-4	3.80e-4
	Model mean	3.27e-2	-4.94e-3	-2.01e-2	-1.32e-3	1.09e-4	3.15e-4	4.91e-4
	Model max.	3.29e-2	-4.74e-3	-1.95e-2	-1.09e-3	2.56e-4	3.90e-4	5.68e-4
	Repeatability	0.66%	0.35%	0.80%	0.37%	0.25%	0.14%	0.17%
	CFD	**3.46e-2**	**-6.06e-3**	**-2.06e-2**	-1.21e-3	**-3.20e-5**	3.38e-4	**2.73e-4**
	Difference	**3.29%**	**-2.03%**	**-0.90%**	*0.20%*	-0.25%	0.04%	***-0.39%***
11°	Model	3.30e-2	-9.56e-3	-2.19e-2	-1.67e-3	8.18e-4	3.84e-4	3.05e-4
	CFD	3.79e-2	-8.00e-3	-2.12e-2	-1.72e-3	1.69e-4	2.80e-4	9.95e-5
	Difference	8.35%	2.63%	1.25%	-0.09%	-1.10%	-0.17%	-0.35%

Table 4.18: Values for Normalizing Unsteady Yaw and Drift Fourier Coefficients

β	X'	Y'	N'
9°	0.02249	0.08764	0.04936
10°	0.02351	0.1067	0.05528
11°	0.02369	0.1117	0.05911

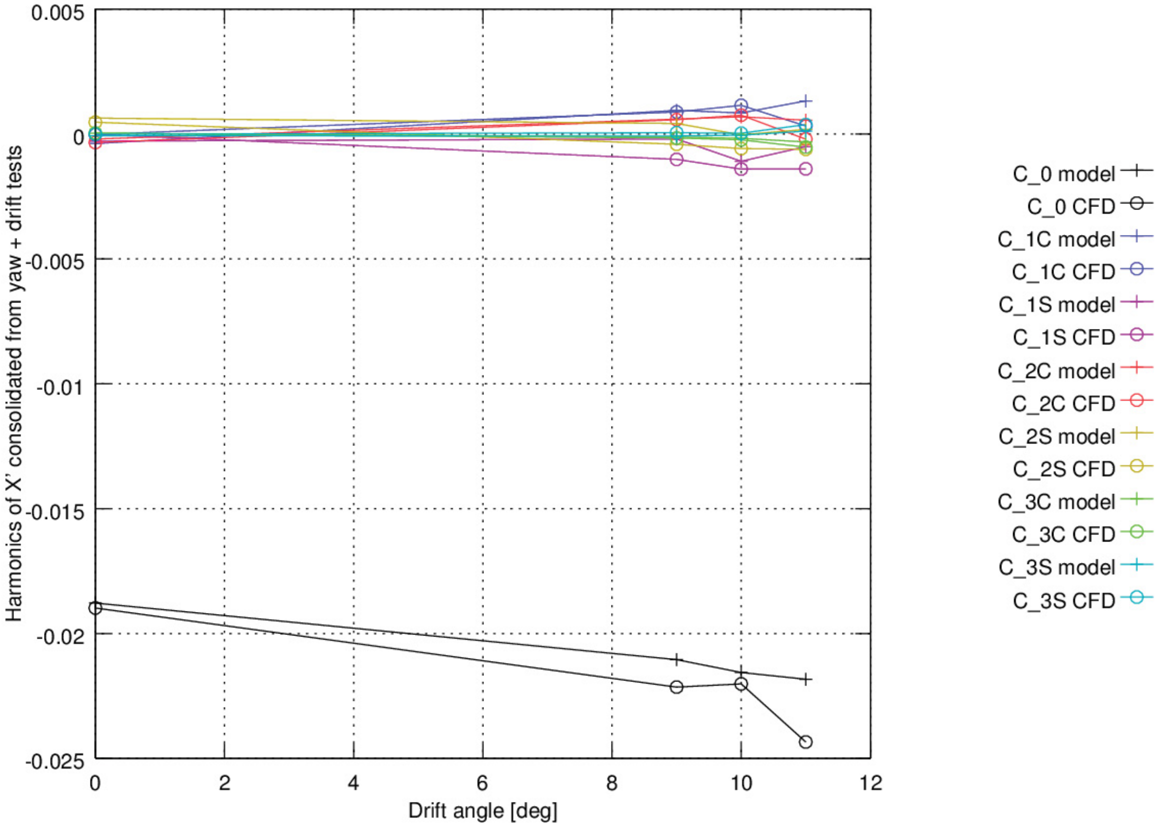

Figure 4.14: Unsteady Yaw and Drift Fourier Coefficients of X', with Model Tests

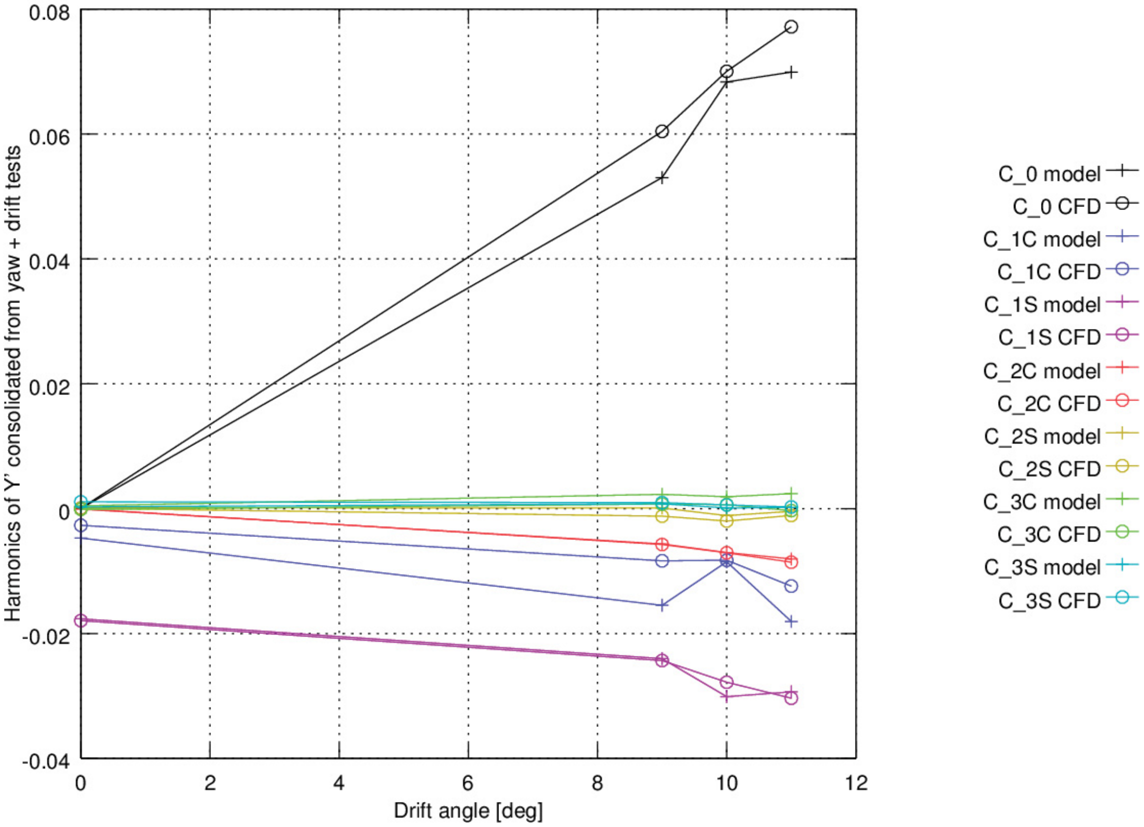

Figure 4.15: Unsteady Yaw and Drift Fourier Coefficients of Y', with Model Tests

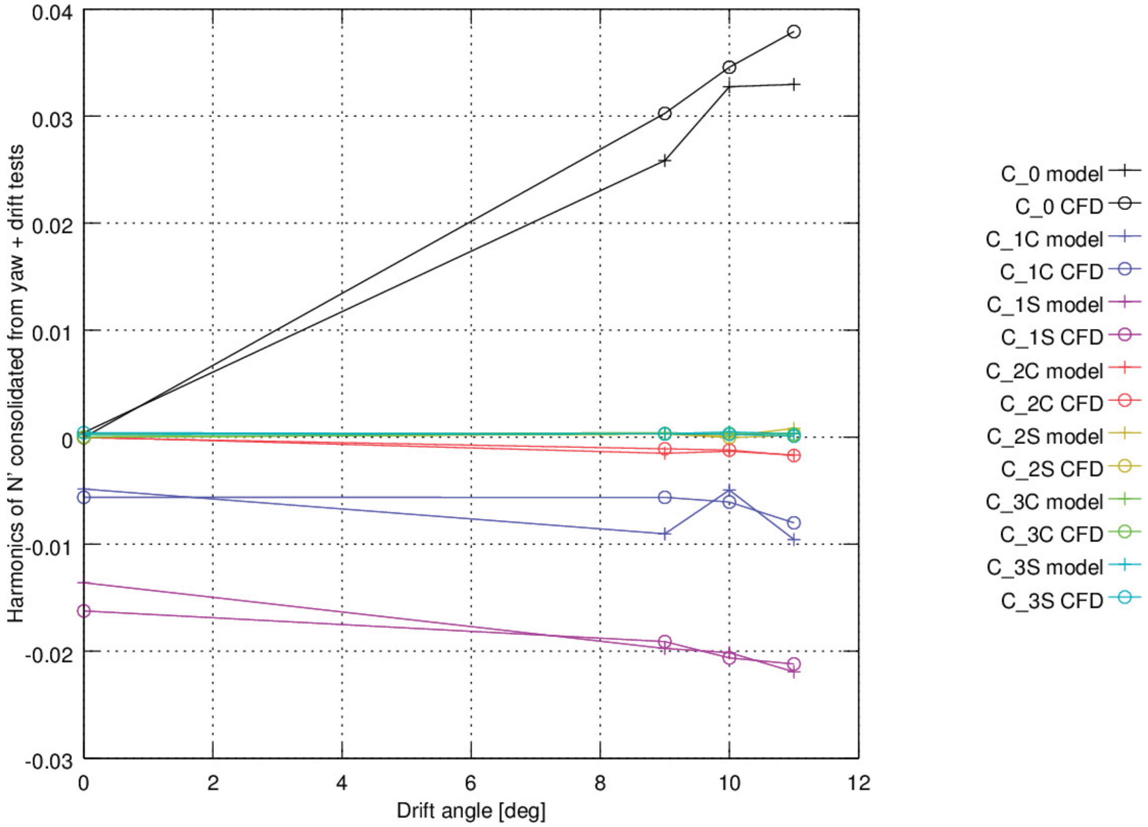

Figure 4.16: Unsteady Yaw and Drift Fourier Coefficients of N', with Model Tests

4.3.4 Effect of Bilge Keels

Bilge Keel effect on the computed X' time-history is presented in Figure B.4. A maximum of about 8% reduction in X' can be observed when bilge keels are removed from the hull. Figure B.5 indicates a phase change in the computed profile of the Y' when bilge keel is removed. The minimum change can be observed in the profile of N' where the removal of the bilge keel only influences the computed maxima and minima; Figure B.6. The effect of the removal of the bilge keel on the computed forces and moments can be more realistically investigated when further refinement in time and space is achieved.

Table 4.20 shows the effect of bilge keels on the Fourier coefficients of each of the forces and moment. It shows that bilge keel removal leads to substantial modifications to only a small number of the Fourier coefficients, which are shown in bold in the table. The $C_{1,C}$ coefficient of Y' is essentially eliminated by bilge keel removal, which is consistent with the phase change in Y' noted above. None of the N' coefficients are strongly affected; this is in contrast to the effect of bilge keels for the other dynamic tests, where the effect on N' is stronger.

The relative differences have been normalized in accordance with Table 4.18.

Table 4.19: Bilge Keel Effect for Unsteady Yaw and 10° Drift

Result		C_0	$C_{1,C}$	$C_{1,S}$	$C_{2,C}$	$C_{2,S}$	$C_{3,C}$	$C_{3,S}$
X'	BK	-2.28e-2	8.32e-4	-1.23e-3	4.16e-4	-5.59e-4	-3.06e-4	8.99e-5
	No BK	-2.08e-2	6.10e-4	-9.89e-4	4.59e-4	-2.82e-4	-3.59e-4	1.31e-4
	Difference	**8.23%**	-0.94%	1.04%	0.18%	1.18%	-0.22%	0.17%
Y'	BK	6.74e-2	-1.09e-2	-2.78e-2	-8.02e-3	-1.25e-3	-5.48e-4	9.48e-4
	No BK	6.44e-2	-6.98e-4	-3.35e-2	-6.43e-3	-2.73e-3	-1.21e-4	9.67e-5
	Difference	-2.82%	**9.53%**	**-5.37%**	1.49%	-1.39%	0.40%	-0.80%
N'	BK	3.38e-2	-6.65e-3	-1.99e-2	-1.87e-3	3.53e-4	-4.83e-5	3.43e-4
	No BK	3.34e-2	-6.70e-3	-1.98e-2	-1.45e-3	3.64e-4	-2.85e-5	2.36e-4
	Difference	-0.77%	-0.09%	0.22%	0.75%	0.02%	0.04%	-0.19%

4.4 UNSTEADY PURE YAW

Simulations for the pure yaw tests have been performed with the medium mesh, as identified in Section 4.3, following the simulation matrix in Table 3.3. Forces and moments acting on the model have been computed and compared with the measurements. The bilge keel was removed from the model in Run 04 of the Table 3.3, and the effect of the removal of the bilge keel on the computed forces and moments has been investigated.

4.4.1 Comparison to Model Tests

The plots in Annex C provide a direct comparison of the time-histories as simulated by CFD to those from physical model testing, including both the raw results and the Fourier fit. As discussed in Section 3.12.4, the summarized comparison to model tests is presented here in terms of the Fourier coefficients. Table 4.20 through Table 4.22 provide the Fourier coefficients as computed from the model tests and from the CFD results. Where multiple repeat model tests were carried out, the tables include the minimum, mean, and maximum of the Fourier coefficients determined for the ensemble of tests, and the model test repeatability shown is based on half the range. All values shown as percentages have been normalized by dividing by the maximum absolute value reported in the mean third-order Fourier fit to the experimental data; these are provided in Table 4.23.

The data are presented graphically in Figure 4.17 through Figure 4.19.

For the repeated runs at $r'_{\max} = 0.30$, it is of interest to compare the model test repeatability to the difference between CFD and model test results. Cases where the CFD result does not fall within the range of the model test results, or where the percent difference is greater than the percent repeatability, are shown in bold. This shows that CFD prediction of the Y' coefficients is generally good, but that CFD predictions of X' and N' Fourier coefficients are not within the repeatability of the model tests. Nonetheless, the X' coefficients are all within 1.87% of the mean from the repeat model tests. Notable outliers are the $C_{1,C}$ coefficient for Y' and the $C_{1,S}$ coefficient for N'.

For the cases where there were no repeat model test runs, the difference between CFD and model test results is generally greater. This is to be expected, due to the decreased confidence in the model test results. Cases where the percent difference exceeds 10% are shown in bold.

A notable outlier is case 5, where r'_{max} is 0.15, where there is considerable disagreement between the model tests and CFD. The model test results for this case appear as an outlier in Table 4.20 through Table 4.22, so it appears to be the case that the model test data for this test is corrupt. The results for this model test have therefore been omitted from Figure 4.17 through Figure 4.19.

For both the Y' and N' results, the $C_{1,S}$ coefficient is typically the largest contributor to the overall difference from the model test results. This is to be expected, as it is also typically the largest Fourier coefficient.

For these tests, symmetry is expected such that the mean (C_0 coefficient) for both Y' and N' be zero. It can be seen in the results that the CFD simulations typically exhibit this with more accuracy than do the model test results. Due to symmetry, one would also expect that the $C_{1,C}$ and $C_{1,S}$ coefficients of X' be zero; this is similarly achieved with better accuracy by CFD than in the model tests. These trends reflect the relative difficulty of achieving perfect symmetry in model tests.

Due to the normalization used, the low percent difference for higher-order Fourier terms are largely due to the small order of magnitude of the terms themselves and their correspondingly small effect on the overall error, rather than an extremely accurate prediction of the term. It was even found in some cases that the repeated model tests produced higher order Fourier coefficients having opposite signs.

Barring the apparently corrupt test 5, the plots typically show smooth trends for the important Fourier coefficients (i.e. those that are relatively large). The only notable exception to this is the $C_{2,C}$ coefficient of X': both model tests and CFD predict this to abruptly begin increasing as r'_{max} exceeds about 0.45 (see Figure 4.17).

Table 4.20: Unsteady Pure Yaw Fourier Coefficients of X', with Model Tests

$r'_{\max}$		C_0	$C_{1,C}$	$C_{1,S}$	$C_{2,C}$	$C_{2,S}$	$C_{3,C}$	$C_{3,S}$
0.05	Model	-1.69e-2	-9.78e-5	-1.09e-4	1.60e-6	7.86e-5	-1.64e-5	-5.17e-5
	CFD	-1.78e-2	1.97e-5	-8.26e-6	1.54e-4	3.42e-5	2.24e-5	2.65e-5
	Difference	-5.28%	0.69%	0.59%	0.90%	-0.26%	0.23%	0.46%
0.15	Model	-2.21e-2	-9.88e-4	-2.25e-5	4.59e-4	7.69e-4	2.74e-5	5.08e-6
	CFD	-1.80e-2	-2.84e-5	-5.07e-5	-3.20e-5	9.53e-5	-6.64e-6	-4.06e-5
	Difference	**17.48%**	4.06%	-0.12%	-2.08%	-2.85%	-0.14%	-0.19%
0.30	Model min.	-1.89e-2	-4.22e-4	-3.45e-4	-3.30e-4	5.78e-4	-2.14e-5	-1.94e-4
	Model mean	-1.88e-2	-3.88e-4	-2.90e-4	-2.08e-4	6.29e-4	2.75e-5	-7.79e-5
	Model max.	-1.87e-2	-3.35e-4	-2.07e-4	-1.46e-4	6.86e-4	9.78e-5	-1.71e-6
	Repeatability	0.63%	0.22%	0.35%	0.47%	0.28%	0.30%	0.49%
	CFD	**-1.90e-2**	**-2.32e-5**	**-1.63e-5**	**-3.49e-4**	**4.66e-4**	3.14e-5	-1.67e-5
	Difference	**-1.02%**	**1.87%**	**1.40%**	**-0.72%**	**-0.84%**	0.02%	0.31%
0.45	Model	-2.01e-2	-5.53e-4	-2.58e-4	2.15e-4	7.91e-4	4.34e-5	-1.70e-4
	CFD	-2.08e-2	2.81e-5	8.26e-6	-1.21e-4	9.91e-4	-5.01e-5	3.45e-5
	Difference	-3.18%	2.76%	1.27%	-1.59%	0.95%	-0.44%	0.97%
0.60	Model	-2.20e-2	-5.86e-4	-3.40e-4	2.52e-3	6.27e-4	1.25e-4	-2.70e-4
	CFD	-2.26e-2	-1.20e-4	4.90e-5	1.98e-3	4.81e-4	-1.19e-4	1.94e-5
	Difference	-2.37%	1.89%	1.58%	-2.20%	-0.59%	-0.99%	1.17%
0.75	Model	-2.38e-2	-6.18e-4	-4.50e-4	4.73e-3	9.60e-4	1.67e-4	-1.51e-4
	CFD	-2.42e-2	-2.14e-4	9.31e-5	3.88e-3	1.01e-4	-1.36e-4	1.46e-5
	Difference	-1.62%	1.40%	1.88%	-2.96%	-2.98%	-1.05%	0.58%

Table 4.21: Unsteady Pure Yaw Fourier Coefficients of Y', with Model Tests

$r'_{\max}$		C_0	$C_{1,C}$	$C_{1,S}$	$C_{2,C}$	$C_{2,S}$	$C_{3,C}$	$C_{3,S}$
0.05	Model	-2.15e-4	-9.64e-4	-2.55e-3	9.30e-5	2.09e-5	-2.84e-4	-3.00e-4
	CFD	-2.56e-6	-6.28e-5	-2.95e-3	1.41e-5	6.00e-5	-7.51e-5	7.88e-5
	Difference	7.89%	**33.50%**	**-14.84%**	-2.93%	1.46%	7.76%	**14.10%**
0.15	Model	-1.87e-4	-6.87e-2	2.84e-2	3.70e-4	-2.03e-4	4.29e-3	-3.27e-3
	CFD	1.48e-5	-7.47e-4	-8.60e-3	1.72e-5	8.22e-5	8.11e-5	1.81e-4
	Difference	0.29%	**96.12%**	**-52.38%**	-0.50%	0.40%	-5.95%	4.88%
0.30	Model min.	-3.80e-4	-5.12e-3	-1.80e-2	-2.51e-4	-4.03e-5	3.17e-4	2.07e-4
	Model mean	2.02e-5	-4.73e-3	-1.77e-2	-9.19e-5	1.56e-4	4.29e-4	2.65e-4
	Model max.	3.68e-4	-4.38e-3	-1.73e-2	6.33e-5	3.92e-4	5.30e-4	3.03e-4
	Repeatability	1.97%	1.96%	2.05%	0.83%	1.14%	0.56%	0.25%
	CFD	2.89e-5	**-2.68e-3**	-1.79e-2	-2.89e-5	4.04e-5	**-1.25e-4**	**1.07e-3**
	Difference	0.05%	**10.82%**	-1.50%	0.33%	-0.61%	**-2.92%**	**4.26%**
0.45	Model	1.44e-4	-7.41e-3	-2.93e-2	-4.04e-4	1.62e-4	1.59e-3	2.42e-3
	CFD	1.35e-4	-6.17e-3	-2.76e-2	1.35e-5	-8.12e-5	1.15e-3	3.44e-3
	Difference	-0.03%	3.69%	4.87%	1.24%	-0.72%	-1.30%	3.03%
0.60	Model	4.78e-4	-1.39e-2	-4.16e-2	-3.21e-4	2.84e-4	2.02e-3	5.56e-3
	CFD	1.10e-4	-1.51e-2	-3.50e-2	-3.15e-4	-1.77e-4	2.09e-3	7.15e-3
	Difference	-0.73%	-2.50%	**12.99%**	0.01%	-0.92%	0.14%	3.18%
0.75	Model	3.58e-4	-1.81e-2	-5.52e-2	-6.66e-4	-1.79e-4	5.37e-3	9.73e-3
	CFD	4.82e-5	-2.12e-2	-4.54e-2	-6.00e-4	-2.36e-4	4.48e-3	1.10e-2
	Difference	-0.44%	-4.41%	**14.05%**	0.10%	-0.08%	-1.28%	1.77%

Table 4.22: Unsteady Pure Yaw Fourier Coefficients of N', with Model Tests

$r'_{\max}$		C_0	$C_{1,C}$	$C_{1,S}$	$C_{2,C}$	$C_{2,S}$	$C_{3,C}$	$C_{3,S}$
0.05	Model	3.00e-4	-1.18e-3	-2.21e-3	2.36e-5	2.84e-5	1.51e-4	-1.41e-4
	CFD	-1.92e-5	-1.08e-3	-2.59e-3	-1.28e-5	2.65e-7	-8.60e-6	-2.28e-5
	Difference	**-10.67%**	3.21%	**-12.70%**	-1.22%	-0.94%	-5.36%	3.95%
0.15	Model	3.14e-4	-4.04e-2	-1.54e-2	2.10e-4	1.34e-5	1.04e-3	-4.34e-4
	CFD	-1.67e-5	-3.10e-3	-7.79e-3	-3.51e-5	-7.29e-6	4.85e-5	6.00e-5
	Difference	-0.76%	**85.24%**	**17.48%**	-0.56%	-0.05%	-2.28%	1.13%
0.30	Model min.	2.04e-4	-5.06e-3	-1.38e-2	-4.29e-5	-6.06e-5	2.59e-4	2.08e-4
	Model mean	4.33e-4	-4.84e-3	-1.36e-2	7.08e-6	2.02e-5	2.76e-4	2.40e-4
	Model max.	6.30e-4	-4.65e-3	-1.34e-2	6.54e-5	1.19e-4	3.01e-4	2.72e-4
	Repeatability	1.40%	1.35%	1.07%	0.36%	0.59%	0.14%	0.21%
	CFD	**-2.17e-5**	**-5.62e-3**	**-1.62e-2**	**-4.91e-5**	-3.00e-6	**4.84e-6**	**4.16e-4**
	Difference	**-2.99%**	**-5.08%**	**-17.28%**	**-0.37%**	-0.15%	**-1.78%**	**1.15%**
0.45	Model	6.64e-4	-6.74e-3	-2.23e-2	-6.95e-5	-7.51e-5	3.75e-4	1.36e-3
	CFD	3.26e-5	-8.25e-3	-2.52e-2	-6.41e-5	-4.71e-5	3.77e-4	1.58e-3
	Difference	-2.50%	-5.99%	**-11.40%**	0.02%	0.11%	0.01%	0.90%
0.60	Model	6.91e-4	-1.11e-2	-3.31e-2	6.57e-5	8.59e-5	5.12e-4	3.21e-3
	CFD	1.44e-5	-1.37e-2	-3.60e-2	4.57e-5	-1.04e-4	5.13e-4	3.03e-3
	Difference	-1.77%	-6.69%	-7.46%	-0.05%	-0.50%	0.00%	-0.46%
0.75	Model	6.79e-4	-1.35e-2	-4.42e-2	6.75e-5	-7.10e-6	1.08e-3	6.20e-3
	CFD	3.28e-5	-1.67e-2	-4.67e-2	1.13e-4	-1.03e-4	1.17e-3	5.14e-3
	Difference	-1.23%	-6.25%	-4.67%	0.09%	-0.18%	0.18%	-2.02%

Table 4.23: Values for Normalizing Unsteady Pure Yaw Fourier Coefficients

$r'_{\max}$	X'	Y'	N'
0.05	0.01702	0.00269	0.00299
0.15	0.02361	0.07070	0.04370
0.30	0.01955	0.01896	0.01524
0.45	0.02106	0.03364	0.02525
0.60	0.02463	0.05010	0.03826
0.75	0.02883	0.06966	0.05244

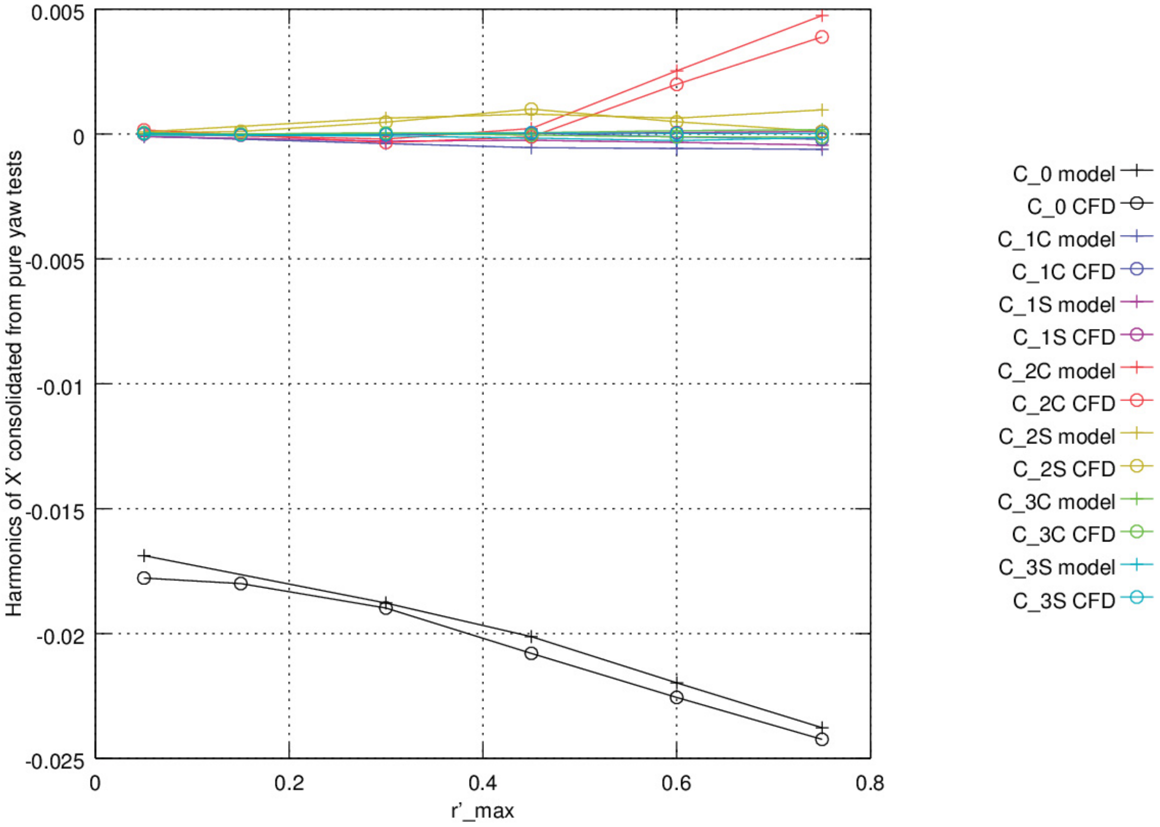

Figure 4.17: Unsteady Pure Yaw Fourier Coefficients of X', With Model Tests

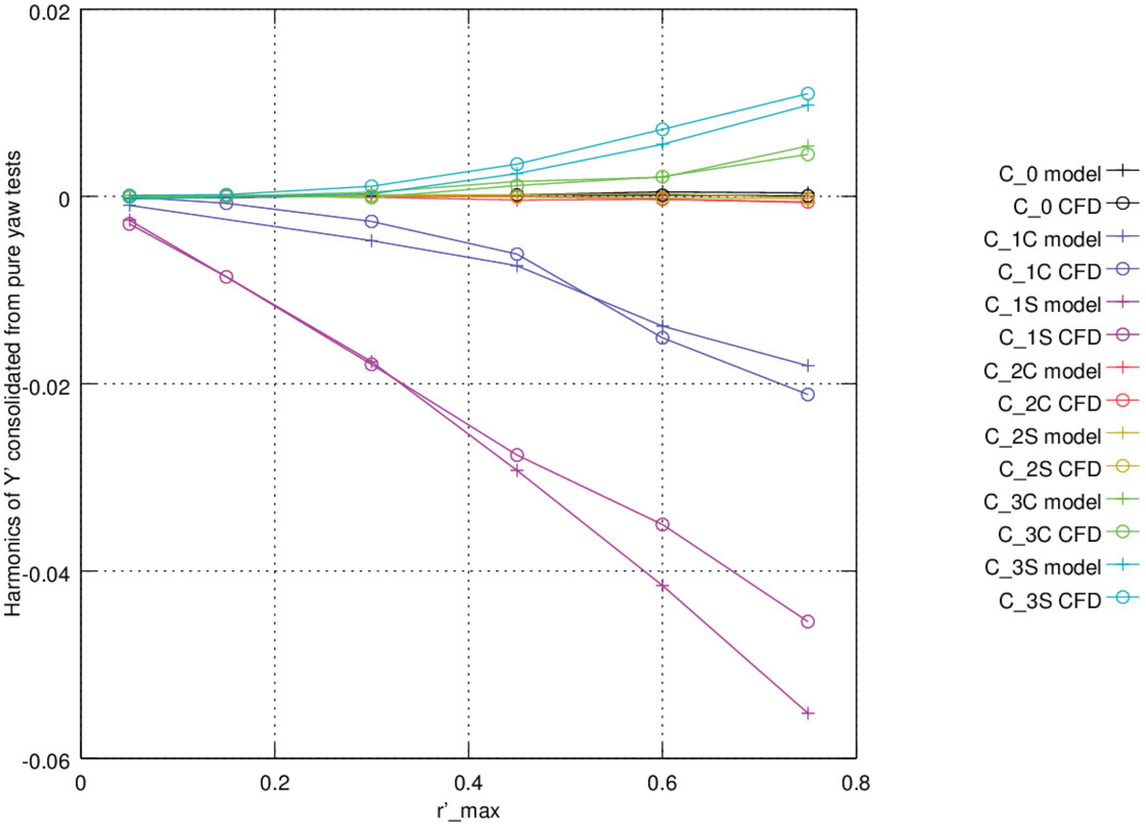

Figure 4.18: Unsteady Pure Yaw Fourier Coefficients of Y', With Model Tests

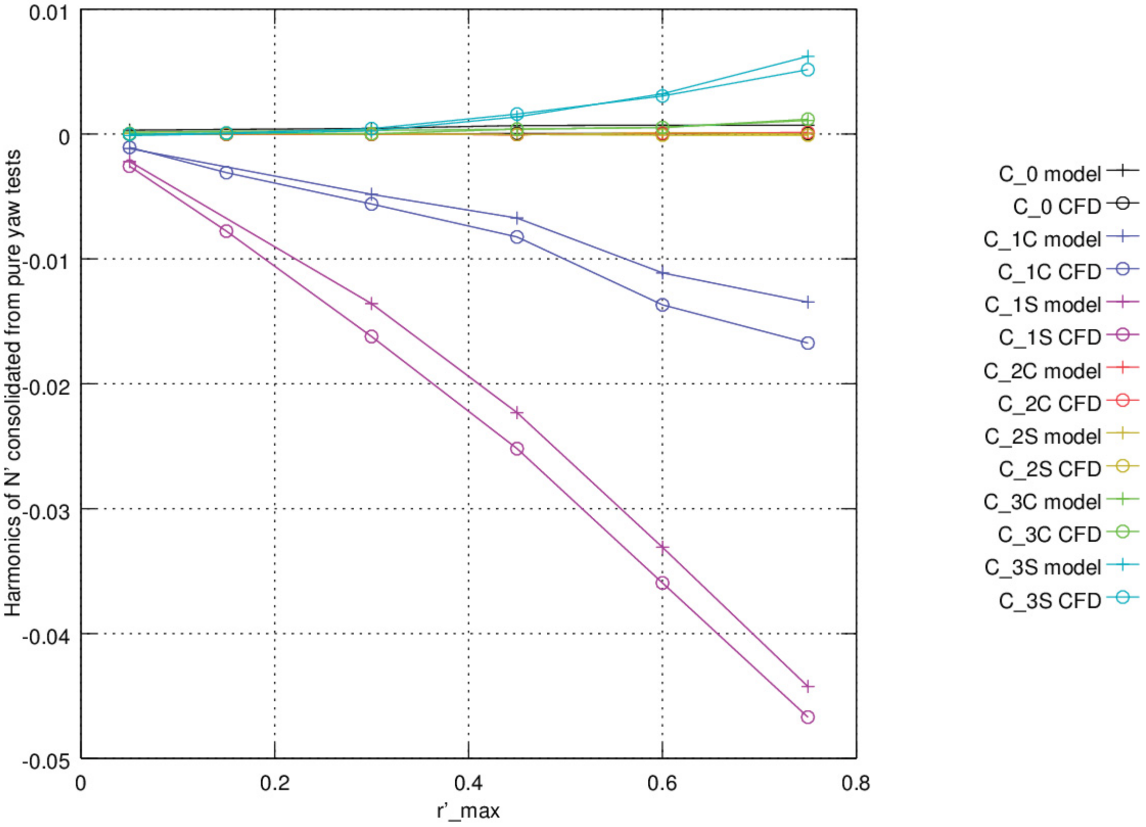

Figure 4.19: Unsteady Pure Yaw Fourier Coefficients of N', With Model Tests

4.4.2 Effect of Bilge Keels

As discussed in Section 5.1, the simulations of the pure yaw test 4 with and without bilge keels were initially set up with differing draft and trim. As a result, the bilge keel sensitivity discussed below for the pure yaw case is likely obscured by the effects of the draft and trim difference.

Neither experiment nor the performed CFD simulation indicates sufficient resolution for capturing the oscillations of X' in Figure C.1. Fourier representation of X' only removes the high frequency oscillations, leaving the low frequency oscillations superimposed on a mean value. The low frequency oscillations, in Figure C.1, can hardly be declared as true X' and, in turn, the bilge keel effect on the computed X' can only be studied in term of the mean values. As it was expected, removal of the bilge keel from the hull significantly reduces the computed X'.

Larger erroneous oscillations can be observed in the measured Y' in Figure C.2 compared with the computations. The small difference between the simulations with and without bilge keel cannot be entirely interpreted as the effect of the removal of the bilge keel. Part of this difference is due to the insufficiency of the spatial and temporal accuracy. A small phase change can be observed in the profile of Y' when the bilge keels are removed, which is in accordance with the observations in Figure B.5.

The inclusion of the bilge keel on the hull of the vessel increases the absolute magnitude of the maxima and minima in the computed profile of N'; see Figure C.3. This slightly differs with the pattern observed in Figure B.6.

Table 4.24 shows the effect of bilge keels on the Fourier coefficients of each of the forces and moment. It shows that bilge keel removal in substantial modifications to only a small number of the Fourier coefficients, which are shown in bold in the table.

The relative differences have been normalized in accordance with Table 4.23.

Table 4.24: Bilge Keel Effect for Unsteady Pure Yaw; $r'_{\max} = 0.05$

Result		C_0	$C_{1,C}$	$C_{1,S}$	$C_{2,C}$	$C_{2,S}$	$C_{3,C}$	$C_{3,S}$
X'	BK	-1.78e-2	1.97e-5	-8.26e-6	1.54e-4	3.42e-5	2.24e-5	2.65e-5
	No BK	-1.54e-2	-1.86e-5	-2.99e-7	7.64e-5	-7.90e-5	-1.86e-6	-1.98e-5
	Difference	**13.74%**	-0.23%	0.05%	-0.46%	-0.66%	-0.14%	-0.27%
Y'	BK	-2.56e-6	-6.28e-5	-2.95e-3	1.41e-5	6.00e-5	-7.51e-5	7.88e-5
	No BK	8.41e-6	2.86e-4	-2.96e-3	-1.99e-5	3.61e-5	5.01e-6	4.81e-6
	Difference	0.41%	**12.97%**	-0.55%	-1.27%	-0.89%	2.98%	-2.75%
N'	BK	-1.92e-5	-1.08e-3	-2.59e-3	-1.28e-5	2.65e-7	-8.60e-6	-2.28e-5
	No BK	6.64e-7	-8.86e-4	-2.19e-3	-3.11e-6	-6.75e-6	6.36e-6	-1.75e-6
	Difference	0.66%	**6.57%**	**13.40%**	0.33%	-0.23%	0.50%	0.70%

4.5 UNSTEADY PURE SWAY

Similar to the other unsteady tests, the simulations for the pure sway tests were also performed with the medium mesh. The simulation matrix in Table 3.4 has been followed and the forces and moments acting on the model have been computed and compared with the measurements. The bilge keel has been removed from the model in Run 01 of the Table 3.4, and the effect of the removal of the bilge keel on the computed forces and moments has been investigated.

4.5.1 Comparison to Model Tests

The plots in Appendix A provide a direct comparison of the time-histories as simulated by CFD to those from physical model testing, including both the raw results and the Fourier fit. As discussed in Section 3.12.4, the summarized comparison to model tests is presented here in terms of the Fourier coefficients. Table 4.25 through Table 4.27 provide the Fourier coefficients as computed from the model tests and from the CFD results. Where multiple repeat model tests were carried out, the tables include the minimum, mean, and maximum of the Fourier coefficients determined for the ensemble of tests, and the model test repeatability shown is based on half the range. All values shown as percentages have been normalized by dividing by the maximum absolute value reported in the mean third-order Fourier fit to the experimental data; these are provided in Table 4.28.

The data are presented graphically in Figures Figure 4.20 through Figure 4.22. The trends shown are generally smooth and nearly linear.

For the repeated runs at $v'_{\max} = 0.17$, it is of interest to compare the model test repeatability to the difference between CFD and model test results. Cases where the CFD result does not fall within the range of the model test results, or where the percent difference is greater than the percent repeatability, are shown in bold. For X', the mean value is 4.1% greater magnitude than the model test result, while the model test repeatability is only 0.8%. The $C_{1,C}$ and $C_{1,S}$ coefficients of X' are also outside the range found in the model tests; however, the expected value due to symmetry considerations is zero, and the CFD results are closer to zero than are the model test results. The difference between CFD and mean model test prediction of the Y' and N' coefficients is up to about 15% and 11%, respectively. The 12 repeated model tests, however, show much better agreement with each other in these cases.

For the cases where there were no repeat model test runs, the difference between CFD and model test results tends to be greater. This is to be expected, due to the decreased confidence in the model test results. Cases where the percent difference exceeds 10% are shown in bold.

While it is not obvious from the Fourier coefficients, the model test time-histories for case 1 with $v'_{\max} = 0.03$ show substantial noise. This is to be expected for a test with small motion, for which the developed forces may be quite small as compared to the capacity of the load cells used.

For the X' results, the comparison between CFD and model test predictions of the mean value is nearly consistent for all three tests. From the time-histories, it appears to be the case that for the tests with smaller motions, all of the harmonic terms tend towards random noise.

Both the Y' and N' results are relatively close to sinusoidal, and the discussion of the difference between model tests and CFD for the case with repeated model tests appears to hold true for the unrepeated tests as well.

For these tests, symmetry is expected such that the mean (C_0 coefficient) for both Y' and N' be zero. It can be seen in the results that the CFD simulations typically exhibit this with more accuracy than do the model test results. Due to symmetry, one would also expect that the $C_{1,C}$ and $C_{1,S}$ coefficients of X' be zero; this is similarly achieved with better accuracy by CFD than in the model tests. These trends reflect the relative difficulty of achieving perfect symmetry in model tests.

Due to the normalization used, the low percent difference for higher-order Fourier terms are largely due to the small order of magnitude of the terms themselves and their correspondingly small effect on the overall error, rather than an extremely accurate prediction of the term. It was even found in some cases that the repeated model tests produced higher order Fourier coefficients having opposite signs.

Table 4.25: Unsteady Pure Sway Fourier Coefficients of X', with Model Tests

$v'_{\max}$		C_0	$C_{1,C}$	$C_{1,S}$	$C_{2,C}$	$C_{2,S}$	$C_{3,C}$	$C_{3,S}$
0.03	Model	-1.72e-2	3.60e-5	-4.28e-5	-9.30e-5	4.60e-5	-4.07e-6	1.39e-4
	CFD	-1.80e-2	-2.00e-5	-3.63e-5	1.04e-4	1.53e-4	2.21e-5	-3.15e-5
	Difference	-4.49%	-0.32%	0.04%	1.13%	0.62%	0.15%	-0.98%
0.07	Model	-1.77e-2	9.85e-5	-7.84e-5	-1.32e-4	1.96e-4	-3.17e-5	-1.43e-5
	CFD	-1.84e-2	-1.52e-5	6.31e-6	1.46e-4	9.03e-5	1.42e-5	-4.38e-5
	Difference	-4.30%	-0.63%	0.47%	1.54%	-0.58%	0.25%	-0.16%
0.17	Model min.	-2.03e-2	3.01e-4	-2.14e-4	-8.14e-4	6.15e-4	-1.39e-4	-7.40e-5
	Model mean	-2.01e-2	3.69e-4	-1.45e-4	-6.78e-4	7.42e-4	-3.98e-5	1.29e-7
	Model max.	-1.99e-2	4.46e-4	-2.54e-5	-5.09e-4	8.54e-4	7.62e-5	5.06e-5
	Repeatability	0.84%	0.34%	0.44%	0.71%	0.56%	0.50%	0.29%
	CFD	**-2.10e-2**	**-1.11e-4**	**2.38e-5**	**-1.63e-4**	**4.26e-4**	9.93e-6	**-8.21e-5**
	Difference	**-4.10%**	**-2.23%**	**0.78%**	**2.39%**	**-1.47%**	0.23%	**-0.38%**

Table 4.26: Unsteady Pure Sway Fourier Coefficients of Y', With Model Tests

$v'_{\max}$		C_0	$C_{1,C}$	$C_{1,S}$	$C_{2,C}$	$C_{2,S}$	$C_{3,C}$	$C_{3,S}$
0.03	Model	5.25e-4	8.47e-3	-5.97e-3	1.47e-4	-3.20e-5	-1.14e-4	-1.62e-4
	CFD	-4.66e-6	9.91e-3	-7.55e-3	-3.65e-5	2.54e-5	-2.08e-5	1.28e-4
	Difference	-4.75%	**12.90%**	**-14.15%**	-1.65%	0.51%	0.84%	2.61%
0.07	Model	6.05e-4	1.86e-2	-1.22e-2	4.91e-5	1.77e-5	2.59e-4	2.14e-4
	CFD	-7.03e-6	2.12e-2	-1.58e-2	-3.54e-5	3.32e-5	3.17e-4	-7.08e-5
	Difference	-2.70%	**11.18%**	**-15.88%**	-0.37%	0.07%	0.26%	-1.25%
0.17	Model min.	-5.33e-5	5.40e-2	-3.50e-2	-3.69e-5	-2.88e-4	2.40e-3	-5.54e-4
	Model mean	5.59e-4	5.47e-2	-3.38e-2	1.24e-4	-1.24e-4	2.65e-3	-3.51e-4
	Model max.	1.04e-3	5.51e-2	-3.26e-2	3.66e-4	5.72e-5	2.78e-3	-2.65e-4
	Repeatability	0.83%	0.85%	1.81%	0.31%	0.26%	0.28%	0.22%
	CFD	3.20e-5	**6.14e-2**	**-4.37e-2**	**-1.77e-4**	2.26e-5	**3.17e-3**	**3.21e-4**
	Difference	-0.80%	**10.22%**	**-15.16%**	**-0.46%**	0.22%	**0.80%**	**1.02%**

Table 4.27: Unsteady Pure Sway Fourier Coefficients of N', With Model Tests

$v'_{\max}$		C_0	$C_{1,C}$	$C_{1,S}$	$C_{2,C}$	$C_{2,S}$	$C_{3,C}$	$C_{3,S}$
0.03	Model	4.72e-4	5.46e-3	-1.07e-3	4.83e-5	-1.40e-5	1.64e-4	-3.59e-5
	CFD	-1.90e-5	6.79e-3	-1.05e-3	-1.85e-6	-4.31e-6	1.68e-5	-3.87e-5
	Difference	-7.86%	**21.35%**	0.25%	-0.80%	0.16%	-2.36%	-0.04%
0.07	Model	4.80e-4	1.13e-2	-1.96e-3	2.50e-5	5.07e-5	1.72e-4	-5.36e-5
	CFD	-1.40e-5	1.34e-2	-2.01e-3	8.64e-6	-1.60e-5	6.30e-5	-7.69e-5
	Difference	-4.07%	**17.48%**	-0.41%	-0.14%	-0.55%	-0.90%	-0.19%
0.17	Model min.	1.77e-4	2.96e-2	-4.68e-3	4.35e-5	-3.29e-5	8.18e-4	3.15e-4
	Model mean	5.21e-4	3.01e-2	-4.17e-3	1.09e-4	3.22e-5	8.86e-4	3.62e-4
	Model max.	7.21e-4	3.04e-2	-3.71e-3	1.82e-4	1.29e-4	9.81e-4	3.98e-4
	Repeatability	0.86%	1.20%	1.53%	0.22%	0.25%	0.26%	0.13%
	CFD	**-1.75e-5**	**3.37e-2**	-4.07e-3	9.22e-5	**-6.75e-5**	**3.80e-4**	**1.35e-4**
	Difference	**-1.69%**	**11.27%**	0.30%	-0.05%	**-0.31%**	**-1.59%**	**-0.72%**

Table 4.28: Values for normalizing unsteady pure drift Fourier coefficients

$v'_{\max}$	X'	Y'	N'
0.03	0.01741	0.01116	0.00624
0.07	0.01804	0.02266	0.01213
0.17	0.02152	0.06560	0.03176

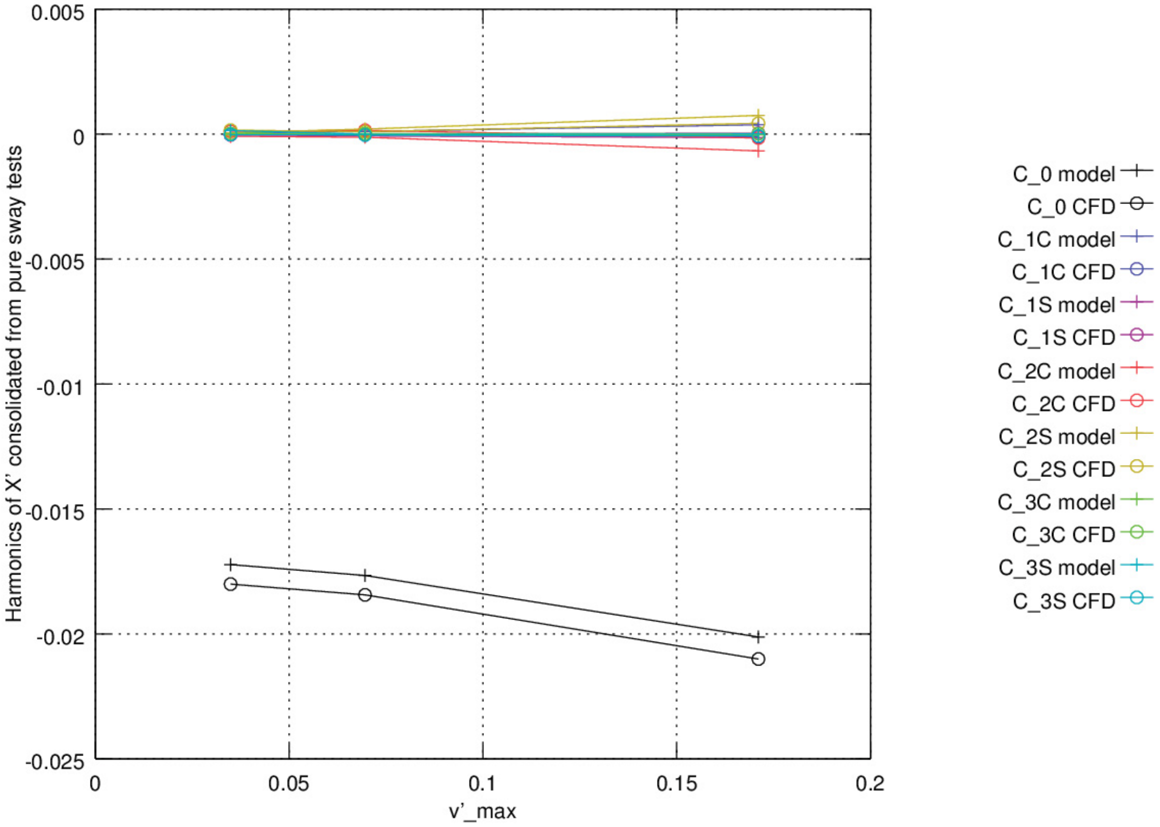

Figure 4.20: Unsteady pure sway Fourier coefficients of X', with model tests

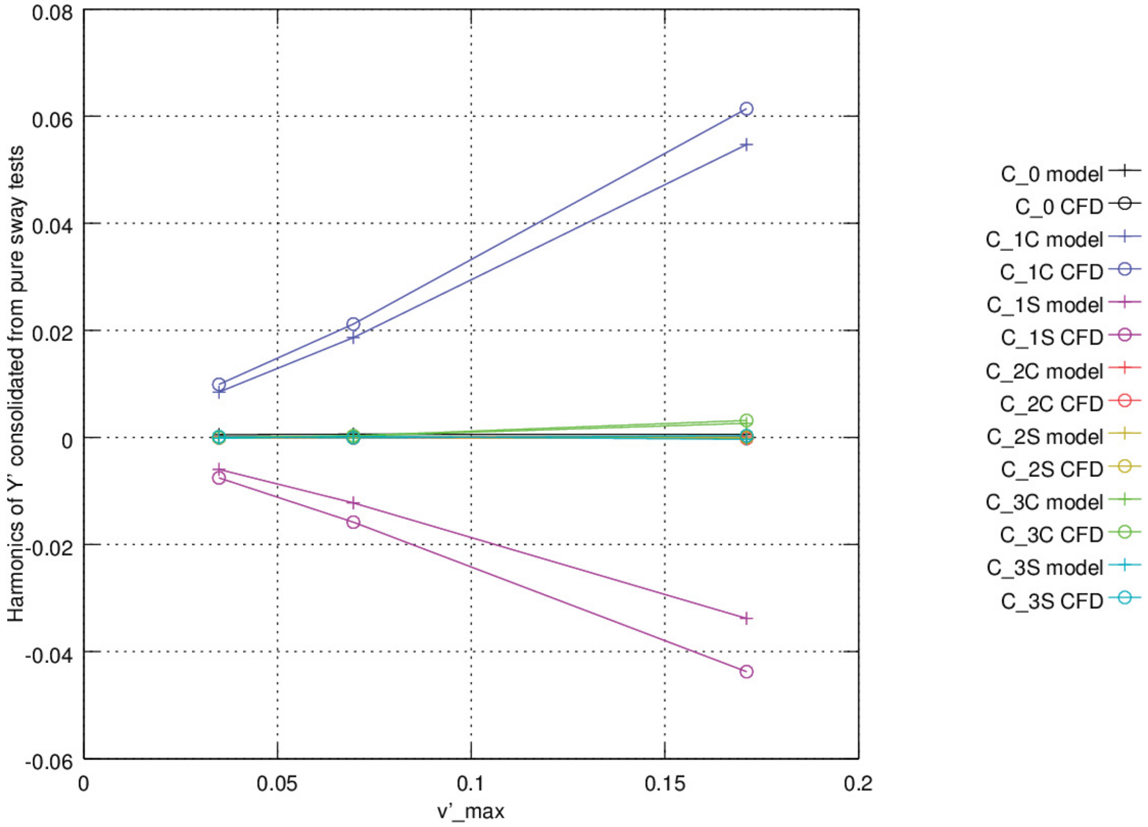

Figure 4.21: Unsteady pure sway Fourier coefficients of Y', with model tests

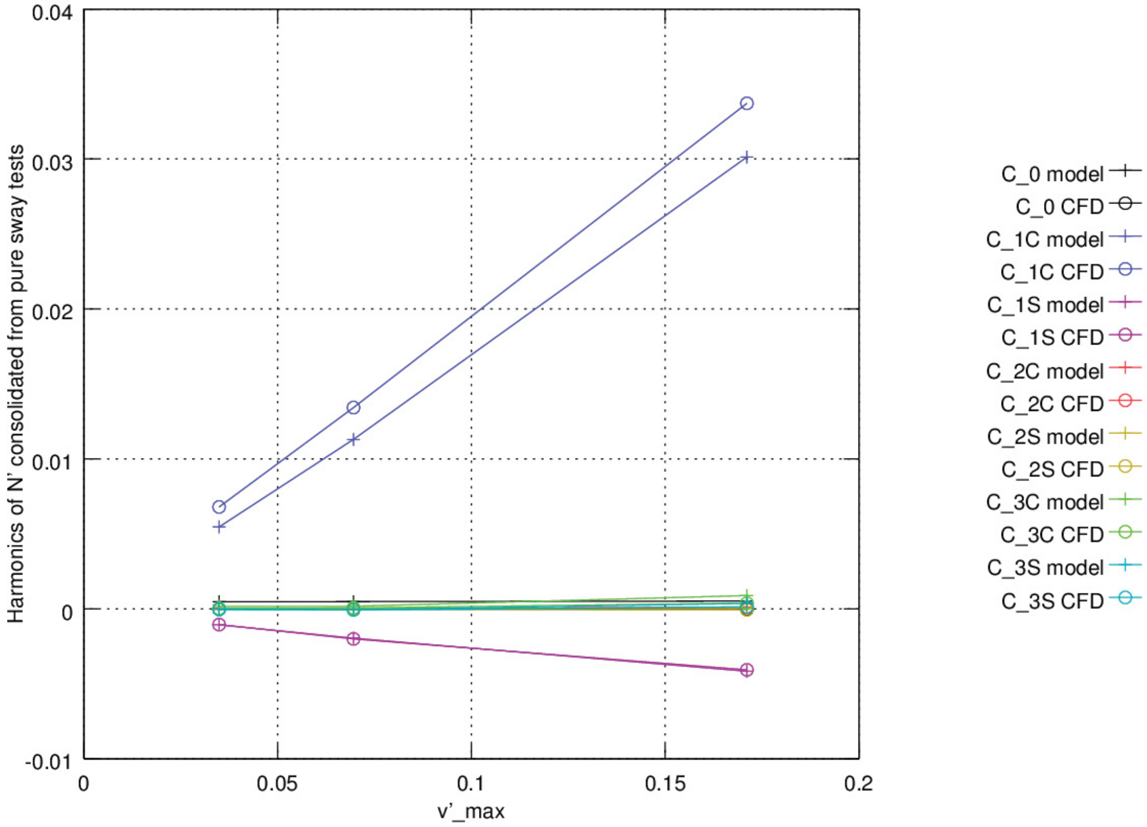

Figure 4.22: Unsteady pure sway Fourier coefficients of N', with model tests

4.5.2 Effect of Bilge Keels

Similar to the bilge keel study in the pure yaw test, only the mean value in the measured and computed X' can be used for the comparison purpose. Results indicate reduction of X' when bilge keel is removed; see Figure D.1.

In Figure D.2, the measured Y' includes significant high frequency oscillation, similar to the Y' in Figure C.2. When the bilge keel is removed, the profile of the Y' does not show a phase change but a change in the absolute magnitude of its maxima and minima. Thus, the phase change phenomenon in the profile of the Y' is due to the changes in vessel yaw rate.

The pattern of the changes in the profile of the N' in Figure D.3 is similar to the pattern in Figure C.3. Thus, the asymmetry in the changes to the profile of N' due to the removal of the bilge keel, in Figure B.6, is due to the effect of the static drift angle.

Table 4.29 shows the effect of bilge keels on the Fourier coefficients of each of the forces and moment. It shows that bilge keel removal in substantial modifications to only a small number of the Fourier coefficients, which are shown in bold in the table.

The relative differences have been normalized in accordance with Table 4.28.

Table 4.29: Bilge keel effect for unsteady pure sway; $v'_{\text{max}} = 0.03$

Result		C_0	$C_{1,C}$	$C_{1,S}$	$C_{2,C}$	$C_{2,S}$	$C_{3,C}$	$C_{3,S}$
X'	BK	-1.80e-2	-2.00e-5	-3.63e-5	1.04e-4	1.53e-4	2.21e-5	-3.15e-5
	No BK	-1.59e-2	-3.14e-5	-1.52e-6	1.28e-4	-8.93e-6	-4.70e-6	5.30e-6
	Difference	**12.12%**	-0.07%	0.20%	0.14%	-0.93%	-0.15%	0.21%
Y'	BK	-4.66e-6	9.91e-3	-7.55e-3	-3.65e-5	2.54e-5	-2.08e-5	1.28e-4
	No BK	1.52e-5	7.60e-3	-5.87e-3	-9.04e-6	-2.36e-5	1.58e-5	1.48e-5
	Difference	0.18%	**-20.73%**	**15.09%**	0.25%	-0.44%	0.33%	-1.02%
N'	BK	-1.90e-5	6.79e-3	-1.05e-3	-1.85e-6	-4.31e-6	1.68e-5	-3.87e-5
	No BK	-1.16e-5	6.05e-3	-8.72e-4	9.15e-6	-2.11e-6	3.57e-5	1.01e-5
	Difference	0.12%	**-11.87%**	2.88%	0.18%	0.04%	0.30%	0.78%

5 PREPROCESSING ERROR AND EFFECTS

5.1 IDENTIFICATION

It was determined late in the project, when the post-processing of the unsteady simulation results was essentially complete, that the draft and trim specified in the unsteady model set-up was incorrect. This includes the following two issues:

1. As described in Section 3.5, the process for setting the draft and trim involved two steps. First, the vessel was translated vertically so that at the draft at the AP was achieved. Then the vessel was rotated about the AP waterline to achieve the required draft at the FP. When completing the first step of this process, the FP draft was mistakenly used to determine the vertical translation distance. There is therefore a draft error equal to the difference between the FP draft and the AP draft.
2. All of the unsteady pure sway and pure yaw simulations (runs 1 through 9) used the same draft and trim as run 9 (unsteady pure yaw with $r'_{max} = 0.75$).

Table 5.1 provides the drafts and trim used in the CFD simulations, as well as the projected lateral area of the underwater hullform, A_L, and the longitudinal component of the centroid of this area, x_{AL}. The draft at the LCF (longitudinal centre of flotation) is based on the LCF in the even-keel condition at the still-water draft of 0.1736 m, as determined using Rhinoceros3D. A_L and x_{AL} are based on linear extrapolations from the projected underwater area of the even-keel condition at the still-water draft of 0.1736 m, considering an undisturbed waterline in the trimmed condition. Simulations completed without bilge keels are labeled with “NBK”; all simulations in the mesh refinement study used the same drafts as reported for Test 12. Table 5.2 provides the same data for the intended draft and trim inputs based on the model test results, and Table 5.3 provides a comparison of the two. Table 5.4 provides a similar comparison between the simulations with bilge keels and the corresponding simulations without bilge keels.

Table 5.1: Draft and Trim Used in Simulations

Test	AP draft	LCF draft	FP draft	Trim by bow	Trim by bow	A_L	x_{AL}
	[m]	[m]	[m]	[m]	[°]	[m²]	[m aft of FP]
1	0.1899	0.196	0.2030	0.0131	0.187	0.7421	1.7570
1 NBK	0.1899	0.196	0.2030	0.0131	0.187	0.7421	1.7570
2	0.1899	0.196	0.2030	0.0131	0.187	0.7421	1.7570
3	0.1899	0.196	0.2030	0.0131	0.187	0.7421	1.7570
4	0.1899	0.196	0.2030	0.0131	0.187	0.7421	1.7570
4 NBK	0.1794	0.179	0.1774	-0.0020	-0.029	0.6728	1.7612
5	0.1899	0.196	0.2030	0.0131	0.187	0.7421	1.7570
6	0.1899	0.196	0.2030	0.0131	0.187	0.7421	1.7570
7	0.1899	0.196	0.2030	0.0131	0.187	0.7421	1.7570
8	0.1899	0.196	0.2030	0.0131	0.187	0.7421	1.7570
9	0.1899	0.196	0.2030	0.0131	0.187	0.7421	1.7570
10	0.1896	0.195	0.2024	0.0128	0.183	0.7403	1.7570
11	0.1932	0.200	0.2091	0.0159	0.227	0.7602	1.7581
12	0.1906	0.196	0.2036	0.0130	0.186	0.7445	1.7580
12 NBK	0.1906	0.196	0.2036	0.0130	0.186	0.7445	1.7580

Table 5.2: Draft and Trim from Model Tests

Test	AP draft	LCF draft	FP draft	Trim by bow	Trim by bow	A_L	x_{AL}
	[m]	[m]	[m]	[m]	[°]	[m²]	[m aft of FP]
1	0.1782	0.180	0.1812	0.0030	0.043	0.6770	1.7528
2	0.1776	0.179	0.1802	0.0025	0.036	0.6738	1.7526
3	0.1784	0.181	0.1851	0.0067	0.096	0.6842	1.7486
4	0.1815	0.181	0.1794	-0.0020	-0.029	0.6809	1.7640
5	0.1802	0.183	0.1855	0.0053	0.076	0.6892	1.7530
6	0.1762	0.179	0.1817	0.0055	0.078	0.6733	1.7470
7	0.1795	0.183	0.1870	0.0075	0.107	0.6903	1.7494
8	0.1767	0.182	0.1876	0.0108	0.155	0.6851	1.7417
9	0.1768	0.183	0.1899	0.0131	0.187	0.6897	1.7394
10	0.1769	0.183	0.1896	0.0128	0.183	0.6892	1.7398
11	0.1773	0.184	0.1932	0.0159	0.227	0.6966	1.7371
12	0.1776	0.183	0.1906	0.0130	0.186	0.6925	1.7405

Table 5.3: Relative Difference in Draft and Trim

Test	AP draft	LCF draft	FP draft	Trim by bow	A_L	x_{AL}
	$[/T_m]$	$[/T_m]$	$[/T_m]$	$[/T_m]$	[/Model A_L]	$[/L_{BP}]$
1	6.7%	9.4%	12.6%	5.8%	9.6%	0.10%
2	7.1%	9.8%	13.2%	6.1%	10.1%	0.11%
3	6.7%	8.3%	10.3%	3.7%	8.5%	0.21%
4	4.9%	8.8%	13.6%	8.7%	9.0%	-0.18%
5	5.6%	7.6%	10.1%	4.5%	7.7%	0.10%
6	7.9%	9.9%	12.3%	4.4%	10.2%	0.25%
7	6.0%	7.5%	9.2%	3.2%	7.5%	0.19%
8	7.6%	8.2%	8.9%	1.3%	8.3%	0.38%
9	7.5%	7.5%	7.5%	0.0%	7.6%	0.44%
10	7.4%	7.4%	7.4%	0.0%	7.4%	0.43%
11	9.1%	9.1%	9.1%	0.0%	9.1%	0.53%
12	7.5%	7.5%	7.5%	0.0%	7.5%	0.44%

Table 5.4: Relative Difference in Draft and Trim, Without Bilge Keels

Test	AP draft	LCF draft	FP draft	Trim by bow	A_L	x_{AL}
	$[/T_m]$	$[/T_m]$	$[/T_m]$	$[/T_m]$	[/BK A_L]	$[/L_{BP}]$
1 NBK	0.0%	0.0%	0.0%	0.0%	0.0%	0.00%
4 NBK	-6.0%	-10.0%	-14.7%	-8.7%	-10.3%	0.11%
12 NBK	0.0%	0.0%	0.0%	0.0%	0.0%	0.00%

Table 5.3 shows that the differences are on the order of 7% to 11% for both LCF draft and projected area. This can be expected to result in increases in both of the manoeuvring forces and the yaw moment. The difference in x_{AL} is less than 0.53% of the L_{BP}; when compared to typical yaw moment arms on the order of $L_{BP}/2$ this suggests that errors in yaw moment will be driven more by the change in lateral area than by the longitudinal shift in its centroid.

Table 5.4 shows that Test 4 was simulated with different drafts with and without bilge keels. This resulted in a 10.3% difference in A_L, so it is likely that the bilge keel sensitivity presented for Test 4 in Section 4.4.2 is obscured by the effects of the changed draft and trim. However in tests 1 and 12, the same drafts were used both with and without bilge keels. It is therefore expected that for these tests the reported bilge keel sensitivity is reasonably representative of what would have been determined if the tests had been completed using the intended drafts.

5.2 EFFECT ON RESULTS

The magnitude of the effect on the results was investigated by repeating the simulation of the case used in the mesh refinement study, test 12, using the medium mesh. As the error was found very late in the analysis, time did not permit a full repeat of all affected cases, but the limited retesting did allow for estimation of the effect of the error on the full range of results.

The time-histories of the resulting X', Y', and N' are shown in Annex B; this includes both the raw results and the Fourier series fit to the results. The plots also include the model test data and the results of the mesh refinement study. When comparing the results with the corrected drafts to the original CFD results with the same medium mesh, it can be seen that for much of the PMM phase the corrected results are on the order of 10% smaller. This is in line with expectations based on the 7.5% change in A_L shown in Table 5.3 for test 12. Notable exceptions to this are:

1. Near 270° phase, the difference in X' reduces to about 5%;
2. Between about 340° and 40° phase (through 0°/360°), the Y' curves cross and the N' curves are nearly identical.

Notwithstanding the above observations, there is uncertainty in the effect of the draft correction, due to uncertainty in the CFD results. The difference due to the draft correction is at times greater than the difference between the medium- and fine-mesh solutions, while at other times the opposite is true.

It is similarly complicated to show whether the draft correction has improved the correlation with model test results: the agreement with model tests is sometimes better with the corrected drafts, and at other times is better with the drafts used in the original simulation.

The results of harmonic analysis of both the original medium-mesh simulation of test 12 and the corrected simulation of the same case are presented in Table 5.5 through Table 5.7. The values for the original simulation are slightly different than those presented in Section 4.3.3, which were based on the fine-mesh simulation.

As repeated model test runs were completed for this condition, it is of interest to compare the model test repeatability to the difference between CFD (with corrected drafts) and model test results. Cases where the CFD result does not fall within the range of the model test results, or where the percent difference is greater than the percent repeatability, are shown in bold. This shows about half of the X' Fourier coefficients predicted by CFD are within the repeatability of the model tests; closer inspection shows that none of those coefficients are far outside the model test repeatability range. Only one of the Fourier coefficients of each of Y' and N' are within the model test repeatability, and in some cases the difference between the CFD prediction and the mean model test result is substantially more than the model test repeatability. However, even in the cases where the difference between CFD and the mean model test result is greater than the model test uncertainty, the percent difference is at most 4.54%. As in Section 4.3.3, the relative differences have been normalized against the largest magnitude of response recorded in the model tests, shown in Table 4.18.

As the correction of the prescribed draft has removed a modelling error, it is expected that the correction would draw the simulation results closer to the model test results. The bottom row in each of Table 5.5 through Table 5.7 indicates whether the draft correction has improved the correlation with model tests; this is noted as unclear in cases where both CFD predictions are within the model test repeatability. For both forces and the moment, the accuracy of four of the seven Fourier coefficients was improved by the draft correction.

Decreased accuracy was found for the $C_{1,S}$ coefficient of X', Y', and N'; the C_0 coefficient of Y' and N', and the $C_{3,S}$ coefficient of N'.

Table 5.5: Effect of Drafts on Unsteady Yaw and 10° Drift X' Fourier Coefficients

Source		C_0	$C_{1,C}$	$C_{1,S}$	$C_{2,C}$	$C_{2,S}$	$C_{3,C}$	$C_{3,S}$
Model	min.	-2.19e-2	5.33e-4	-1.19e-3	5.81e-4	-2.00e-4	-2.99e-4	-1.80e-4
	mean	-2.16e-2	8.37e-4	-1.10e-3	6.83e-4	-3.96e-5	-1.79e-4	-5.43e-5
	max.	-2.08e-2	9.21e-4	-6.90e-4	8.07e-4	3.08e-4	1.54e-4	1.09e-4
	Repeat-ability	2.30%	0.82%	1.06%	0.48%	1.08%	0.96%	0.61%
CFD, original drafts	CFD	**-2.28e-2**	8.32e-4	**-1.23e-3**	**4.16e-4**	**-5.59e-4**	**-3.06e-4**	8.99e-5
	w.r.t. model	**5.16%**	0.02%	0.57%	**1.13%**	**2.21%**	0.54%	0.61%
CFD, corrected drafts	CFD	-2.09e-2	8.00e-4	**-6.24e-4**	6.47e-4	**-3.27e-4**	-2.40e-4	1.00e-4
	w.r.t. model	**2.67%**	0.16%	**2.02%**	0.15%	**1.22%**	0.26%	**0.66%**
	w.r.t. original drafts CFD	7.83%	0.13%	2.59%	0.98%	0.99%	0.28%	0.04%
	Improved?	Yes	Unclear	No	Yes	Yes	Yes	Unclear

Table 5.6: Effect of Drafts on Unsteady Yaw and 10° Drift Y' Fourier Coefficients

Source		C_0	$C_{1,C}$	$C_{1,S}$	$C_{2,C}$	$C_{2,S}$	$C_{3,C}$	$C_{3,S}$
Model	min.	6.66e-2	-9.45e-3	-3.06e-2	-7.46e-3	-1.60e-3	1.62e-3	-1.63e-4
	mean	6.83e-2	-8.52e-3	-3.01e-2	-7.04e-3	-1.13e-3	1.89e-3	9.86e-5
	max.	6.89e-2	-8.16e-3	-2.87e-2	-6.65e-3	-6.71e-4	2.10e-3	2.80e-4
	Repeat-ability	1.08%	0.61%	0.88%	0.38%	0.43%	0.22%	0.21%
CFD, original drafts	CFD	6.74e-2	**-1.09e-2**	**-2.78e-2**	**-8.02e-3**	-1.25e-3	**-5.48e-4**	**9.48e-4**
	w.r.t. model	0.82%	**2.19%**	**2.17%**	**0.92%**	0.11%	**2.28%**	**0.80%**
CFD, corrected drafts	CFD	**6.35e-2**	**-7.64e-3**	**-2.56e-2**	**-6.23e-3**	-8.46e-4	**6.95e-4**	**6.37e-4**
	w.r.t. model	**4.54%**	**0.82%**	**4.27%**	**0.76%**	0.26%	**1.12%**	**0.50%**
	w.r.t. original drafts CFD	3.72%	3.02%	2.10%	1.68%	0.38%	1.16%	0.29%
	Improved?	No	Yes	No	Yes	Unclear	Yes	Yes

Table 5.7: Effect of Drafts on Unsteady Yaw and 10° Drift N' Fourier Coefficients

Source		C_0	$C_{1,C}$	$C_{1,S}$	$C_{2,C}$	$C_{2,S}$	$C_{3,C}$	$C_{3,S}$
Model	min.	3.22e-2	-5.14e-3	-2.03e-2	-1.50e-3	-2.30e-5	2.40e-4	3.80e-4
	mean	3.27e-2	-4.94e-3	-2.01e-2	-1.32e-3	1.09e-4	3.15e-4	4.91e-4
	max.	3.29e-2	-4.74e-3	-1.95e-2	-1.09e-3	2.56e-4	3.90e-4	5.68e-4
	Repeat-ability	0.66%	0.35%	0.80%	0.37%	0.25%	0.14%	0.17%
CFD, original drafts	CFD	**3.38e-2**	**-6.65e-3**	-1.99e-2	**-1.87e-3**	**3.53e-4**	**-4.83e-5**	**3.43e-4**
	w.r.t. model	**1.95%**	**3.09%**	0.37%	**0.99%**	**0.44%**	**0.66%**	**0.27%**
CFD, corrected drafts	CFD	**3.12e-2**	-4.99e-3	**-1.85e-2**	**-1.03e-3**	**2.99e-4**	3.53e-4	**3.22e-4**
	w.r.t. model	**2.76%**	0.10%	**2.95%**	**0.52%**	**0.34%**	0.07%	**0.31%**
	w.r.t. original drafts CFD	4.72%	2.99%	2.58%	1.51%	0.10%	0.73%	0.04%
	Improved?	No	Yes	No	Yes	Yes	Yes	No

5.3 VERIFICATION

To verify the prescribed draft and trim, the vertical force and the pitching moment due to the fluid pressure and shear stress on the hull have been determined by STAR-CCM+. These have been post-processed by adding the weight of the vessel to determine the net force and moment; this has been translated to determine the net force and moment acting about the longitudinal centre of flotation (LCF). Using linear hydrostatics with the waterplane area and the longitudinal metacentric height, the draft change and trim change (about the LCF) that would be required to achieve a force and moment balance has been predicted. Table 5.8 shows the results of this for all of the steady and (as averaged over a motion period) unsteady simulations. It shows that the CFD predictions very nearly achieve a vertical force and trimming moment balance in all cases where the intended draft and trim have been correctly applied. It also shows that the revised simulation of run 12 with a corrected draft has reduced the additional draft required from -10.72 mm to 1.61 mm.

Future applications of CFD maneuvering simulation may include vessel designs for which there are no model test data upon which to base the prescribed draft and trim. In addition, Table 5.5 through Table 5.7 show that the influence of draft and trim is important to achieving the demonstrated level of accuracy of the CFD predictions. The ability of CFD to accurately determine the draft and trim is therefore critical to the analysis of untested designs. While the full process of CFD draft and trim prediction is outside the scope of this project, the results in Table 5.8 provide an encouraging indication that relatively accurate draft and trim predictions could be achieved.

Table 5.8: Verification of Prescribed Draft and Trim

Test type	Test parameters	Additional draft required [mm]	Additional trim by stern required [°]
Steady drift	$\beta = 0°$	0.94	-0.0173
	$\beta = 2°$	-0.01	-0.0129
	$\beta = 6°$	-0.20	-0.0151
	$\beta = 9°$	1.59	-0.0260
	$\beta = 11°$	1.57	-0.0228
	$\beta = 12°$	0.90	-0.0204
	$\beta = 16°$	1.38	-0.0244
	$\beta = 20°$	0.65	-0.0280
	$\beta = 10°$, Coarse mesh	1.21	-0.0150
	$\beta = 10°$, Medium mesh	1.04	-0.0142
	$\beta = 10°$, Fine mesh	0.97	-0.0154
	$\beta = 10°$, NBK	0.89	-0.0161
Unsteady pure sway	Run 1: $v'_{max} = 0.03$	-14.86	0.0134
	Run 1: $v'_{max} = 0.03$, no BK	-1.63	-0.0110
	Run 2: $v'_{max} = 0.07$	-14.50	0.0135
	Run 3: $v'_{max} = 0.17$	-12.24	0.0095
Unsteady pure yaw	Run 4: $r'_{max} = 0.05$	-14.99	0.0127
	Run 4: $r'_{max} = 0.05$, no BK	2.18	-0.0222
	Run 5: $r'_{max} = 0.15$	-14.78	0.0131
	Run 6: $r'_{max} = 0.30$	-14.15	0.0128
	Run 7: $r'_{max} = 0.45$	-13.20	0.0109
	Run 8: $r'_{max} = 0.60$	-12.08	0.0081
	Run 9: $r'_{max} = 0.60$	-10.68	0.0042
Unsteady yaw and drift	Run 0: $\beta = 9°$	-10.40	-0.0020
	Run 11: $\beta = 11°$	-13.75	-0.0005
	Run 12: $\beta = 10°$, Fine mesh	-10.81	-0.0041
	Run 12: $\beta = 10°$, Medium mesh	-10.72	-0.0043
	Run 12: $\beta = 10°$, Coarse mesh	-10.65	-0.0043
	Run 12: $\beta = 10°$, no BK	-10.93	-0.0056
	Run 12: $\beta = 10°$, corrected drafts	1.61	-0.0062

5.4 SUMMARY

The draft and trim error do not significantly affect any conclusions related to modelling approaches, such as the selection of time step, the cyclic repeatability, the effects of mesh refinement, and the spatial discretization error calculation. The conclusions regarding the influence of bilge keels are not be significantly influenced for cases 1 and 12, where the same draft and trim were used both with and without bilge keels.

Repeating the simulation of case 12 with corrected drafts generally improved the results, with the exception of 6 of the 21 Fourier coefficients, for which the difference from the mean model test result was increased and outside the range of model test repeatability.

The net vertical force and net pitching moment (in simulations using the intended drafts) are quite small. This is encouraging because future efforts where model tests may not be available would require that CFD predict the draft and trim, and the present results suggest this could be done with reasonable accuracy.

It is anticipated that the comparison with model tests could be further improved by using time-varying draft and trim for the unsteady simulations, and this is recommended for future work.

It is recommended that additional repeat analyses be carried out to extend this impact analysis of the draft error. For example, the pure sway test 3 and the pure yaw test 6 both include multiple repeat model tests, so would be good candidates for exploring the impact on the different types of unsteady tests.

6 CONCLUSION

6.1 SUMMARY

STX Canada Marine have completed CFD simulations to numerically replicate Planar Motion Mechanism (PMM) model tests of the DDG51 frigate, previously completed by FORCE Technology [1, 2] in the context of the SIMMAN workshops. The aim of the present study was to validate both the accuracy and practicality of CFD for the prediction of ship manoeuvring data that can be derived from PMM tests. The scope of the validation is limited to the relatively direct results of the PMM tests or simulations: it does not include the development of manoeuvring derivatives and using them in a mathematical manoeuvring simulation to predict IMO or other ship manoeuvres.

The vessel has a relatively typical fine hullform for a fast displacement naval monohull, and includes both a sonar bulb (below baseline) and bilge keels. No rudder, propellers, shafts, or other appendages were included in either the model tests or the CFD simulations.

Most of the model tests completed at a Froude number of 0.28 were repeated with CFD. The simulations include cases of steady drift, unsteady pure sway, unsteady pure yaw, and the combination of unsteady pure yaw with a superimposed steady drift angle. To establish the spatial discretization error as presented for the Journal of Fluids Engineering [3], mesh refinement studies including three mesh sizes were completed for one steady case and one unsteady case. The sensitivity of the results to the bilge keels was investigated by repeating four of the simulations with the bilge keels removed. All simulations have been completed with the intent of carefully replicating the model tests. Details such as the vessel geometry, model scale, physical constants, and equations describing the PMM motion were kept consistent with [1]. The results analysis focused on the non-dimensional forces and moment of most interest to ship manoeuvring: the longitudinal force, X', the lateral force, Y', and the yaw moment about amidships, N'.

A literature review was completed prior to initiating the simulation work. The relatively few studies found showed a variety of techniques, and some presented relatively good correlation with experimental results for steady simulations. Good validation of unsteady manoeuvring simulations was not found. The review provided some insight into the effectiveness of different CFD modelling techniques and details, in the context of vessel manoeuvring simulations.

While the model test report [1] included a detailed error analysis, some of the final plots showed a drastic difference from the separately presented raw results from the same tests [2]. It was determined that the error was likely in the model test report [1]; due to this error it could not be assumed that the uncertainty results (shown on the same plots) were correct. This unfortunately limited the consideration for experimental uncertainty to examining the range of results obtained for the few test conditions in which twelve repeat runs were completed.

At higher drift angles, the steady drift solutions exhibited a breaking bow wave on the upstream side, a breaking wave near amidships on the downstream side, and flow aeration downstream which was drawn under the hull. These flow patterns are unsteady and have too small of a length and timescale to be fully resolved by the simulations. It was also found that the fluctuations in the integrated hull forces and moment were small, and so it was inferred that resolving these flow phenomena accurately is not important to the accuracy of the time-averaged forces and moment. A large vortex shed from the sonar bulb was prominent in the solution. At some drift angles this vortex extended underneath the downstream bilge keel and modified the flow so that the transverse component of the flow velocity across the bilge keel tip was in the opposite direction to the overall drift velocity. This type of flow interaction would not have been captured by classical simple manoeuvring techniques which treat the hull and bilge keel manoeuvring forces separately.

While the above fluctuations in the steady drift results were small, so was the difference between the results achieved with the coarse, medium, and fine meshes. Therefore the calculation of the spatial discretization error was somewhat obscured. The fine-mesh spatial discretization error was determined to be between 0.0004% and 0.14% for X', between 0.26% and 3.0% for Y', and between 0.70% and 1.6% for N'.

For drift angles of 2° or greater, the comparison of the steady drift simulations with model test results showed at most 7.3% error for X', 4.4% error for Y', and 5.4% for N'. With the fine mesh at 10° drift, there were also 12 repeated model tests, and the errors were reduced to 0.9% for X', 2.9% for Y', and 2.6% for N'.

The removal of bilge keels in the 10° drift case resulted in an 11% reduction in X', an 8% reduction in Y', and 1.4% reduction in N'. With bilge keels, the well-established bilge keel vortex merged with the weaker skeg vortex; without bilge keels the skeg vortex remained distinct from other flow features.

The unsteady simulations exhibited similar types of flow phenomena to those found in the steady simulations. In addition, the animations show additional transverse waves having small amplitudes and short wavelengths, which are overtaken by the vessel. These could be either a real physical phenomena or a numerical artifact. Refinement in both time and space would be required to either better resolve either the phenomena or remove the artifact. In either case, it was determined that effects of the small flow pattern on the overall manoeuvring forces and moment are not important.

The post-processing of the unsteady simulations included harmonic analysis of the time-series results to yield the coefficients of a third-order Fourier series for X', Y', and N'. These coefficients are viewed as an intermediary which captures the aspects of the raw time series that would capture the essential manoeuvring characteristics of the vessel, without deriving a mathematical manoeuvring model derived from the CFD results and thereby obtaining final results such as a tactical diameter or zig-zag overshoot. Percentage differences or errors reported for the unsteady results are generally on the basis of Fourier coefficient, normalized by the maximum amplitude of the mean model test time-history so that relatively unimportant Fourier coefficients are not over-emphasized.

Late in the project, when the post-processing of all simulations was effectively complete, it was found that the draft and trim were incorrectly specified in the setup of all unsteady simulations. These have been interpreted as errors in the projected underwater lateral area of 7% to 11%, and errors in the longitudinal centroid of this area of less than 0.53% of the length between perpendiculars. The case used for the mesh refinement study was repeated with corrected drafts and the medium mesh to assess the impact of the erroneous inputs. It was found that the predictions were generally improved by this, although the accuracy (as compared to model tests) was decreased for about a quarter of the results. The difference between the results of the corrected simulation and the mean of the 12 repeat model tests, as determined from the Fourier coefficients, was found to be at most 2.67% for X', 4.54% for Y', and 2.95% for N'.

Despite the above draft and trim error, the unsteady mesh refinement study is still considered to be generally applicable, because the same draft and trim were used on all three meshes. It showed a fine-mesh spatial discretization error of at most 4.80% for X', 0.75% for Y', and 4.75% for N'. For Y', the mesh convergence appeared to be divergent for some Fourier coefficients; this is expected to be a misinterpretation of oscillatory convergence, and would be clarified by repeating the simulation with a yet finer mesh.

Although the unsteady simulations are subject to draft and trim input errors, the difference from the model test Fourier coefficients of the dynamic yaw and drift tests is at most 10.61% for X', 8.43% for Y', and 8.93% for N'. The greatest difference from model test Fourier coefficients for the pure yaw tests (not including the outlier model test at $r'_{\max} = 0.15$) is 5.28% for X', 33.50% for Y', and 17.28% for N'. The greatest difference from model test Fourier coefficients for the pure sway tests is 4.49% for X', 15.88% for Y', and 21.35% for N'. The most different Fourier coefficient for an individual test is typically between 5% and 20% different from the model test result.

While the simulations with bilge keels removed did not use the intended drafts, the unsteady pure sway case and the unsteady yaw and drift case both used the same drafts with and without bilge keels. The observed bilge keel effect for those is therefore reasonably representative of what would have been observed with the correct drafts. For the unsteady pure sway case, bilge keel removal resulted in a 12% reduction in X', a 21% reduction in Y', and a 12% reduction in N'.

For the unsteady yaw and drift case, bilge keel removal resulted in an 8% reduction in X', a 9.5% change in Y' which visually appeared as a phase change, and a 0.8% change in N'.

Overall, this study has shown validation results which support the accuracy and feasibility of CFD as an early analysis tool for determining the manoeuvring characteristics of a vessel. The accuracy of the steady simulations, as judged by comparisons to model tests, is almost as good as the repeatability of the model tests themselves. This represents a substantial improvement over other studies identified in the literature review, which reported errors in the order of 10% for steady drift cases, and unacceptably large errors for unsteady cases.

6.2 RECOMMENDATIONS FOR FUTURE WORK

Considering that the ship manoeuvring performance is a relatively new application for CFD, there are many opportunities for further work. A number of these are listed below, but this list is by no means exhaustive. The first two recommendations could be undertaken without any additional CFD analysis, while the remainder would all extend the CFD work undertaken in this study.

1. The uncertainty analysis in the model test report [1] should be corrected, including the obvious errors in the final plots, and scrutiny of the remainder of the calculations and results. This would also ideally include synthesis with other model tests of the same vessel carried out in the SIMMAN workshop series, to better establish the experimental uncertainty and mean result. Upon completion of this,

the comparison with the present CFD results and the model test results could be revisited to improve the quality of the validation. This may be best pursued via the SIMMAN workshops.

2. The CFD results could be used to formulate a mathematical manoeuvring model, and the resulting model should be used to predict realistic ship manoeuvres typical of those used for assessing manoeuvring design criteria. Following this insight into the uncertainty in the salient results of the manoeuvres and their relationship to the CFD modelling fidelity should be sought through a sensitivity analysis. Such insight is of utmost importance to the overall reliability of the technique from the designer's perspective.
3. Some or all of the unsteady simulations presented herein could be repeated with the draft and trim corrected to extend the impact analysis of the draft error presented in Section 5.2. For example, the pure sway test 3 and the pure yaw test 6 both include multiple repeat model tests, so would be good candidates for exploring the impact on the different types of unsteady tests.
4. Simulations with an even finer mesh and time step could be completed to more formally support the conclusion that the small scale flow observed in the present simulations are not of importance to the integrated hull forces and moment.
5. Validation could be carried out to establish the ability to use CFD to predict the sinkage and trim of the vessel during the manoeuvring simulations. This is an important precursor to the use of CFD for designs which have not yet been model tested.
6. CFD validation could be carried out for a model including other appendages, and notably a rudder and/or propeller. This would allow the hydrodynamic interaction with these appendages and the main flow around the hull to be included in the subsequent development of a mathematical manoeuvring model.
7. Validation could be carried out to establish the ability and practicality of using CFD to also predict vessel roll motions in manoeuvring simulations.
8. Alternative test conditions could be explored with the aim of determining how CFD can most efficiently predict the necessary data to establish a vessel's manoeuvring performance characteristics. In particular, this need not be bound by the physical limitations that have guided the development of present experimental techniques. For example, while rotating arm model test facilities are scarce (thereby favouring PMM tests), a comparable CFD simulation of a steady drift angle and steady yaw rate could yield some of the same information as a PMM test – but could be completed with the relative simplicity of a steady simulation.
9. The validation of CFD for vessel manoeuvring could be expanded to include other vessels. In particular, the flow on the DDG51 Frigate typically included a large vortex shed of the sonar bulb. The validation results may therefore be different even in the case of a vessel without such a bulb, but with an otherwise similar hullform (e.g. the CPF). The validation of the method for other vessel types is considered to be a necessary precursor to its use for predicting the manoeuvring characteristics of new designs.

10. While a full-scale CFD simulation of a vessel is more computationally intensive, it could provide a valuable tool for overcoming some of the scale-related deficiencies of model tests. It would be valuable to compare model-scale and full-scale CFD simulations to explore scale effects. Also, it would be ideal to validate full-scale CFD simulations against full-scale manoeuvring trials data, if they are available.
11. The literature review found some instances of using CFD to directly predict entire free-running manoeuvres. The practicality and validation of such a technique could be investigated and weighed against the present approach of simulating captive tests to construct a Taylor series-based mathematical manoeuvring model.

7 REFERENCES

[1] Claus D. Simonsen, "PMM model test with DDG51 including uncertainty assessment," Force Technology, ONRII187 01, 2004.

[2] Kristian Agdrup, FORCE Technology, "Model Test Report, PMM tests of Hull 5415 with bilge keels only," 2004. [Online]. Available: SIMMAN 2014 FTP site.

[3] Ismail B. Celik, Urmila Ghia, Patrick J. Roache and Christopher J. Freitas, "Procedure for Estimation and Reporting of Uncertainty Due to Discretization in CFD Applications," *Journal of Fluids Engineering,* vol. 130, no. 7, p. 078001, 2008.

[4] Claus D. Simonsen, Janne F. Otzen, Christian Klimt, Nikolaj L. Larsen, Frederick Stern, "Maneuvering predictions in the early design phase using CFD generated PMM data," in *29th Symposium on Naval Hydrodynamics*, Gothenburg, Sweden, August 2012.

[5] "Workshop on Verification and Validation of Ship Manoeuvering Simulation Methods," in *SIMMAN 2008*, Copenhagen, April 2008.

[6] Nobuaki Sakamoto, Pablo M. Carrica, Frederick Stern, "URANS simulations of static and dynamic maneuvering for surface combatant: part 1. Verification and validation for forces, moment, and hydrodynamic derivatives," *J Mar Sci Technol,* vol. 17, pp. 422-445, 2012.

[7] E. Jacquin, P.-E. Guillerm, A. Drouet, P. Perdon, B. Alessandrini, "Simulation of unsteady ship maneuvering using free-surface RANS solver," in *26th Symposium on Naval Hydrodynamics*, Rome, Italy, September 2006.

[8] "Rhinoceros," [Online]. Available: http://www.rhino3d.com/. [Accessed 14 Dec 2013].

[9] "FORAN," SENER Marine, [Online]. Available: http://www.foransystem.com/NAVAL/home/en. [Accessed 14 Dec 2013].

[10] "FORMSYS," Bently Sustaining Infrastructure, [Online]. Available: http://www.formsys.com/maxsurf. [Accessed 14 Dec 2013].

[11] "ShipConstructor," SSI Corporate, [Online]. Available: http://www.ssi-corporate.com/. [Accessed 14 Dec 2013].

[12] Lu Zou, Lars Larsson, Michal Orych, "Verification and validation of CFD predictions for a manoeuvring tanker," in *9th International Conference on Hydrodynamics*, Shanghai, 2010.

[13] Pablo M. Carrica, Farzad Ismail, Mark Hyman, Shanti Bhushan, Frederick Stern, "Turn and zigzag maneuvers of a surface combatant using a URANS approach with dynamic overset grids," *J Mar Sci Technol,* vol. 18, pp. 166-181, 2013.

[14] "CD-adapco training course: Virtual Tow Tank," CD-adapco, 2012.

[15] "ITTC - Recommended Procedures and Guidelines: Guideline on Use of RANS Tools for Manoeuvering Prediction," 26th ITTC Manoeuvering Committee, 7.5-03 (04-01), 2011.

[16] Frederick Stern, "The Current Status of CFD in ITTC 2: Maneuvering & Seakeeping," ITTC, Fukuoka, 2008.

[17] Nobuaki Sakamoto, "URANS And DES Simulations Of Static And Dynamic Maneuvering For Surface Combatant," University of Iowa, Iowa, 2009.

[18] Menter, F. R., "Two-Equation Eddy-Viscosity Turbulence Models for Engineering Applications," *AIAA Journal,* vol. 32, no. 8, pp. 1598-1605, 1994.

[19] "Eulerian Multiphase," CD-Adapco, [Online]. Available: http://www.cd-adapco.com/products/star-ccm%E2%84%A2/%E6%AC%A7%E6%8B%89%E5%A4%9A%E7%9B%B8%E6%B5%81. [Accessed 18 Dec 2013].

[20] "ANSYS Fluent Features: Multiphase Flow," ANSYS, [Online]. Available: http://www.ansys.com/Products/Simulation+Technology/Fluid+Dynamics/Fluid+Dynamics+Products/ANSYS+Fluent/Features. [Accessed 18 Dec 2013].

[21] B.E. Launder and D.B. Spalding, "The numerical computation of turbulent flows," *Comp. Methods Appl. Mech. Eng.,* vol. 3, pp. 269-289, 1974.

[22] Choi, Junwoo and Yoon, Sung Bum, "Numerical simulations using momentum source wave-maker applied to RANS equation model," *Coastal Engineering,* vol. 56, no. 10, p. 1043 – 1060, 2009.

[23] "SIMMAN 2014," Force Technology, [Online]. Available: http://www.simman2014.dk/cms/site.aspx?p=13337. [Accessed 29 Jan 2014].

[24] L. Benedetti, B. Bouscasse, R. Broglia, L. Fabbri, F. La Gala, C. Lugni, "PMM ModelL Test With DDG51 Including Uncertainty Assessment; No 14," INSEAN, Prepared for SIMMAN 2007.

APPENDICES

APPENDIX A. DATA STRUCTURE IN HARD DRIVE

A hard drive is attached to this report where inputs to STAR-CCM+, outputs from STAR-CCM+, and the post-processed data are presented. The data structure in the hard drive consists of several folders and subfolders as:

1. Std Drift *[referring to the steady drift tests]*
    1.1. in 0d to in 20d *[referring to the tests at different drift angles in* Table 3.1*]*
    1.2. MRS *[referring to the mesh refinement study]*
        1.2.1. C *[referring to the coarse mesh data]*
        1.2.2. F *[referring to the fine mesh data]*
        1.2.3. M *[referring to the medium mesh data]*
    1.3. NBK *[referring to the case with no bilge keel]*
    1.4. Setup *[referring to the simulations done during problem setup]*
2. Ustd Yaw-Drift *[referring to the unsteady yaw and drift tests]*
    2.1. C and M mesh, and Exp. Data *[referring to comparison of the results from coarse and medium meshes]*
    2.2. *Cyclic and Time Accuracy [referring to the tests where cyclic repeatability and temporal accuracy of the solutions are investigated]*
    2.3. MRS *[referring to the mesh refinement study]*
    2.4. R10 to R12 *[referring to the tests 10 to 12 in* Table 3.2*]*
    2.5. R12NBK *[referring to the run which is similar to R12 but with no bilge keel]*
    2.6. Setup *[referring to the simulations done during problem setup]*
3. Ustd Yaw *[referring to the unsteady yaw tests]*
    3.1. R04 to R09 *[referring to the tests 04 to 09 in* Table 3.3*]*
    3.2. R04NBK *[referring to the run which is similar to R04 but with no bilge keel]*
    3.3. Setup *[referring to the simulations done during problem setup]*
4. Ustd Sway *[referring to the unsteady sway tests]*
    4.1. R01 to R03 *[referring to the tests 01 to 03 in* Table 3.4*]*
    4.2. R01NBK *[referring to the run which is similar to R01 but with no bilge keel]*

The leaf level in the above-presented hierarchy where the tests in Table 3.1 to Table 3.4 are presented is a folder which includes the following folders:

- 3D *[referring to STAR_VIEW files which permit 3D view of a scene]*
- Csv *[referring to the *.csv outputs from STAR-CCM+]*
- Plt *[referring to the plots which are a direct output from STAR-CCM+]*
- Sne *[referring to the hard copy of scenes as a direct output from STAR_CCM+]*
- *Avi [Only in unsteady tests: referring to the animations generated from the scenes and plots which were output from STAR-CCM+]*
- *PostProcessing [referring to plots which include both the CFD and model test time-histories; both the raw results and the Fourier representations of the results are shown]*

These sub-folders are also available in the folders presenting the mesh refinement and the bilge keel studies.

APPENDIX B. UNSTEADY YAW AND DRIFT

Mesh Refinement Study:

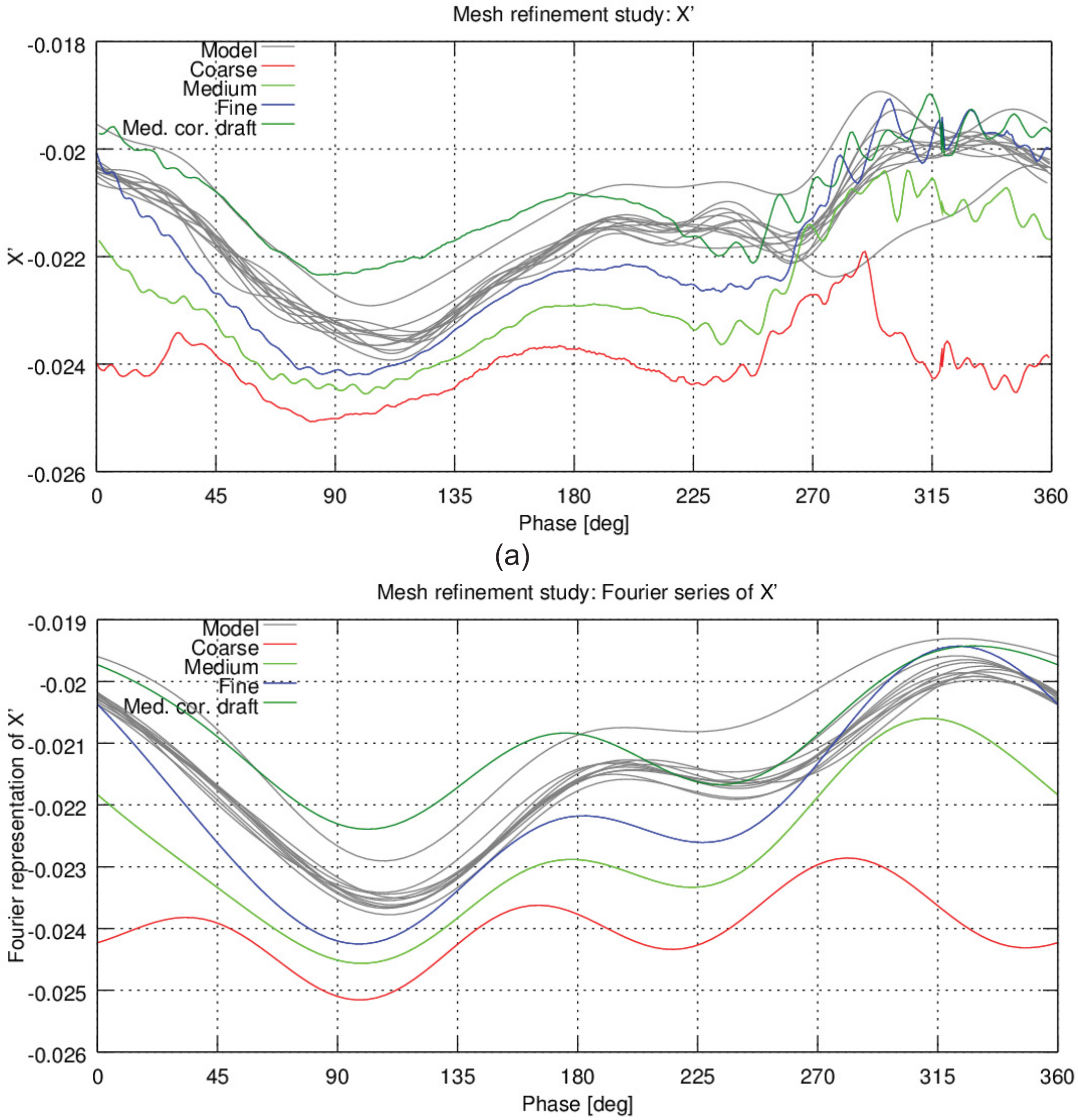

(a)

(b)

Figure B.1: Measured and Computed X' in Mesh Refinement Study for Yaw and Drift Test; (a) Pure Measured/Computed Data, (b) Fourier Representation of Data

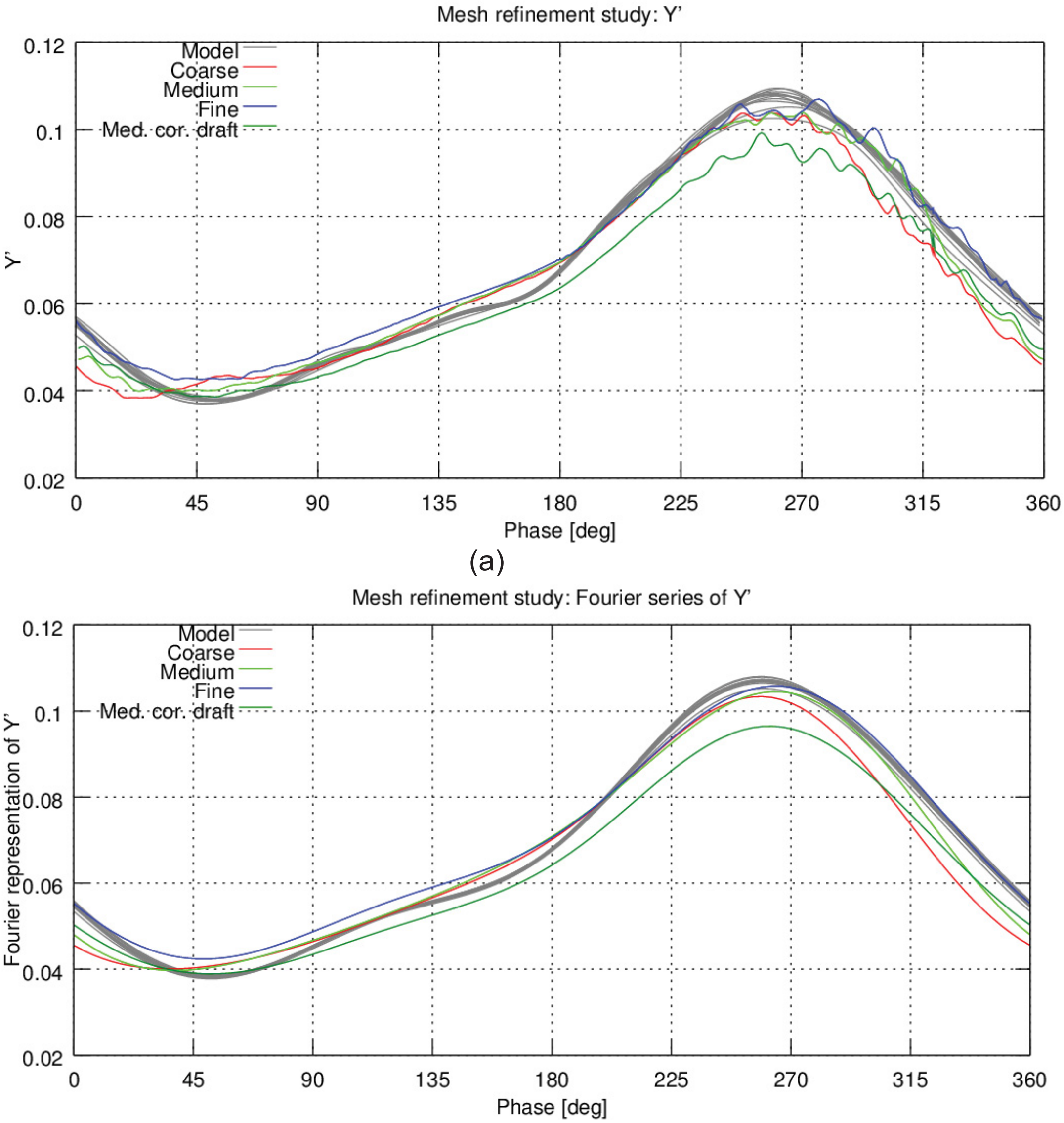

(a)

(b)

Figure B.2: Measured and Computed Y' in Mesh Refinement Study for Yaw and Drift Test; (a) Pure Measured/Computed Data, (b) Fourier Representation of Data

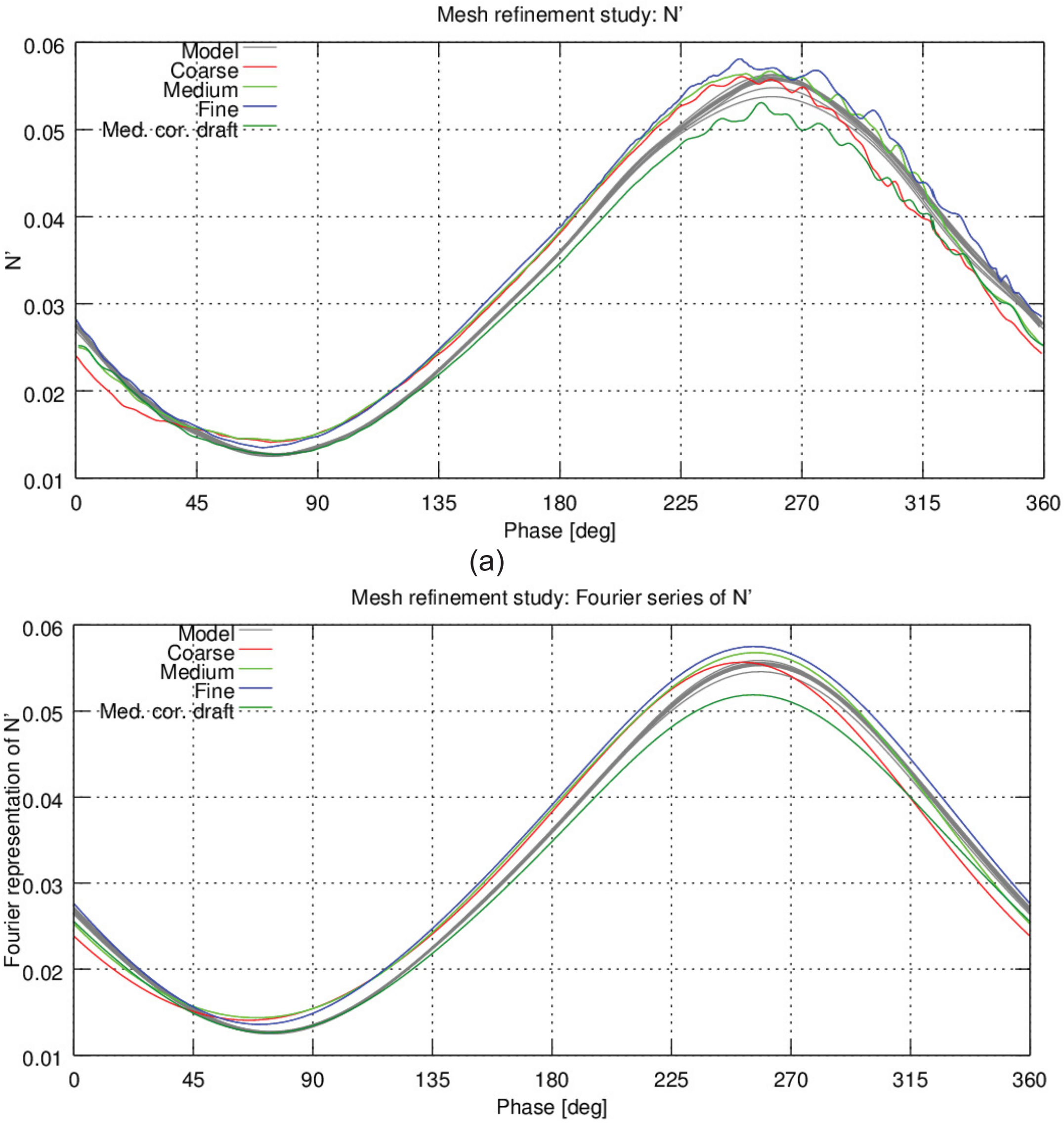

(a)

(b)

Figure B.3: Measured and Computed Z' in Mesh Refinement Study for Yaw and Drift Test; (a) Pure Measured/Computed Data, (b) Fourier Representation of Data

Effect of Bilge Keels

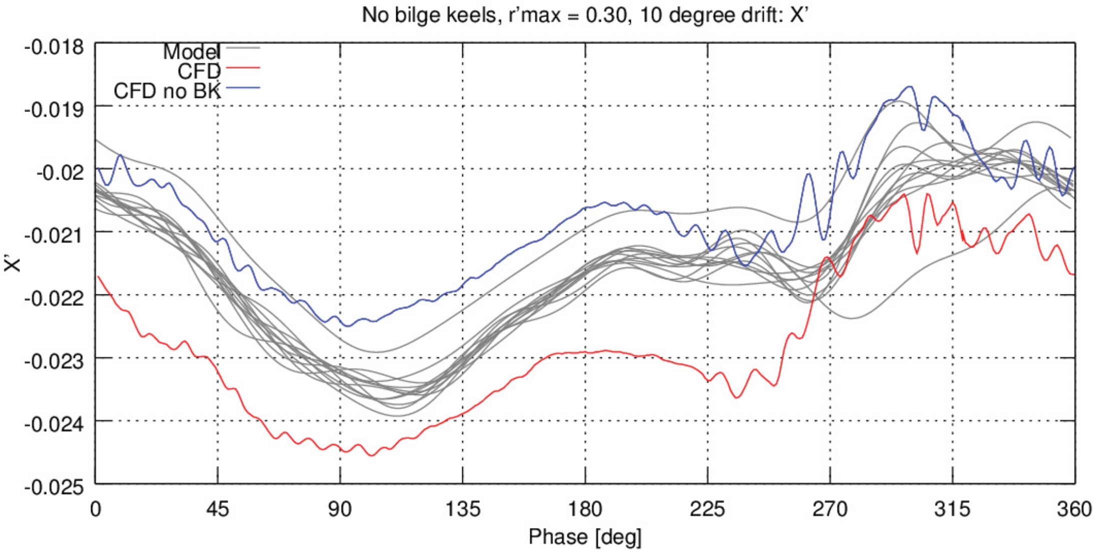

(a)

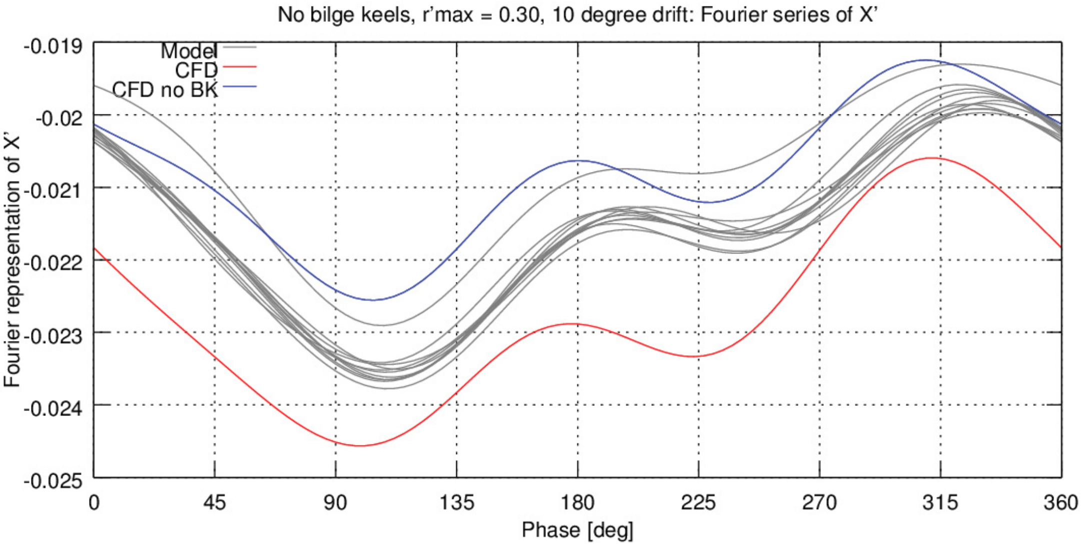

(b)

Figure B.4: Measured and Computed X' in Bilge Keel Study for Yaw and Drift Test; (a) Pure Measured/Computed Data, (b) Fourier Representation of Data

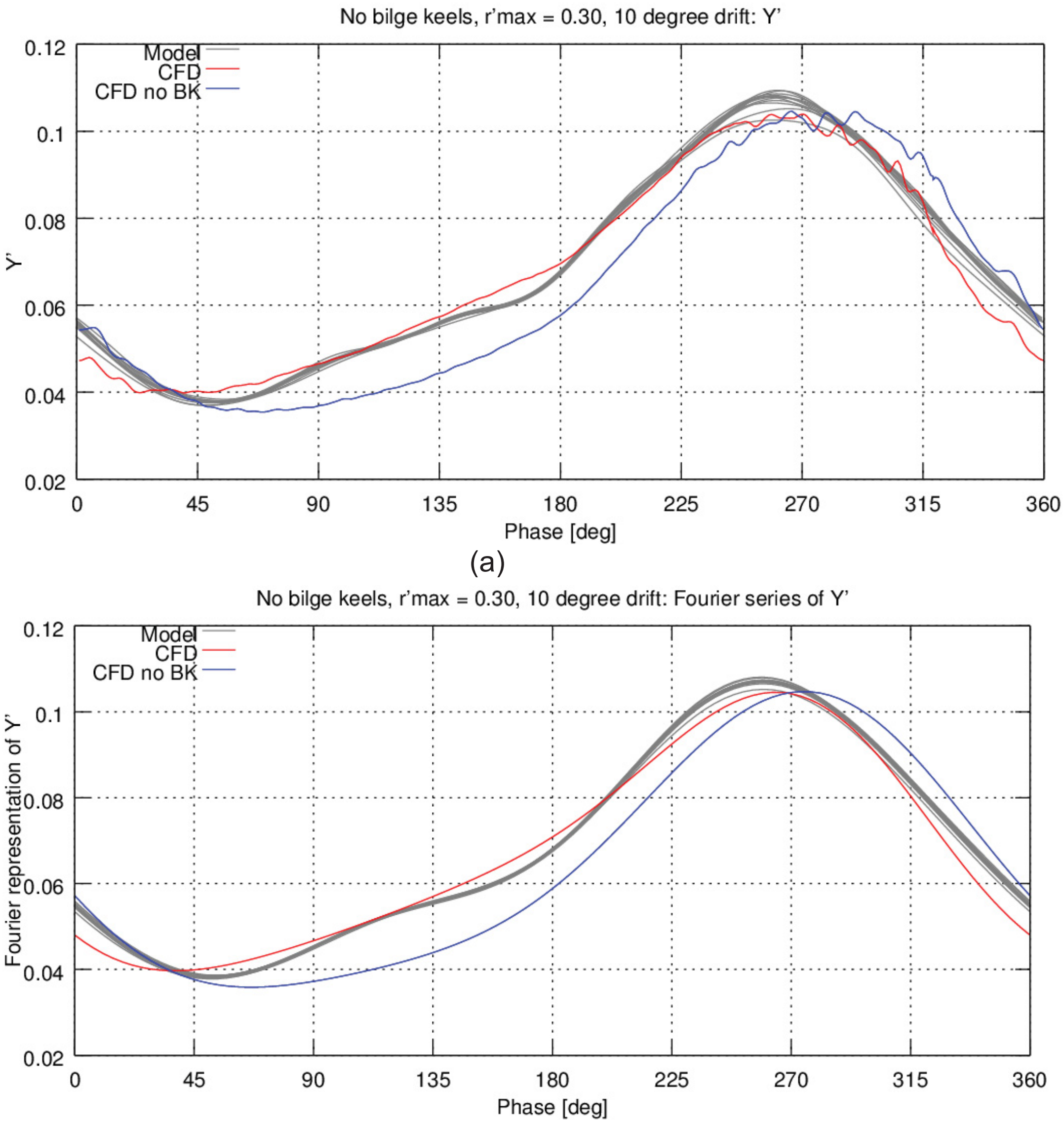

(a)

(b)

Figure B.5: Measured and Computed Y' in Bilge Keel Study for Yaw and Drift Test; (a) Pure Measured/Computed Data, (b) Fourier Representation of Data

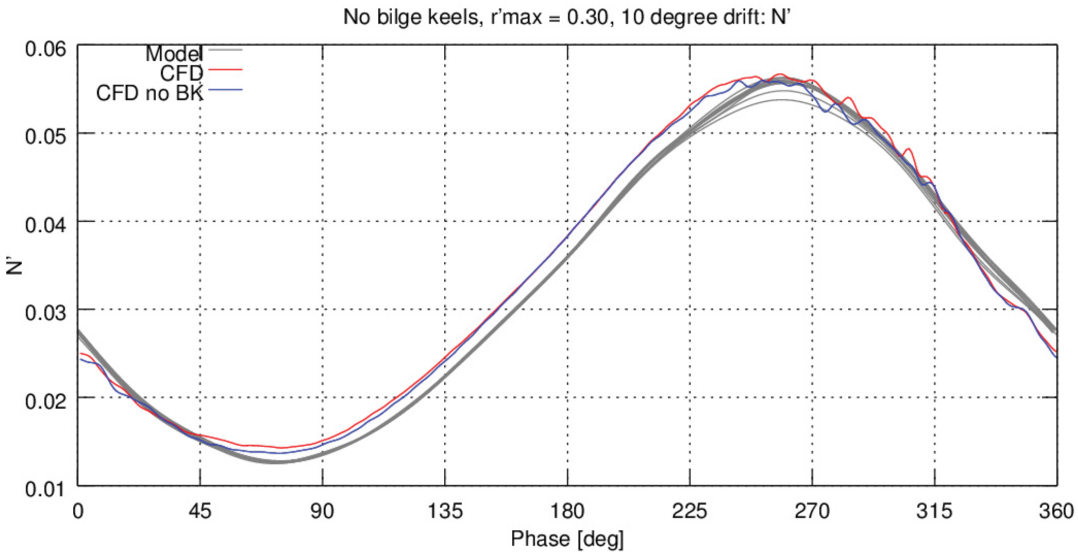

(a)

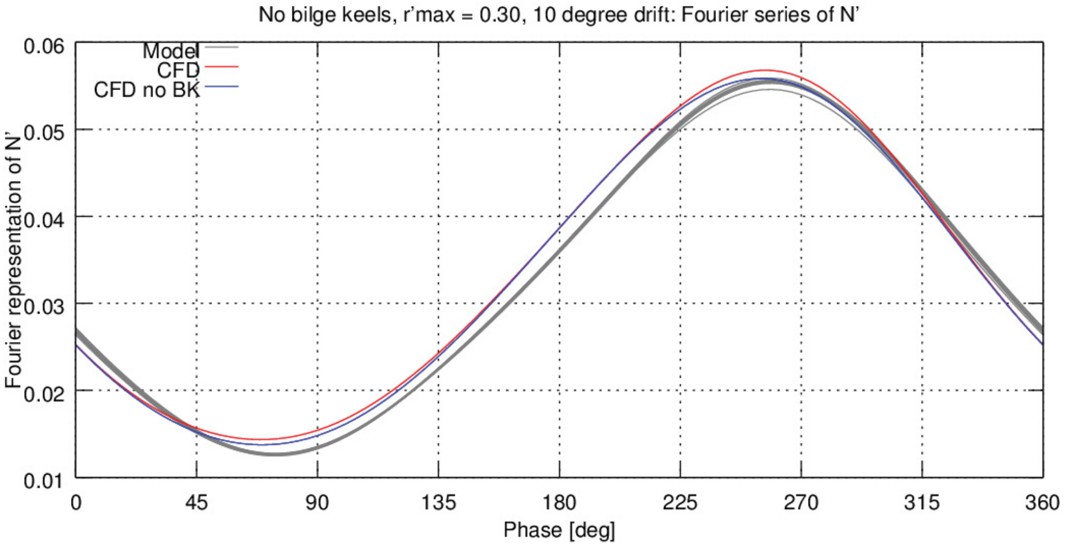

(b)

Figure B.6: Measured and Computed N' in Bilge Keel Study for Yaw and Drift Test; (a) Pure Measured/Computed Data, (b) Fourier Representation of Data

APPENDIX C. UNSTEADY PURE YAW

Effect of Bilge Keels

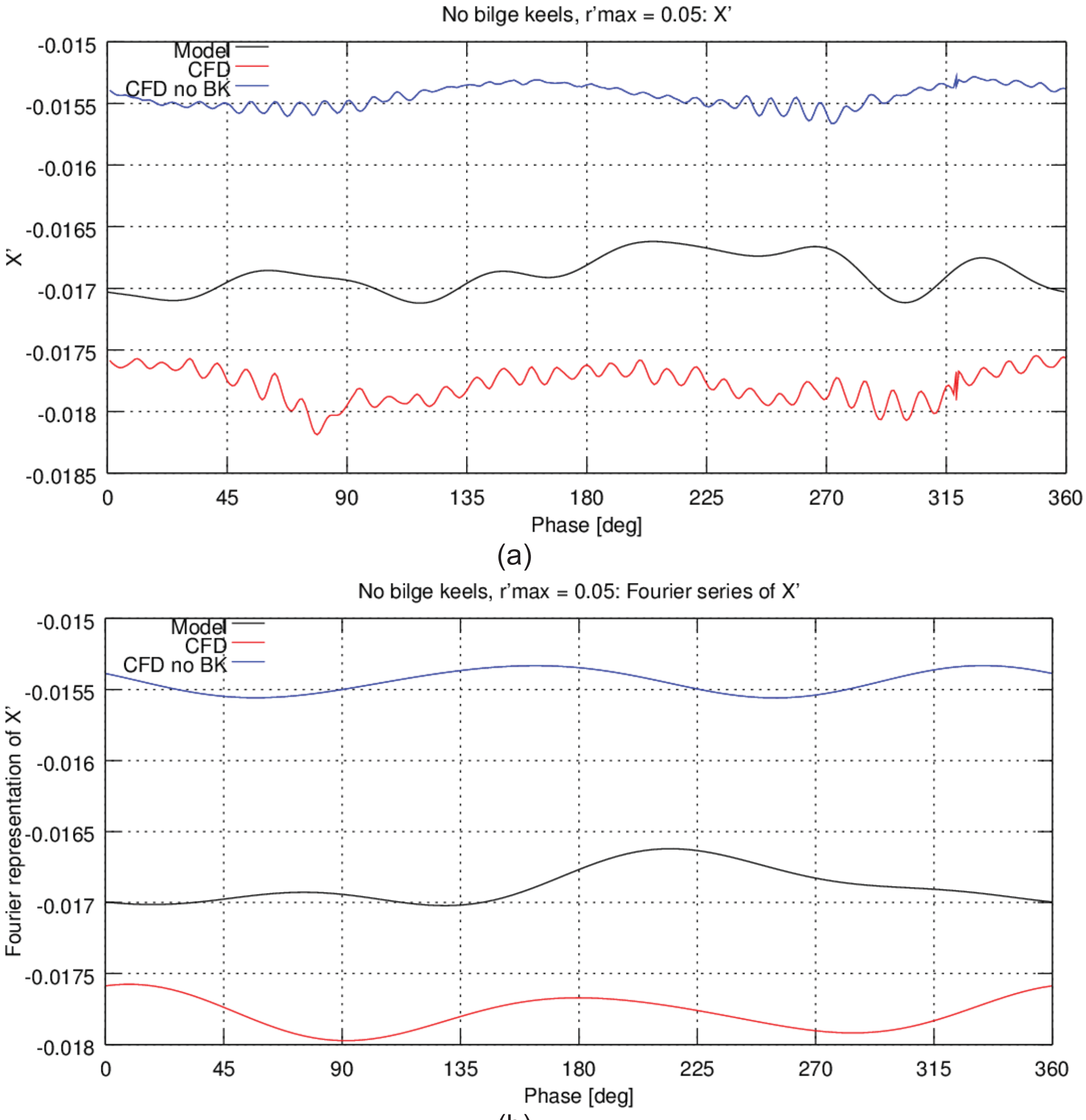

(a)

(b)

Figure C.1: Measured and Computed X' in Bilge Keel Study for Pure Yaw Test; (a) Pure Measured/Computed Data, (b) Fourier Representation of Data

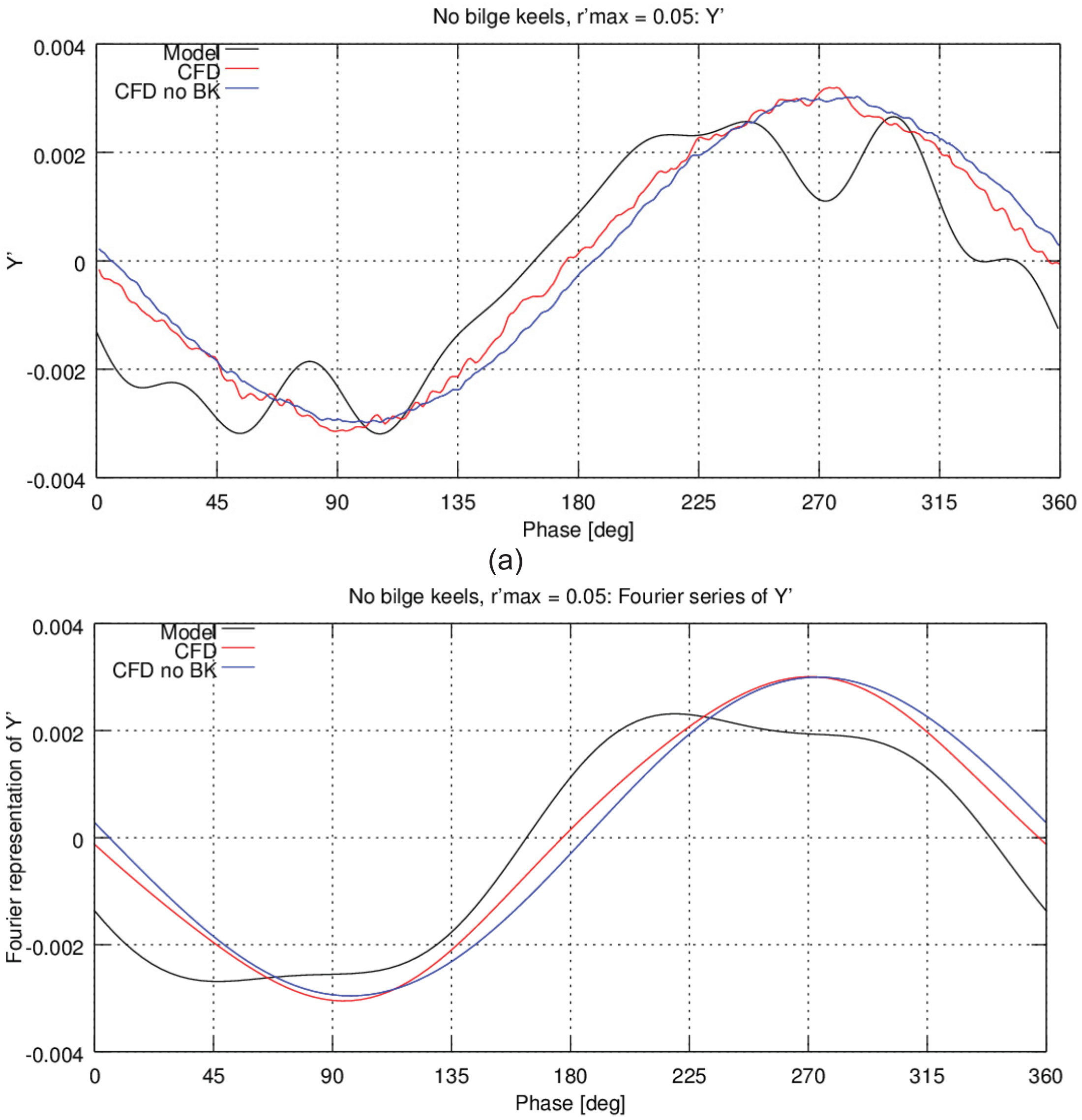

(b)

Figure C.2: Measured and Computed Y' in Bilge Keel Study for Pure Yaw Test; (a) Pure Measured/Computed Data, (b) Fourier Representation of Data

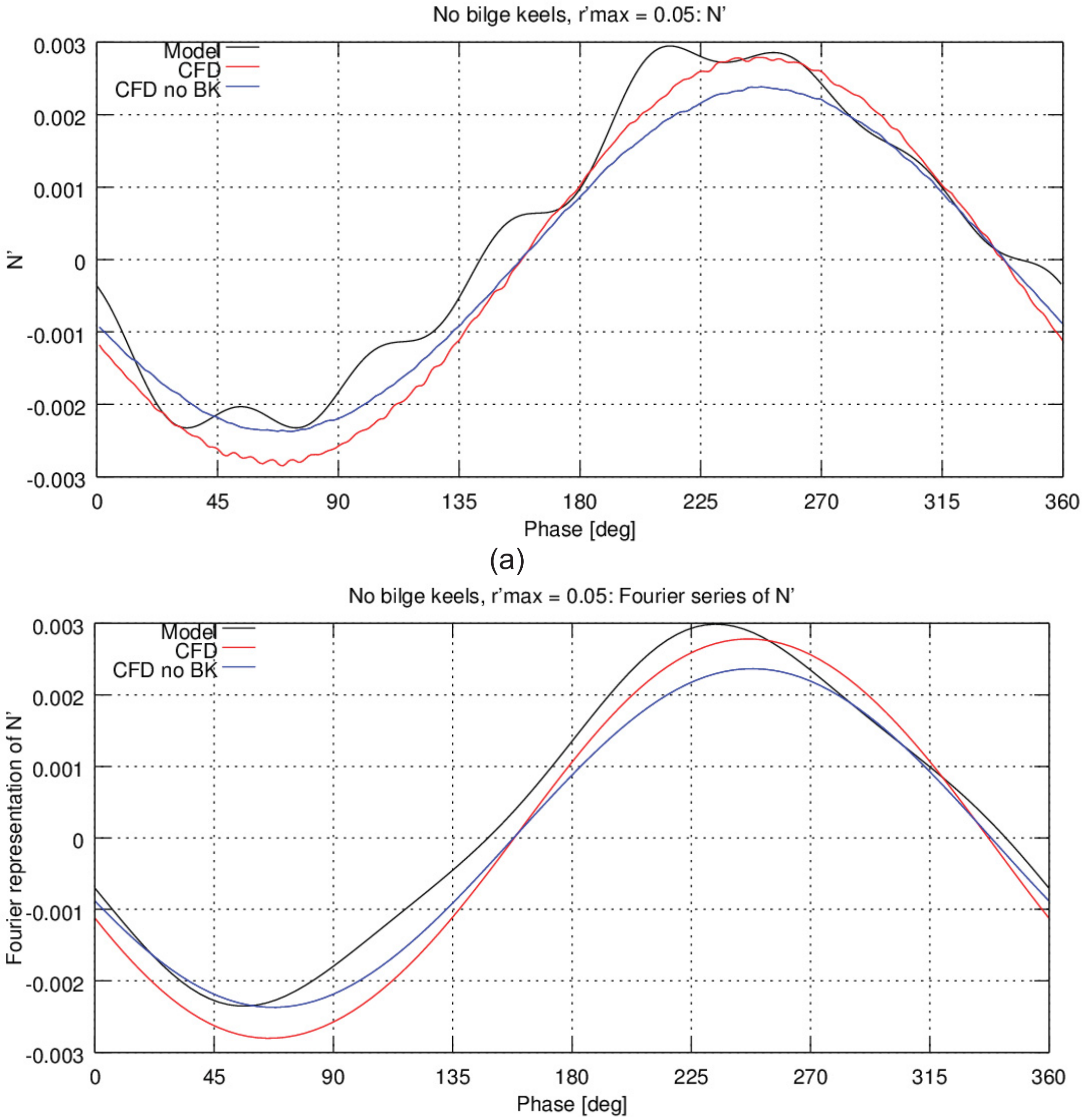

(a)

(b)

Figure C.3: Measured and Computed N' in Bilge Keel Study for Pure Yaw Test; (a) Pure Measured/Computed Data, (b) Fourier Representation of Data

APPENDIX D. UNSTEADY PURE SWAY

Effect of Bilge Keels

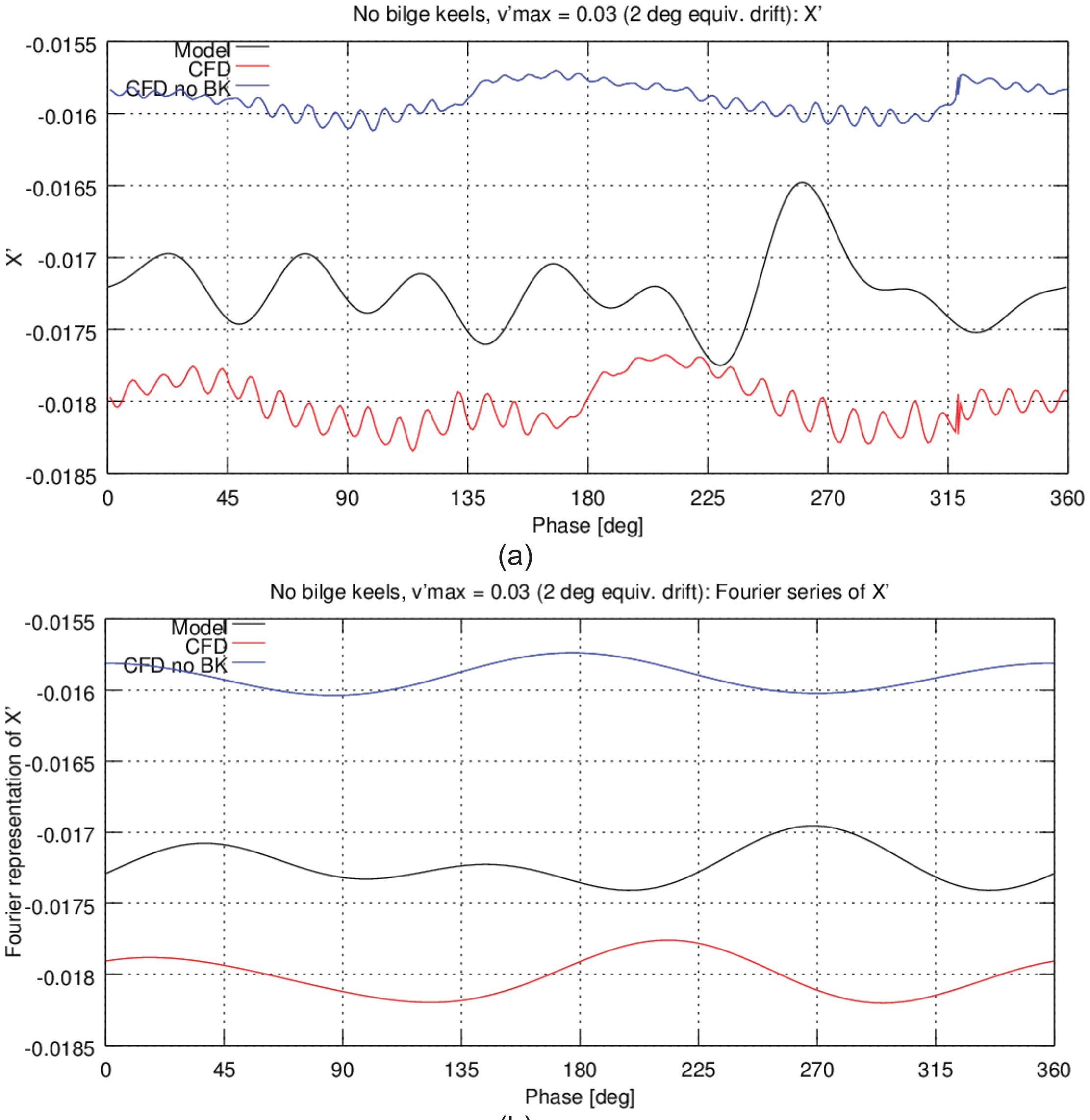

(a)

(b)

Figure D.1: Measured and Computed X' in Bilge Keel Study for Pure Sway Test; (a) Pure Measured/Computed Data, (b) Fourier Representation of Data

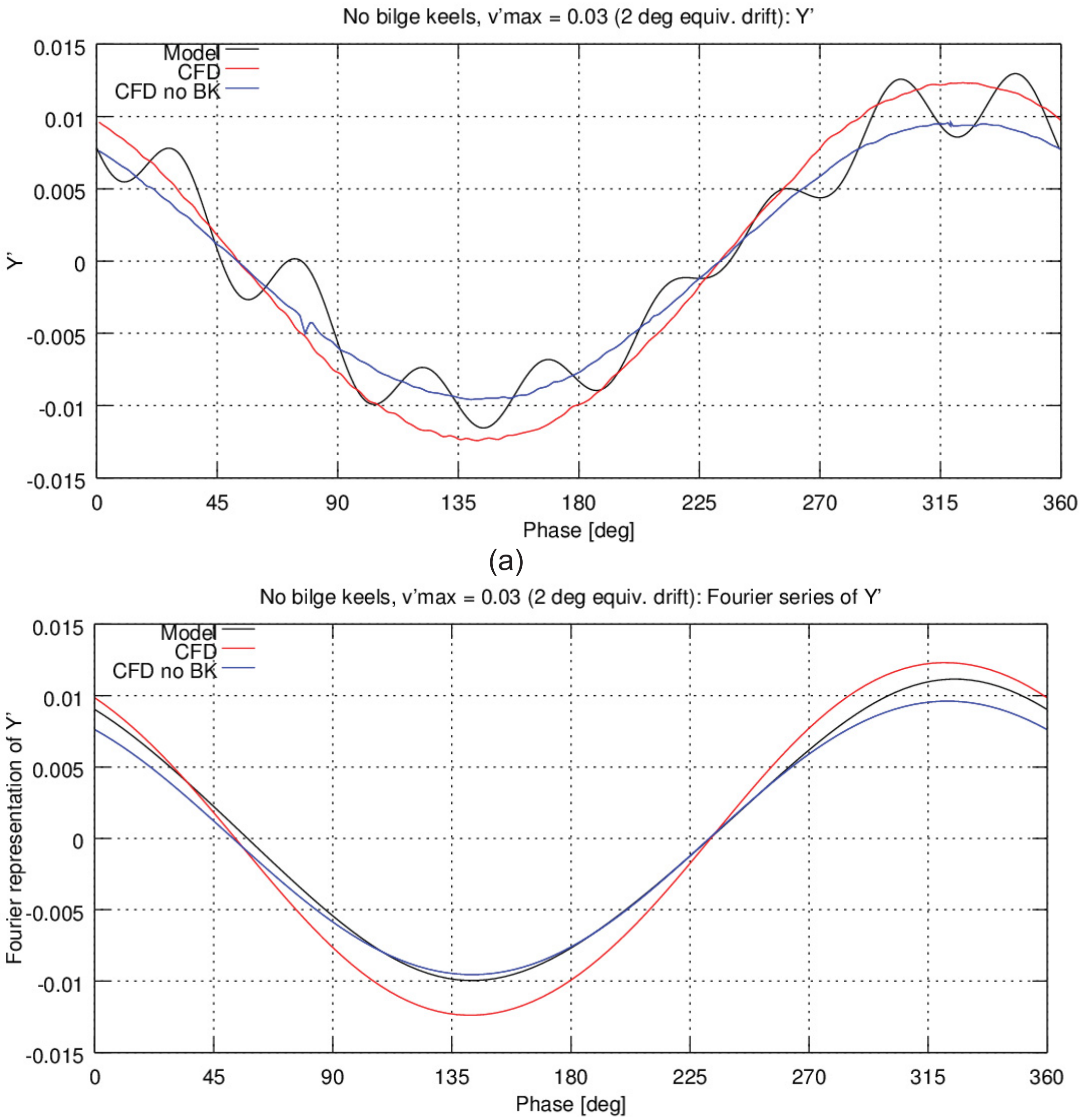

(a)

(b)

Figure D.2: Measured and Computed Y' in Bilge Keel Study for Pure Sway Test; (a) Pure Measured/Computed Data, (b) Fourier Representation of Data

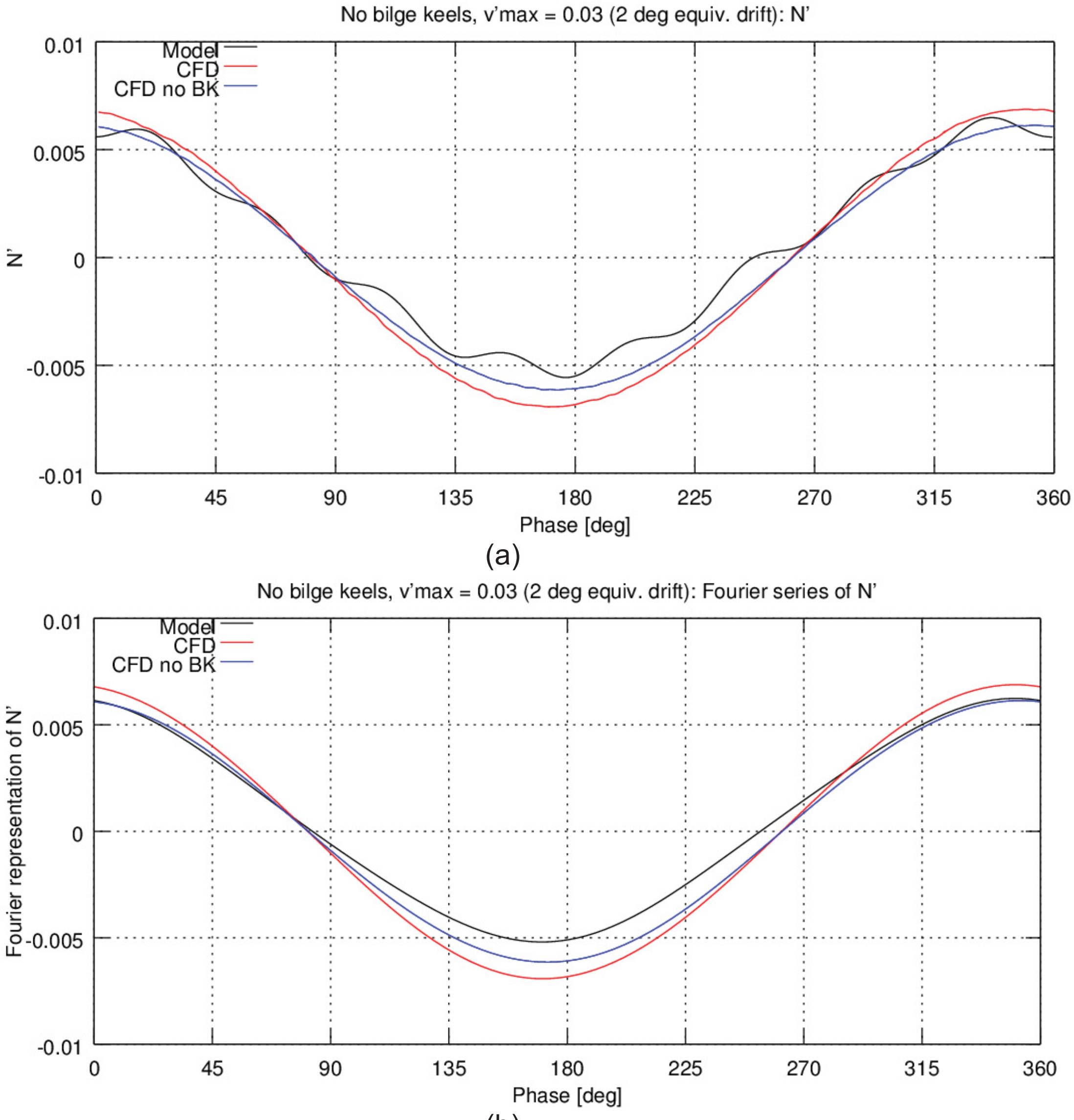

(a)

(b)

Figure D.3: Measured and Computed N' in Bilge Keel Study for Pure Sway Test; (a) Pure Measured/Computed Data, (b) Fourier Representation of Datad